POLITECNICO DI TORINO

Master of Science in Energy and Nuclear Engineering

Master thesis

Correlation of vorticity structures with heat transfer coefficient and friction factor in corrugated channel geometries

Supervisors

Prof. Laura Savoldi

Prof. Antonio Cammi

Prof. Luca Marocco

Candidate

Francesco Feudo

28th November 2025

Abstract

The present work investigates the thermo–fluid dynamic behavior of sinusoidal corrugated channels, with the objective of establishing quantitative links between vorticity structures, pressure losses, and heat transfer performance. Steady-state numerical simulations were performed with OpenFOAM (simpleFoam and scalarTransportFoam) for multiple corrugation amplitudes and wavelengths, covering a range of Reynolds numbers within the laminar and transitional regimes. The analysis of the vorticity field highlights the formation of recirculation zones and high-shear regions, whose intensity and occurrence rise with geometric corrugation and Reynolds number. These flow structures promote enhanced mixing and elevate the heat transfer coefficient, while simultaneously increasing frictional losses. Mean vorticity was adopted as indicator of the disturbance imposed by the geometry. The results reveal a consistent correlation between vorticity amplification and the growth of both Nusselt number and friction factor, emphasizing the central role of vortical dynamics in governing the performance of sinusoidal channels. Furthermore, the physical insights and empirical power-law correlations developed in this study have broader significance: the mechanisms identified here are directly translatable to more complex periodic architectures, such as triply periodic minimal surfaces (TPMS), thereby offering a foundation for the predictive design and optimization of next-generation compact heat exchangers.

Table of contents

1 Introduction

Vorticity is an inherent feature of fluid flow and plays a key role in heat and mass transfer phenomena. It can be artificially generated or naturally occurs in various flow configurations, such as near-wall regions of turbulent boundary layers or in flows over curved and rotating surfaces. A thorough understanding of vorticity is therefore fundamental for understanding heat transfer mechanisms and for developing both active and passive control strategies in numerous technological applications. According to Lee et al. [1], the corrugation geometry in plate heat exchangers strongly influences the formation of secondary vortices and, consequently, the overall heat transfer performance. Their analysis demonstrated that flow separation and reattachment near the contact points of adjacent corrugations produce localized vortical structures, which intensify fluid mixing and enhance heat transfer by thinning the thermal boundary layer. They also observed that sharper geometries, such as triangular corrugations, generate stronger vortices and higher heat transfer rates, although at the expense of increased pressure losses, thus emphasizing the intrinsic coupling between vorticity generation, thermal enhancement, and frictional resistance in corrugated channels. Similarly, XiaoMing Gao et al. [2] showed that even a single corrugated wall, compared to a smooth channel, significantly alters the flow field by inducing separation and recirculation zones. These structures promote local vortices that enhance heat transfer but simultaneously increase hydraulic losses.

Although these studies have established the qualitative link between vorticity generation, heat transfer enhancement, and pressure drop, a quantitative understanding of how specific vortex structures correlate with the local and global heat transfer coefficient and friction factor remains limited. In particular, the literature lacks a systematic investigation of the relationship between the characteristics of vortical flow (strength, size, and spatial distribution) and the thermal hydraulic performance across different corrugated geometries.

Therefore, this thesis aims to establish a correlation between vorticity structures, heat transfer coefficient, and friction factor in corrugated channel configurations, providing new insights into the fundamental mechanisms that govern thermal enhancement and flow resistance in such systems.

1.1 Influence of wall corrugation on vorticity, pressure losses and heat transfer

The presence of wall corrugations in a channel enforces a fundamental modification of the flow field: the alternating expansions and contractions, contact points and valleys induce flow separation and reattachment, form recirculation zones and vortical structures.

Increasing wall roughness adding ribs [3], tapes, TPMS (Triple Periodic Minimal Surfaces) [4] or just curving the wall may help the development of secondary flow as it’s possible to see in Figure 1.1 [3].

In channels with corrugated or wavy walls it has been shown that recirculation zones appear downstream of the crests or “contact points”, and within these zones pairs of counter-rotating vortices may develop, which increase mixing between core and wall fluid [5]. Such vortical motion promotes disruption of the thermal boundary layer and enhances convective heat

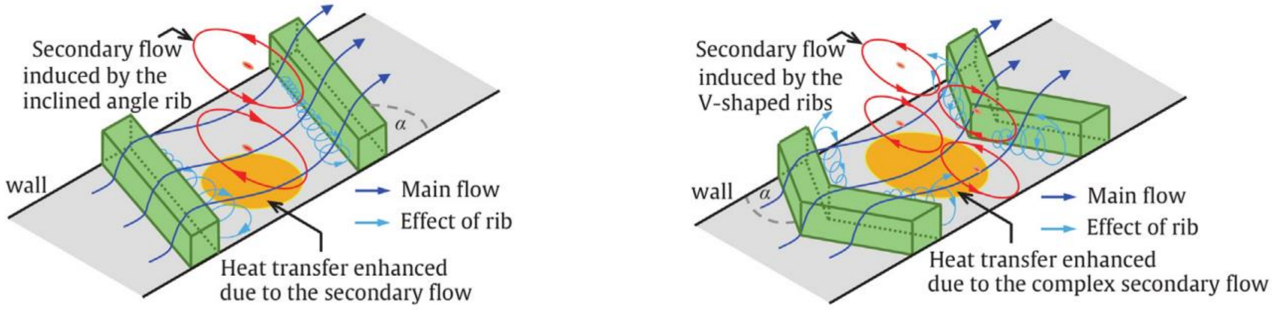

(a) Inclined angle ribs. (b) V-shaped ribs.

Figure 1.1: conceptual 3-D flow pattern inside rib-roughened walls

transfer, but simultaneously raises the shear and form drag associated with the non-smooth geometry, thereby increasing pressure losses.

Indeed, experimental and numerical studies show that corrugated channel configurations yield significantly higher Nusselt numbers compared with smooth channels, thanks to the enhanced mixing and higher vorticity, yet at the expense of markedly higher pressure drop [6]. Moreover, parametric studies indicate that the strength of the recirculation zones and vortex generation scale with geometrical features (such as corrugation amplitude and wavelength) and flow Reynolds number: increasing the corrugation amplitude or steepness elevates vortex intensity and hence transfer enhancement, but also amplifies hydraulic penalty [7]. Thus, wall corrugation acts as a two-edged mechanism: on one hand it favors vorticity generation and improves heat transfer; on the other hand, it increases pressure losses and reduces hydraulic efficiency. For this reason, when designing corrugated geometries for heat exchangers or enhanced convective systems, it is mandatory to seek an optimal trade-off between thermal gain and frictional cost.

1.2 TPMS and sinusoidal channels

Triply Periodic Minimal Surfaces (TPMS) are complex geometric structures with surfaces that repeat smoothly across three dimensions [8]. These surfaces are defined by a single implicit function and have transitions between their repeating units, making them suitable for stress, fluid flow, and heat transfer applications. Some common TPMS forms include gyroids, Schwarz surfaces, and diamond and linoid patterns, each offering unique thermal properties, as shown in Figure 1.2 [8].

For instance, gyroids are known for their high surface-to-volume ratio and open lattice structure, which encourages fluid mixing, a key factor for effective heat transfer. With low thermal resistance comparable to traditional heat-dissipating structures, TPMS elements have emerged as a promising design strategy for maximizing heat transfer while maintaining compact, highly efficient thermal solutions due to the following characteristics:

- Low Thermal Resistance: TPMS surfaces facilitate heat dissipation.
- Enhanced Fluid Mixing: The geometry lessens fluid boundary layers.
- High Surface-to-Volume Ratio: With an extensive contact area for fluid interaction, TPMS geometries make optimal use of available space for thermal exchange.

However, TPMS designs are not excluded by challenges. Their dense structure can lead to increased pressure drop, and their complex shapes typically require additive manufacturing, which limits material options and can increase production costs.

The link between TPMS and vorticity lies in their complex flow paths. The curvature and interconnection of TPMS channels promote the formation of secondary flows, recirculation zones, and localized acceleration and deceleration of the fluid, all of which contribute to vorticity generation. These vortical structures disrupt the thermal boundary layer and enhance convective heat transfer through improved fluid mixing. However, the same mechanisms that promote vorticity also increase frictional losses, resulting in higher pressure drops. As several studies have shown [9], this trade-off between thermal enhancement and hydraulic performance is intrinsic to the design of TPMS flow channels.

A useful way to study and understand the fluid dynamic and thermal behavior of TPMS structures is through sinusoidal or corrugated channels, which represent simplified, two-dimensional periodic systems. These geometries reproduce the essential features of periodicity, curvature, and flow separation that are also present in TPMS, but in a more computationally tractable form. Lee et al. [10] showed that the periodicity of the wall shape governs the onset and strength of recirculating regions, directly linking vortex generation to both Nusselt number enhancement and friction factor increase.

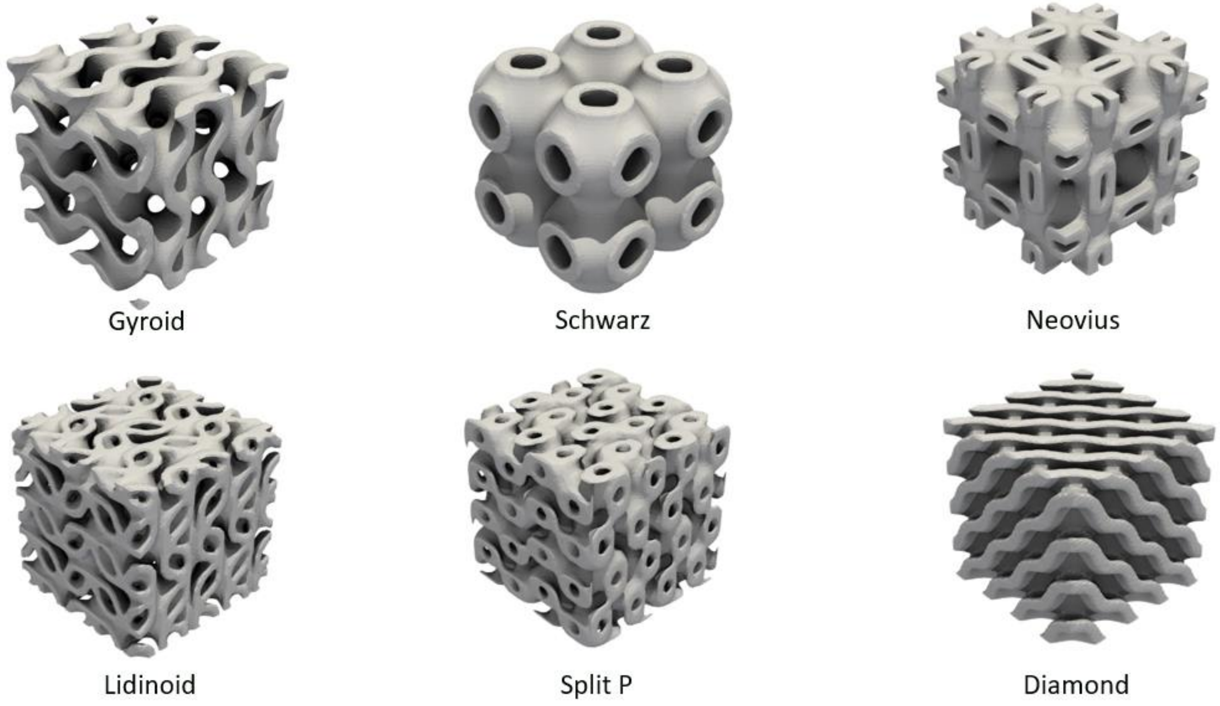

Gyroid
Schwarz
Neovius
Lidinoid
Split P
Diamond

Figure 1.2: Example of TPMS with different geometries

1.3 Aim of the work

Since TPMS geometries can be regarded as a three-dimensional extension of sinusoidal periodicity, numerical simulations on sinusoidal channels offer a valuable means of investigating the fundamental mechanisms of vorticity generation, boundary-layer disruption, and the associated thermal–hydraulic trade-offs. Once these relationships are well understood in simpler two-dimensional periodic channels, they can be translated to TPMS structures, where the same physical principles govern fluid mixing, pressure losses, and heat transfer enhancement within a fully three-dimensional periodic framework.

The main objective of this work is to establish quantitative correlations between the friction factor, vorticity, and Nusselt number, using as a reference dataset the numerical results obtained from a wide range of two-dimensional sinusoidal channel configurations. By systematically varying the geometric parameters and Reynolds number, the study aims to identify how vortex intensity and distribution influence both the heat transfer coefficient and the hydraulic performance. This approach provides a foundational understanding that can later be extended to more complex periodic geometries such as TPMS.

The study is organized into three main sections:

- First, the case setup is presented in detail, including the rationale behind the geometric configuration, the mesh generation strategy, the selected boundary conditions and thermophysical properties, as well as the numerical models implemented within the chosen OpenFOAM solvers. Particular attention is dedicated to the use of symmetry shifts and periodic boundary conditions, which were introduced to simplify the computational domain and streamline the post-processing phase.
- The second part focuses on the qualitative analysis of the flow, providing visualizations of velocity, vorticity, and temperature fields to illustrate the main features induced by the corrugated geometry.
- Finally, the quantitative results are examined with the aim of establishing empirical correlations linking vorticity to both friction factor and Nusselt number, thus offering a predictive framework for assessing the thermo-hydraulic performance of sinusoidal channels.

2 Case study

2.1 Sinusoidal geometries

Considering flow of an incompressible Newtonian fluid forced through a wavy sinusoidal channel, as in Figure 2.1 [11]:

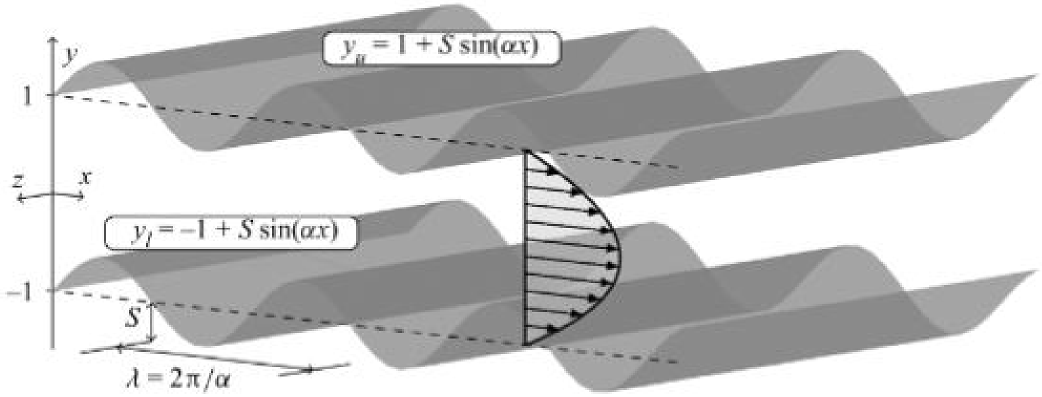

Figure 2.1: Sinusoidal channel geometry

The geometry of a sinusoidal channel can be characterized by three key parameters: the corrugation amplitude S, the wavelength λ, and the corrugation number α.

Parameter S represents the peak-to-trough height of the wall undulations, controlling the intensity of the wall modulation; λ is the distance over which the sinusoidal pattern repeats itself, defining the spatial period of the channel; α is a dimensionless quantity indicating the number of waves per unit length along the channel. These quantities are related through the simple geometric relation:

$$\lambda = \frac{2\pi}{\alpha} \tag{2.1}$$

Understanding these parameters is essential for analyzing the flow and thermal behavior within sinusoidal channels, as they directly influence the generation of vorticity, the development of the thermal boundary layer, and the overall hydraulic resistance.

In OpenFOAM, the sinusoidal channel geometries were generated using the *blockMesh* utility, which allows for a fully parametric definition of the computational domain. The wall profiles are expressed analytically as

$$\begin{aligned} y_u &= 1 + Scos(\alpha x) \\ y_l &= 1 - Scos(\alpha x) \end{aligned} \tag{2.2}$$

where y_u and y_l denote the upper and lower walls, respectively.

By specifying the parameters α and S as input variables in the mesh generation script, both the geometry and the mesh resolution can be systematically varied.

The specific values of the corrugation amplitude and corrugation wavenumber used in this study were selected based on previous investigations reported in the literature on sinusoidal channels [11] . These values provide a well-established reference framework and ensure that the selected geometries are representative of conditions that significantly influence flow structures, vorticity generation, and heat transfer. By following this reference, the study maintains consistency with earlier works while allowing for systematic exploration of the impact of geometric variations on thermo-fluid dynamic performance.

Chosen configurations are depicted in Figure 2.2:

To compare different configurations, hydraulic diameter has been defined as:

$$D_h = \frac{4A_{lat}}{2p} \tag{2.3}$$

Figure 2.3 illustrates that an increase in wall corrugation leads to a larger wetted perimeter, which consequently reduces the hydraulic diameter of the channel.

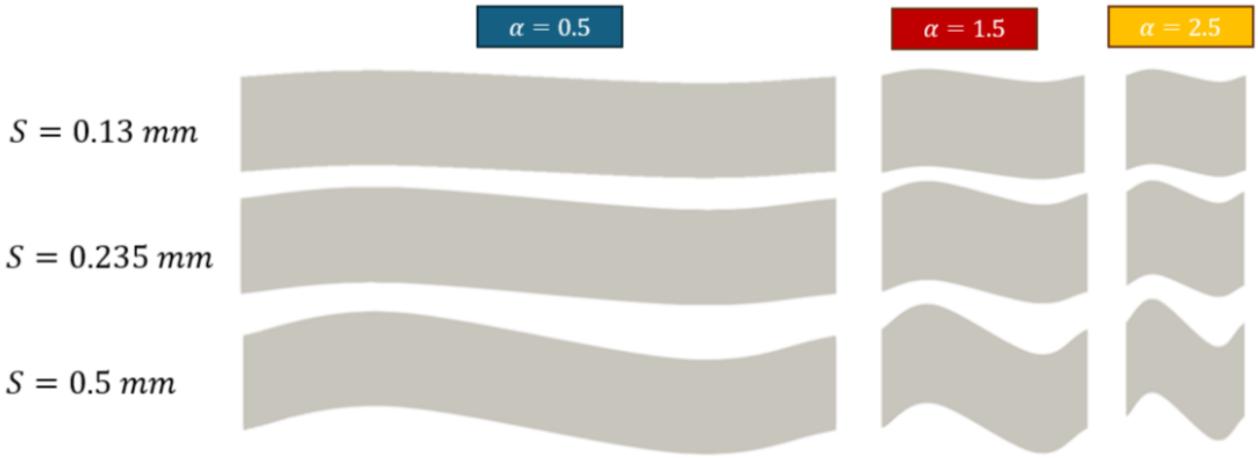

Figure 2.2: Chosen geometries

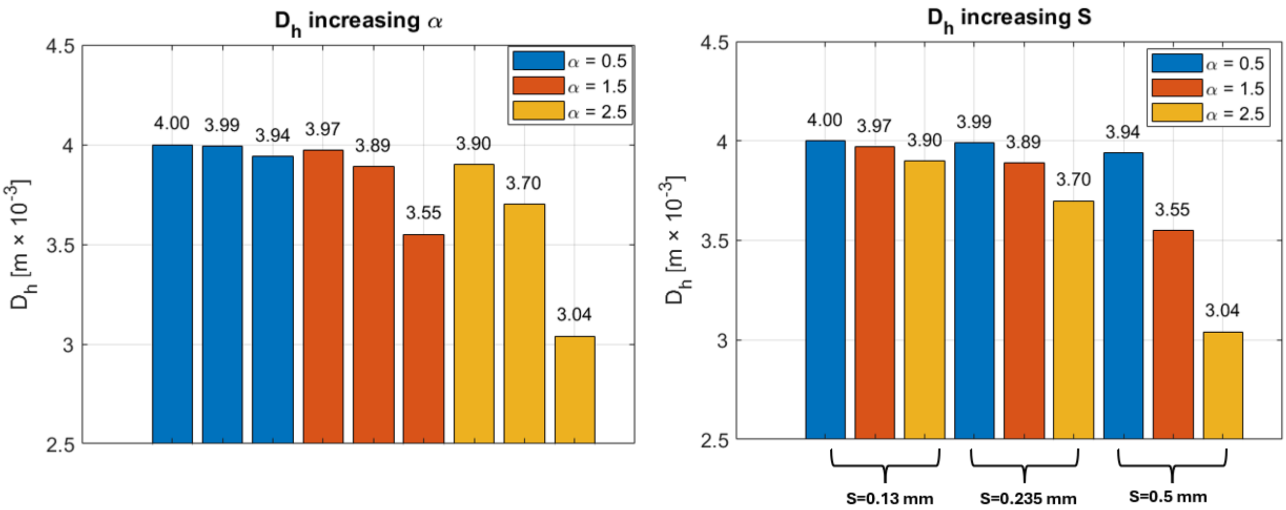

Figure 3.3: hydraulic diameter for all the configurations

2.2 Mesh generation

The definition and parametrization of the computational mesh represent a fundamental step in achieving reliable numerical simulations. The quality of the domain discretization directly affects both the accuracy of the results and the stability of the numerical solution. However, a highly refined mesh inevitably increases the number of cells and the overall computational cost.

For this reason, it is essential to identify an optimal compromise between accuracy and computational efficiency, adapting the mesh resolution to the specific characteristics of the flow or physical field under investigation. Mesh parametrization enables the automation and control of this process, allowing rapid adjustments of the resolution or element distribution according to different geometric configurations or boundary conditions.

2.2.1 BlockMesh utility

Meshes were generated using the blockMesh utility, which allows for the creation of fully parametric hexahedral grids with graded cells and curved edges. The domain was constructed by defining multiple blocks, each delimited by eight vertices corresponding to the corners of a hexahedron.

Geometry was designed to reproduce a sinusoidal channel with periodic boundary conditions in the streamwise direction. The upper and lower channel walls were described using spline edges, which interpolate a set of control points defined by the wavelength λ and the corrugation amplitude S. This approach enables the generation of smooth sinusoidal profiles without the need for additional meshing tools such as *snappyHexMeshDict*.

To accurately solve the near-wall region, two additional boundary layers were introduced: one adjacent to the upper wall and one to the lower wall. These were implemented by defining two extra sets of vertices, each parameterized through the variables y_u and y_l. By modifying these parameters directly within the *blockMeshDict*, it is possible to adjust the wall-normal thickness of the boundary layers without altering the rest of the geometry (Figure 2.4):

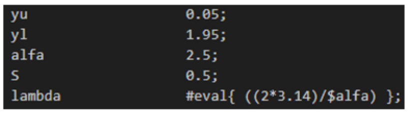

```
yu                    0.05;
yl                    1.95;
alfa                  2.5;
S                     0.5;
lambda                #eval{ ((2*3.14)/$alfa) };
```

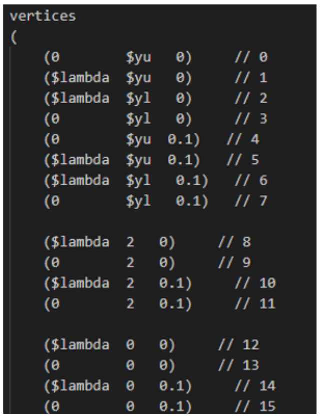

```
vertices
(
    (0          $yu    0)      // 0
    ($lambda    $yu    0)      // 1
    ($lambda    $yl    0)      // 2
    (0          $yl    0)      // 3
    (0          $yu   0.1)    // 4
    ($lambda    $yu   0.1)    // 5
    ($lambda    $yl    0.1)    // 6
    (0          $yl    0.1)    // 7

    ($lambda   2   0)      // 8
    (0         2   0)      // 9
    ($lambda   2   0.1)      // 10
    (0         2   0.1)      // 11

    ($lambda   0   0)      // 12
    (0         0   0)      // 13
    ($lambda   0   0.1)      // 14
    (0         0   0.1)      // 15
```

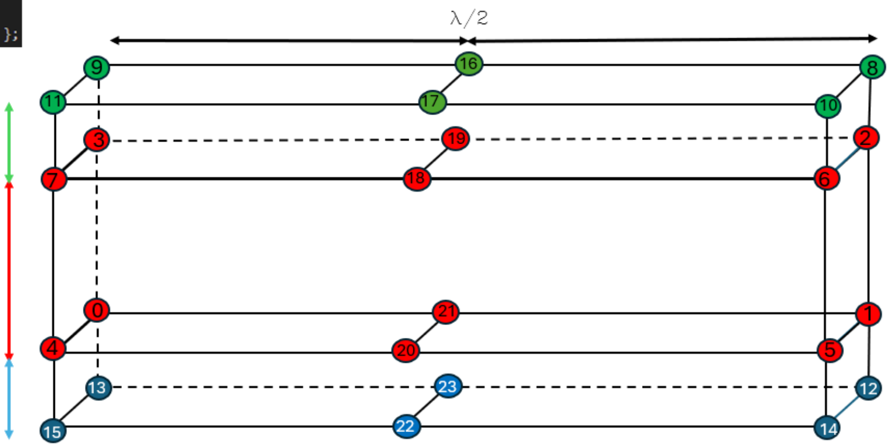

Figure 2.4: blockMesh tool

The mesh is composed of three main hexahedral blocks. The central block defines the main flow domain, while the upper and lower blocks represent the boundary layer regions, each refined independently to have a high refinement near wall

Finally, the cyclicAMI boundary condition was imposed at the inlet and outlet, with the separation vector corresponding to one wavelength (λ), ensuring periodicity along the streamwise direction. The front and back faces were set as empty, enforcing two-dimensional flow conditions.

2.2.2 Grid convergence study

To ensure that the numerical solution was independent of the computational grid, a grid convergence study was performed following the Richardson extrapolation method [12].

Richardson extrapolation method is a systematic approach used to estimate the exact solution of a numerical problem by analyzing the results obtained with different grid resolutions. The method assumes that the discretization error decreases as a power of the characteristic grid size h, defined as

$$h = \sqrt{\frac{1}{\#\ of\ cells}} \tag{2.4}$$

According to

$$\phi(h) = \phi_{exact} + Ch^{p} \tag{2.5}$$

where $\phi(h)$ is the numerical result obtained with grid size h, ϕ_{exact} is the asymptotic (or exact) value toward which the solution converges, C is a constant related to the magnitude of the numerical error, and p is the numerical order of accuracy of the discretization scheme.

By performing the same simulation on at least three grids of increasing refinement, the apparent order p can be estimated as

(2.6)

$$p = \frac{ln\left[\frac{\phi_1 - \phi_2}{\phi_2 - \phi_3}\right]}{\ln(r_{32})}$$

Where ϕ_1, ϕ_2, ϕ_3 are the computed results on the coarse, medium, and fine grids, respectively, and $r_{32} = \frac{h_2}{h_3}$ is the refinement ratio between the medium and fine grids. Once p is known, the extrapolated value corresponding to an infinitely fine grid can be calculated using

$$\phi_{ext} = \phi_3 + \frac{(\phi_3 - \phi_2)}{(r_{32}^p - 1)} \tag{2.7}$$

This extrapolated value ϕ_{ext} provides an estimate of the solution that would be obtained if the grid spacing approached zero, thus minimizing the effect of discretization errors. The method also allows for the evaluation of the *Grid Convergence Index* (GCI), which quantifies the relative uncertainty due to grid dependence.

Simulations were performed at Reynolds equal 500, providing pressure drop Δp [Pa] (to quantify the relative error bar when evaluating hydraulic quantities) and average temperature [K] at the wall (to quantify the relative error bar when evaluating thermal quantities) for each grid.

The order of accuracy of the numerical scheme was estimated from the results using the logarithmic relation between successive grid refinements (eq. 2.6). This allowed the calculation of the apparent order p and, subsequently, the extrapolated value corresponding to an infinitely fine grid, obtained through Richardson extrapolation (eq. 2.7). The apparent percentage errors between consecutive grids (coarse–medium and medium–fine) were evaluated, as well as the *Grid Convergence Index* (GCI) for both pairs, using a safety factor of 1.25 to account for uncertainties in the estimation of p.

Finally, the relative errors of each simulation with respect to the extrapolated value were computed and plotted against the grid size h. The results showed a monotonic convergence toward the asymptotic value, confirming that the mesh resolution adopted for the finest grid is within the grid-independent regime.

In the following section, the grid convergence study is presented for the most corrugated geometry; however, the same procedure was also performed for the other configurations. The corresponding error bars obtained from these analyses were then applied to the results to provide a quantification of the numerical uncertainties.

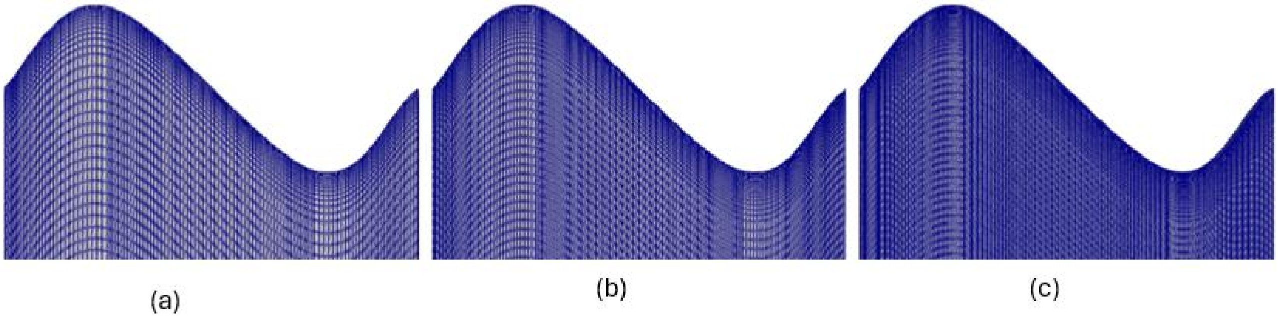

Figure 2.5: grid for α=2.5, S=0.5 mm: (a) coarse (b) medium (c) fine

In Figure 2.5, grids of different sizes are depicted for the most corrugated geometry.

In Table I, values for grid size h and refinement ratio are defined:

Table I: grid parameters

	h	r_{ij}
Coarse	0.013	/
Medium	0.009	1.34
Fine	0.007	1.33

Figure 2.6 shows the values for pressure drop with respect to the extrapolated value and their relative error, evaluated as $\epsilon_{ij} = \frac{|dp_i - dp_j|}{|dp_i|} * 100$:

The grid convergence study confirms that the numerical solution approaches a stable value as the grid is refined. The pressure drop (Figure 2.6a) decreases progressively with smaller grid size, converging toward the Richardson extrapolated value. The relative error (Figure 2.6b) follows a consistent trend, reducing to less than a few percent for the finest grid.

Using the medium grid adopted in this work, this corresponds to an uncertainty of approximately 0.33% which is represented as an error bar in the results of the most corrugated geometry for both the pressure drop and the corresponding friction factor.

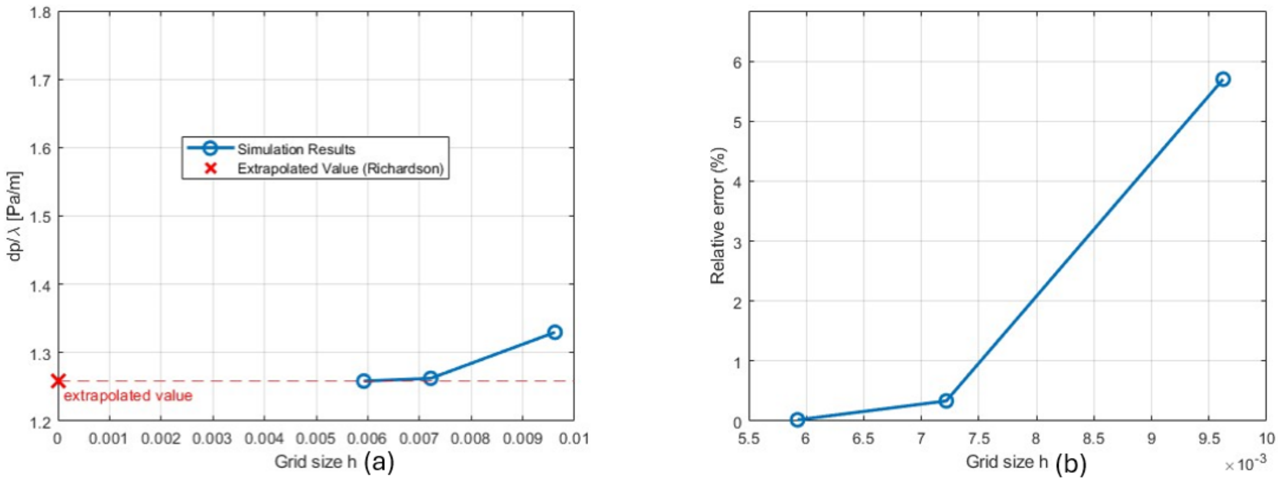

Figure 2.6: grid convergence study: (a) pressure drop for each grid, (b) relative error

The analysis of the thermal results focuses on the average reached temperature of the upper wall. An accurate prediction of this quantity is essential, as it directly affects the reliability of the heat transfer results. Ensuring a well-resolved wall temperature distribution therefore provides confidence in the correctness and consistency of the thermal performance obtained from the simulations.

In Figure 2.7, grid convergence study (a) and relative error (b) with respect to the extrapolated value are shown:

Similarly to what has been said for pressure drop, can also be applied to the average wall temperature: using medium grid it’s possible to achieve 1.6% error bar for the thermal results.

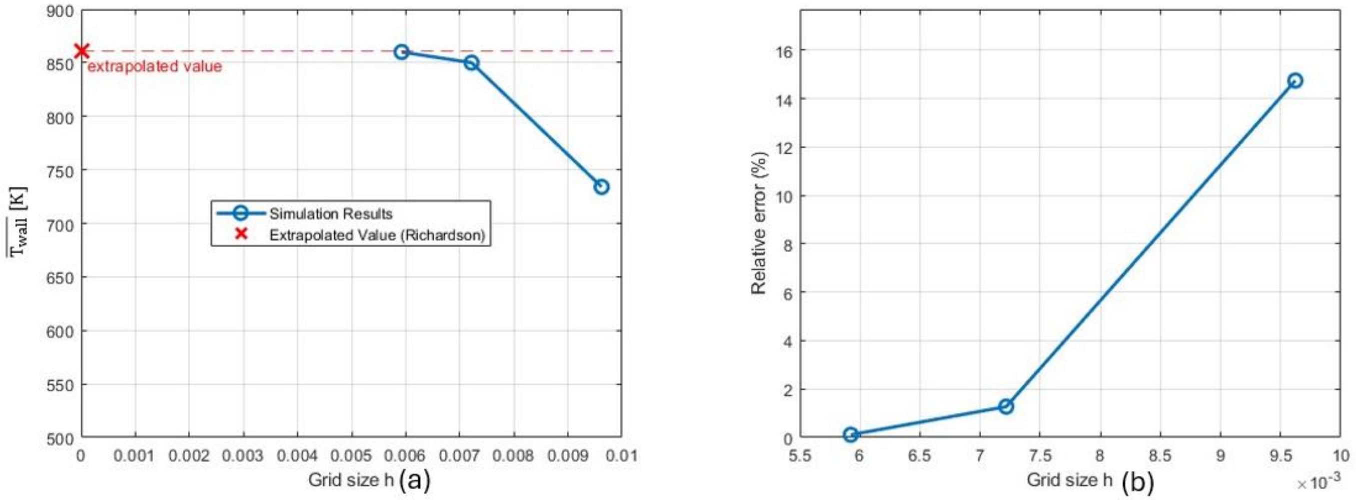

Figure 2.7: grid convergence study: (a) wall temperature for each grid, (b) relative error

2.3 Boundary conditions

The numerical simulations were carried out using OpenFOAM and subsequently validated and compared with results obtained from STAR-CCM+ to ensure consistency and reliability. The computational domain is a 2D sinusoidal channel, where periodic boundary conditions were imposed both for the fluid flow and thermal fields to reproduce a fully developed regime. The working fluid is water, with a constant Prandtl number equal to 7 and constant thermophysical properties:

$$Pr = \frac{\nu}{D_t} = \frac{\mu c_p}{k} \tag{2.8}$$

D_t represents the thermal diffusivity of the fluid, while ν represents the kinematic diffusivity.

The mean velocity in the channel is fixed at $2.5 \times 10^{-3}\,\frac{m}{s}$, while the flow regime was simulated at both laminar conditions (Re=10, 100, 300, 500) and turbulent conditions (Re=5000, 10000, 20000). The variation of the Reynolds number is achieved by changing the dynamic viscosity (μ) of the fluid while maintaining a constant mean velocity (U_m) and Prandtl number; consequently, the thermal conductivity (k) was also adjusted to preserve the relationship among the thermophysical properties.

The thermal boundary conditions applied to the sinusoidal channel consist of constant isothermal temperature of 500 K and a uniform heat flux of 2.5×10^4 W/m^2. These boundary conditions are imposed on both sinusoidal surfaces of the channel to reproduce a constant thermal load and to study the resulting heat transfer characteristics under steady-state conditions. This configuration enables analysis of how the flow and temperature fields interact with the wavy geometry while maintaining a controlled and reproducible thermal environment. Figure 2.8 shows the imposed thermal boundary conditions.

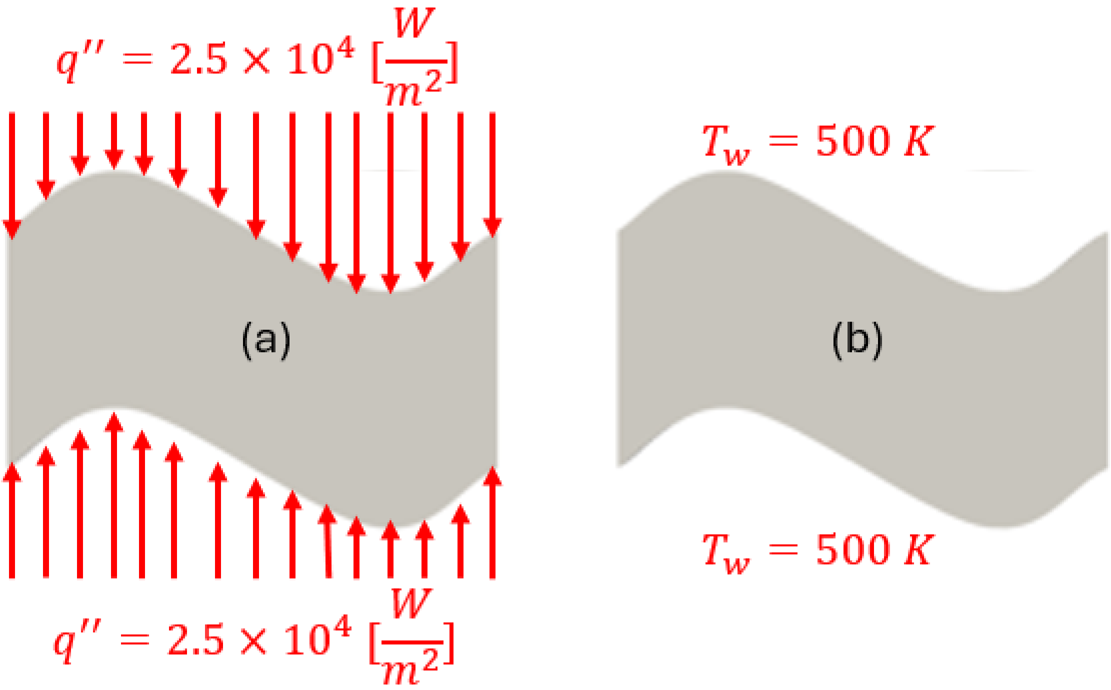

Figure 2.8: Thermal boundary conditions: (a) imposed q" (b) imposed T

2.4 OpenFOAM solver

OpenFOAM can solve any different cases: in this work SIMPLE algorithm is used to solve hydraulic part of the problem, then flow is “freezed” and thermal part is solved using SCALARTRANSPORT algorithm.

2.4.1 SIMPLE algorithm

Semi Implicit Method for Pressure Linked Equations (SIMPLE) couples u, p momentum and mass conservation equations:

$$\nabla \cdot u = 0 \tag{2.9}$$

$$\nabla \cdot (uu) - \nabla \cdot R = -\nabla p + S_u \tag{2.10}$$

Where u is the velocity, p is the kinematic pressure, R is the stress tensor and S_u is the momentum source.

In the SIMPLE procedure, these equations are discretized using the finite volume method. First, the momentum equation is solved using a guessed pressure field to obtain an intermediate velocity u*. Then, a pressure correction equation is derived from the continuity constraint to enforce mass conservation. The corrected fields are updated as:

$$p = p^* + \alpha_p p' \tag{2.11}$$

$$\mathrm{u} = \mathrm{u}^* - \frac{1}{A_u}\nabla p' \tag{2.12}$$

where $p'$is the pressure correction, $A_u$is the diagonal coefficient of the discretized momentum equation, and $\alpha_p$is an under-relaxation factor used to ensure numerical stability.

The algorithm iterates between solving the momentum and pressure correction equations until both the velocity and pressure fields satisfy the continuity equation. This method provides a robust approach for steady-state incompressible flow problems, as implemented in the simpleFoam solver of OpenFOAM.

2.4.2 SCALARTRANSPORT algorithm

The scalarTransportFoam solver is designed to evolve a passive scalar field T by solving a generic transport equation that accounts for advection, diffusion, and optional source terms. The governing equation can be expressed as:

$$\frac{\partial}{\partial t}(T) + \nabla \cdot (uT) - \nabla \cdot (D_T \nabla T) = S_T \tag{2.13}$$

Where T is the transported scalar, u is the velocity field provided by an external flow solver (simpleFOAM), D_T is the scalar thermal diffusivity, and S_T represents a volumetric source or sink term.

The discretized form of transport equation is solved using finite volume method where:

- convection term $\nabla \cdot (uT)$ is approximated using upwind or linear schemes.
- diffusion term $\nabla \cdot (D_T \nabla \mathrm{T})$ is discretized with central differencing.
- Optional source terms S_T are included as explicit volumetric contributions.

The algorithm iteratively updates the scalar field T until convergence, ensuring conservation of the scalar quantity throughout the computational domain. This makes scalarTransportFoam particularly suitable for simulating heat or species transport in a prescribed flow field.

2.4.3 Turbulence model

To properly model the turbulent regime, selecting an appropriate turbulence model is a crucial step, as several formulations exist, each with different strengths and limitations depending on the type of flow under study. In this work, the Menter SST (Shear Stress Transport) k–ω model was adopted, as implemented in OpenFOAM v2412. This model belongs to the class of two-equation turbulence models, where two additional transport equations are solved: one for the turbulent kinetic energy (k):

$$\frac{D}{D_t}(\rho k) = \nabla \cdot (\rho D_k \nabla k) + \rho G - \frac{2}{3}\rho k(\nabla \cdot u) - \rho \beta^* \omega k + S_k \tag{2.14}$$

- $\frac{D}{D_t}(\rho k)$ is the material derivative of turbulent kinetic energy. It represents the temporal and convective change of k following the fluid motion.
- $\nabla \cdot (\rho D_k \nabla k)$ is the turbulent diffusion term. It accounts for the diffusion transport of k due to both molecular viscosity and turbulent viscosity.
- ρG is the production term. Represents the generation of turbulent kinetic energy due to velocity gradients (shear).
- $-\frac{2}{3}\rho k(\nabla \cdot u)$ is the dilatation term, which accounts for compressibility effects, so it has been neglected in this study.
- $\rho \beta^* \omega k$ is the dissipation term that describes the conversion of turbulent kinetic energy into internal energy through viscous effects.
- S_k is the additional source term. In OpenFOAM, it is typically set to zero.

and another for the specific dissipation rate (ω):

$$\frac{D}{D_t}(\rho \omega) = \nabla \cdot (\rho D_\omega \nabla \omega) + \frac{\rho \gamma G}{\nu} - \frac{2}{3}\rho \gamma \omega(\nabla \cdot u) - \rho \beta \omega^2 - \rho(F_1 - 1)CD_{k\omega} + S_\omega \tag{2.15}$$

- $\nabla \cdot (\rho D_\omega \nabla \omega)$ is the diffusion of ω, analogous to the diffusion term in k equation but with different coefficients.
- $\frac{\rho \gamma G}{\nu}$ is the production of ω, representing the generation of ω in proportion to the production of k.
- $\rho \beta \omega^2$ represents the dissipation of ω, describing the decay of ω due to turbulence itself.
- $\rho(F_1 - 1)CD_{k\omega}$ is the cross-diffusion term, one of the fundamental features of the SST formulation: F_1 is the so-called blending function that switches between $k - \omega$ and $k - \epsilon$ behaviours as it is shown in Figure 2.9 [13].

Blending function has a value of $0 < F < 1$. If F=0 it behaves like $k - \epsilon$, if F=1 it behaves like $k - \omega$.

- S_ω is the additional term

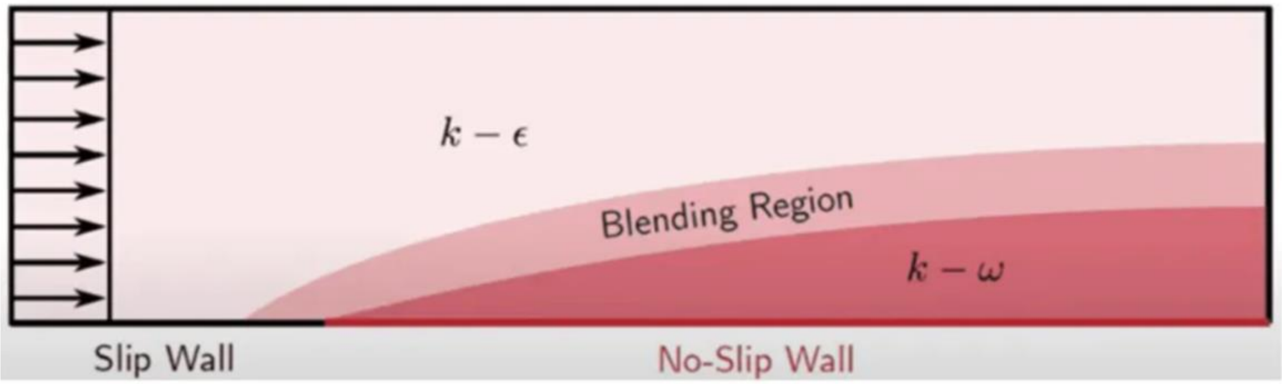

Figure 2.9: SST model switches between

The Menter SST model was specifically developed to combine the advantages of both the k–ε and the standard k–ω formulations. It addresses one of the main weaknesses of the classical k–ω model, namely its excessive sensitivity to the freestream values of ω, which can lead to inaccurate predictions in regions far from solid boundaries. By introducing a blending function that smoothly transitions between the k–ω model near the walls and the k–ε model in the outer regions of the flow, the SST formulation ensures better stability and reliability across the entire domain.

Moreover, the Menter SST model is known for its superior capability to predict flow separation and adverse pressure gradient effects, which are critical in complex geometries such as corrugated or sinusoidal channels. Its accurate near-wall treatment makes it suitable for solving boundary layer behavior without requiring excessively fine grids, thus providing a good balance between accuracy and computational efficiency. For these reasons, it represents an optimal choice for the present study, where the interaction between separated flow regions and wall heat transfer is of primary importance.

A fundamental parameter that tells if the turbulence model is followed correctly is the wall unit *y+:* is a non-dimensional wall distance that tells how deep the first grid point sits inside the turbulent boundary layer. It is defined as:

$$y^{+} = \frac{u_{\tau} y}{\nu} \tag{2.16}$$

Where y is the distance from the wall to the center of the first cell, ν is the kinematic viscosity, and $u_{\tau} = \sqrt{\frac{\tau_{wall}}{\rho}}$ is the friction velocity based on the wall shear stress τ_{wall} and density ρ. In physical terms, y+ partitions the near-wall region into the viscous sublayer (y+ $\lesssim$ 5), the buffer layer (5 $\lesssim$ y+ $\lesssim$ 30), and the logarithmic layer (y+ $\gtrsim$ 30), as can be seen in Figure 2.10 [14]. A lower y+ means you are directly resolving the steep velocity and temperature gradients at the wall; a higher y+ means you are relying more on modeling assumptions to represent them.

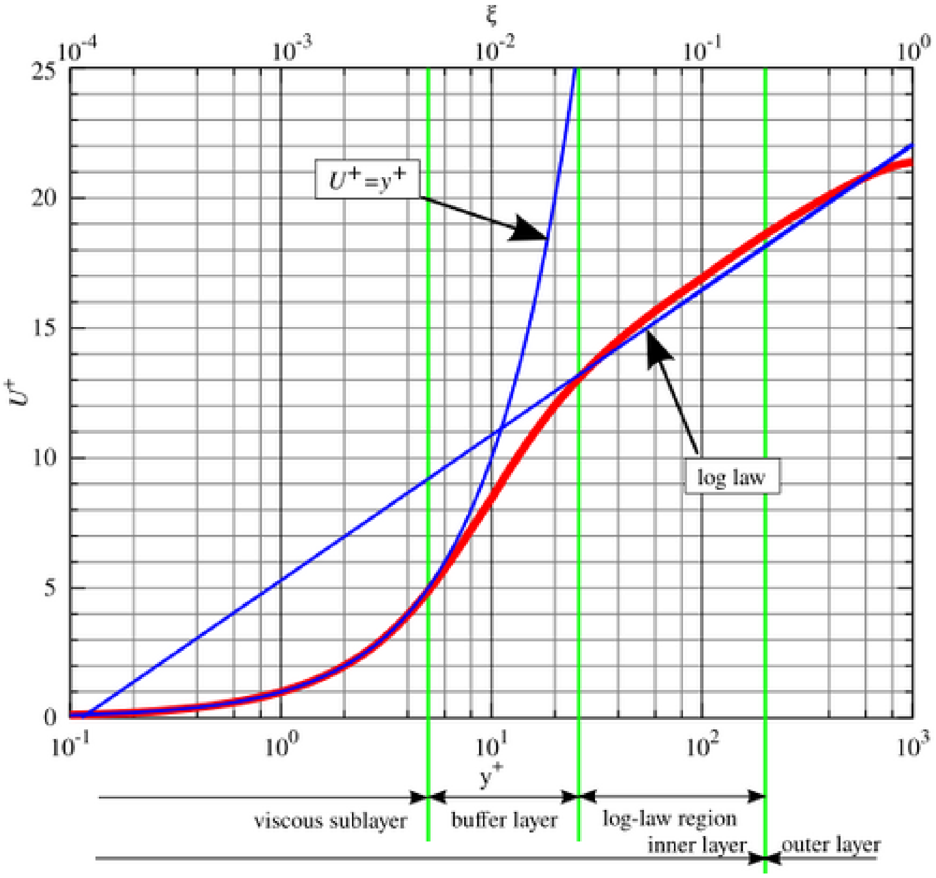

Figure 2.10: Law of the wall

This matters especially when using the Menter k–ω SST turbulence model. SST blends k–ω near the wall with k–ε away from the wall, but it is formulated to be integrated all the way to the wall without wall functions. To honor that design, the mesh should place the first cell inside the viscous sublayer, typically targeting $y^+<1$. With low y^+, the ω-equation's near-wall dissipation and the k-equation's production by mean shear are resolved where their gradients are sharpest; the model evaluates the correct balance of production and destruction. As a result, predictions of wall shear stress, skin-friction coefficient, and heat flux (hence friction factor and Nusselt number) are significantly more reliable.

2.5 Exploit shift-symmetry and periodicity

The concept of shift symmetry (also known as translational symmetry) plays a key role in this work. This type of symmetry describes the property of a system that remains unchanged when it is shifted by a certain amount along a spatial or temporal coordinate.

If a function $f(t)$ describes the structure or response of a system, *shift symmetry* means that:

$$f(t+T_0)=f(t) \tag{2.17}$$

or sometimes

$$f(t+T_0)=-f(t) \tag{2.18}$$

for a fixed translation T_0, that in this case will be half wavelength.

In other words, the system's configuration or output repeats (or inverts) after a specific shift. This periodic or half-wave symmetry is particularly common in systems governed by sinusoidal behaviour.

For example:

- If the channel wall shape is defined by a sinusoidal function, shifting it horizontally by one full wavelength results in an identical geometry (periodicity).
- Shifting by half a wavelength may produce an inverted geometry that is still dynamically equivalent, depending on the boundary conditions (shift-symmetry)

By validating the shift symmetry for the analyzed configurations, it is possible to restrict the post processing to only half of the computational domain without losing accuracy or generality. In Figure 2.11 there is a qualitative comparison between what happens in theory and what happens in this work:

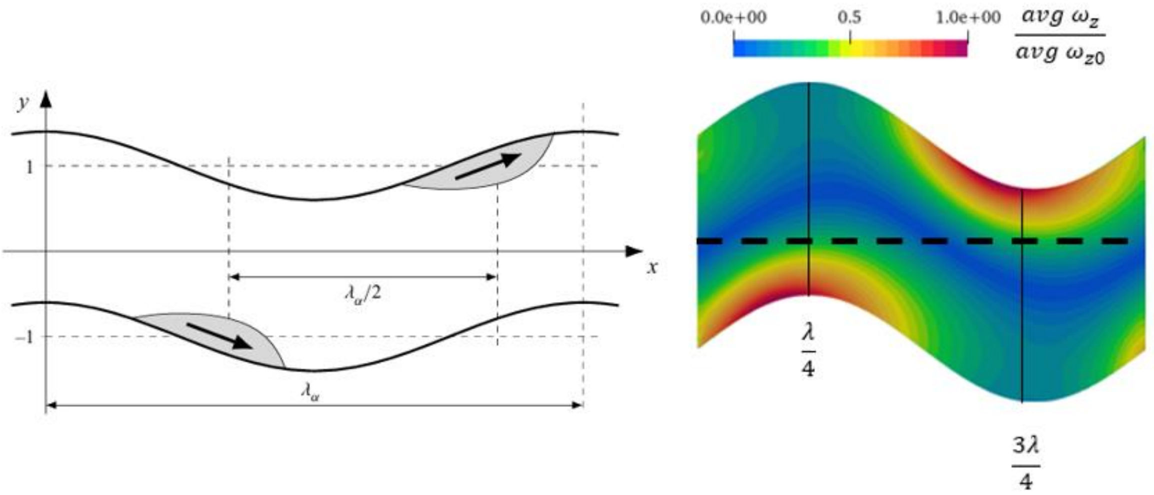

Figure 2.11: Shift-symmetry

To assess the accuracy of the shift symmetry in the sinusoidal channel simulations, the relative error in the vorticity along the wall-normal direction (y) was evaluated. The procedure followed these steps:

1. The lower half of the computational domain was translated by $\frac{\lambda}{2}$ in the streamwise direction and rotated by 180°, effectively mapping it onto the upper half of the domain.
2. A line was traced along the y-direction at $x = \frac{3\lambda}{4}$, to allow a pointwise comparison between corresponding locations in the two halves of the domain.
3. At each point along the line, the relative difference between the original vorticity and the transformed vorticity was computed:

$$\epsilon_{rel}(y)[\%] = \frac{|\ \omega_z^{\text{original}}(y) - \omega_z^{\text{transformed}}(y)\ |}{\omega_z^{original}(y)} 100 \qquad (2.19)$$

4. Results were plotted as a function of y in Figure 2.12. Relative error was found to be approximately constant and very close to zero throughout the domain, confirming that the mesh is symmetric and that the shift symmetry is accurately preserved:

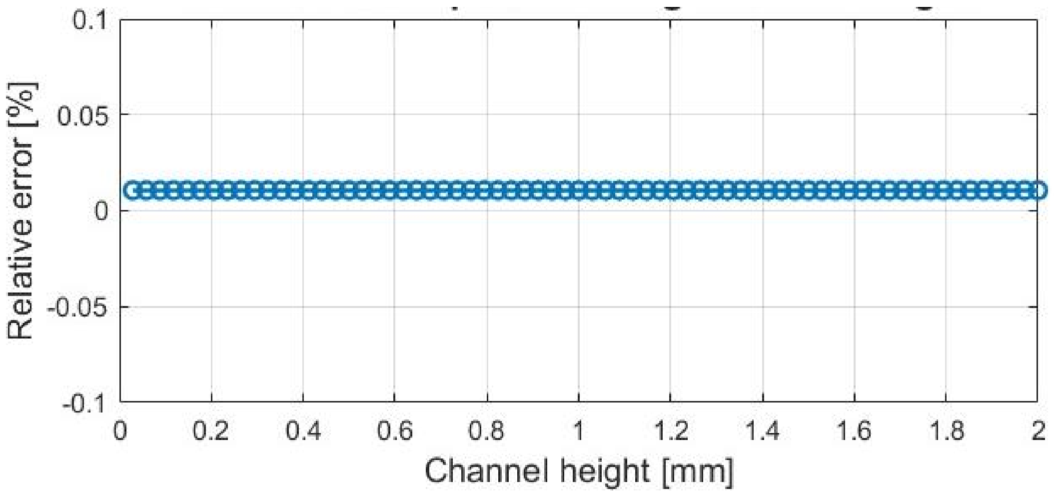

Figure 2.12: Relative error of shift-symmetry approximation along y

This validation demonstrates that it is legitimate to analyze only half of the domain in subsequent post-processing, as the flow properties are effectively mirrored and shifted.

About periodicity, it is important to validate it to guarantee that flow structures, pressure, and velocity fields repeat consistently across the boundaries, preventing artificial discontinuities. Validating the periodicity of the domain was essential to ensure that the flow reached hydrodynamically and thermally fully developed conditions within a single wavelength of the sinusoidal geometry. Figure 2.13 [15] shows what happens theoretically.

This validation allows each simulation to be performed on only one geometric period, significantly reducing computational cost while maintaining physical accuracy. It also ensures that the results obtained within this reduced domain are fully representative of the repeating flow behavior along the entire channel.

In OpenFOAM, hydraulically fully developed conditions can be imposed by applying periodic boundary conditions at the inlet and outlet of the computational domain, while enforcing a specified mean velocity along the channel through an *fvOptions* source term. Conversely, the thermally fully developed conditions can be implemented using a custom boundary condition written in Python to ensure that the thermal field exhibits periodic behavior consistent with hydrodynamic development. Before applying it to corrugated cases, it’s important to validate it with the simpler case.

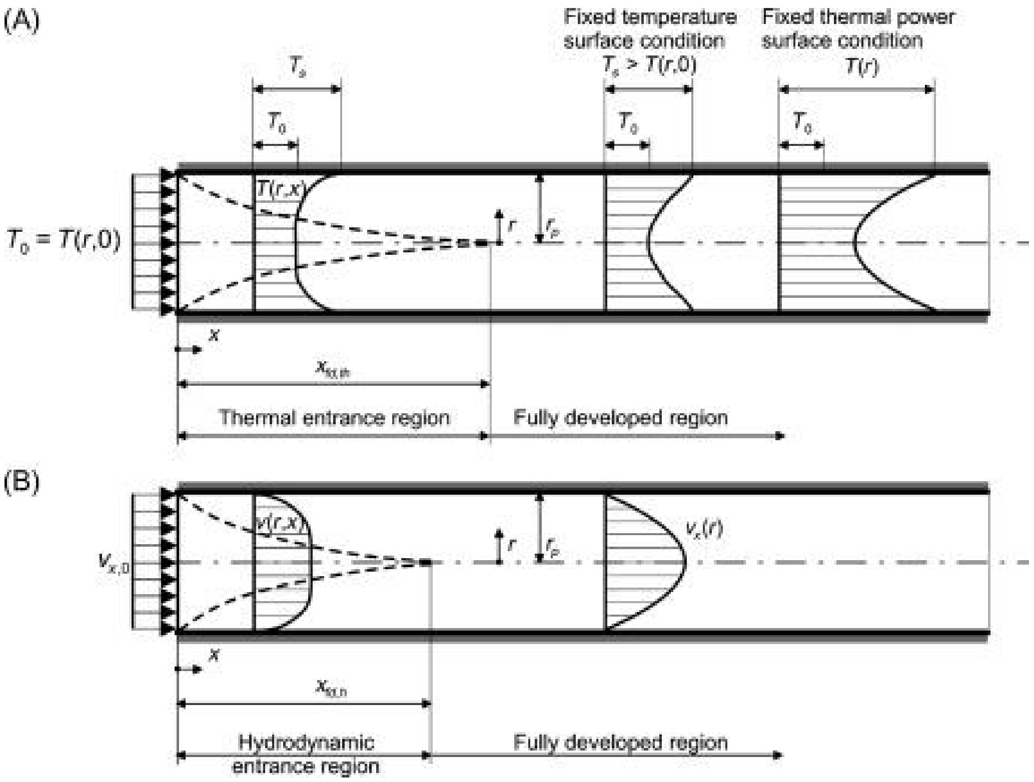

Figure 2.13: Graphical representation of flow development

For thermal cases, the imposed temperature boundary condition was taken to calculate dimensionless temperature profiles:

$$\theta^* = \frac{T(x,y) - T_w}{T_b - T_w} \tag{2.20}$$

With T_b = bulk temperature and T_w = wall temperature.

In Figure 2.14 and 2.15 velocity profile and dimensionless temperature for the parallel flat plates case and sinusoidal channel are shown to prove periodicity.

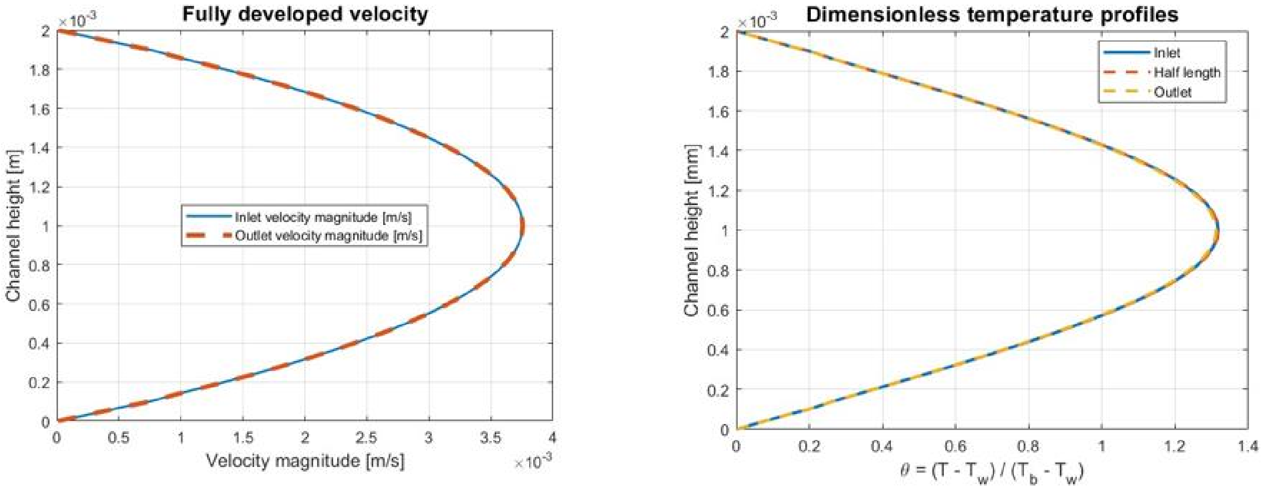

Figure 2.14: fully developed conditions for parallel flat plates

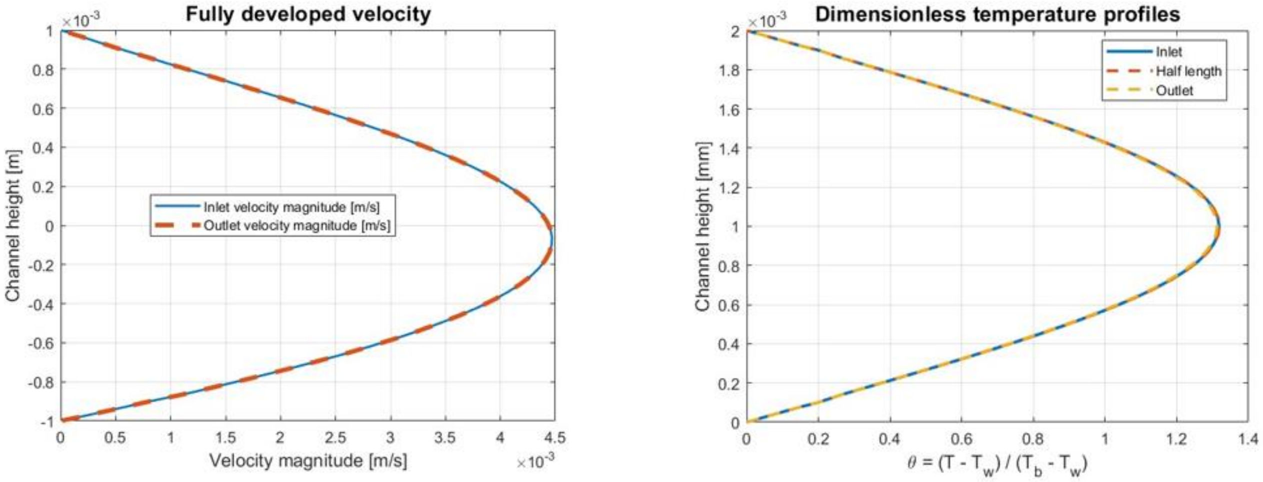

Figure 2.15: fully developed condition for sinusoidal flow

3 Results

In this chapter, the main quantities characterizing the flow and heat transfer within the sinusoidal channels are presented and analyzed. The quantities of interest are the vorticity, the friction factor, and the Nusselt number.

The following sections present qualitative results for all the simulated geometries. Subsequently, in Chapter 4, correlations between the normalized vorticity, friction factor, and Nusselt number will be investigated to identify possible relationships linking the hydrodynamic and thermal behaviors of the sinusoidal channels.

Qualitative plots are normalized by the highest value in the corresponding figure to have a clearer comparison.

3.1 Laminar regime

3.1.1 Hydraulic results

This section presents the hydrodynamic results obtained for the nine sinusoidal channel configurations in the Reynolds number range between 10 and 500. The analysis focuses on the behavior of the flow field, with particular attention to the evolution of the velocity and vorticity field. These quantities provide insight into how the geometric parameters of the sinusoidal walls affect the flow structure, energy dissipation, and pressure losses.

The sinusoidal corrugation introduces periodic accelerations and decelerations in the flow, promoting the formation of vortical structures and local recirculation whose intensity depends on both the Reynolds number and the degree of corrugation. By comparing the results across all configurations, it is possible to evaluate how the hydrodynamic response of the channel evolves from low to moderate Reynolds numbers and how geometric modifications influence the overall flow resistance.

The first part of this analysis focus on the effect of wall corrugation on vorticity enhancement.

The effect of the wall corrugation on the internal flow was investigated by analyzing the velocity field obtained from the numerical simulations. Increasing the corrugation parameter α causes significant modifications in the flow behavior within the sinusoidal channels. As the walls become wavier, the local cross-sectional area varies more markedly along the streamwise direction, leading to alternating regions of flow acceleration and deceleration.

For low corrugation levels (Figure 3.1a), velocity along x remains relatively smooth and the flow follows the channel contour without noticeable disturbances. When α increases (Figure 3.1b, c), however, the stronger wall curvature promotes the onset of local recirculation zones in the troughs and a clear acceleration of the fluid along the crests. These effects result in a more complex velocity distribution along x, with higher spatial gradients and enhanced mixing near the wall.

Figure 3.1 shows how the velocity field progressively evolves with increasing corrugation, providing a visual representation of the transition from a nearly uniform flow to a more structured and dynamic one.

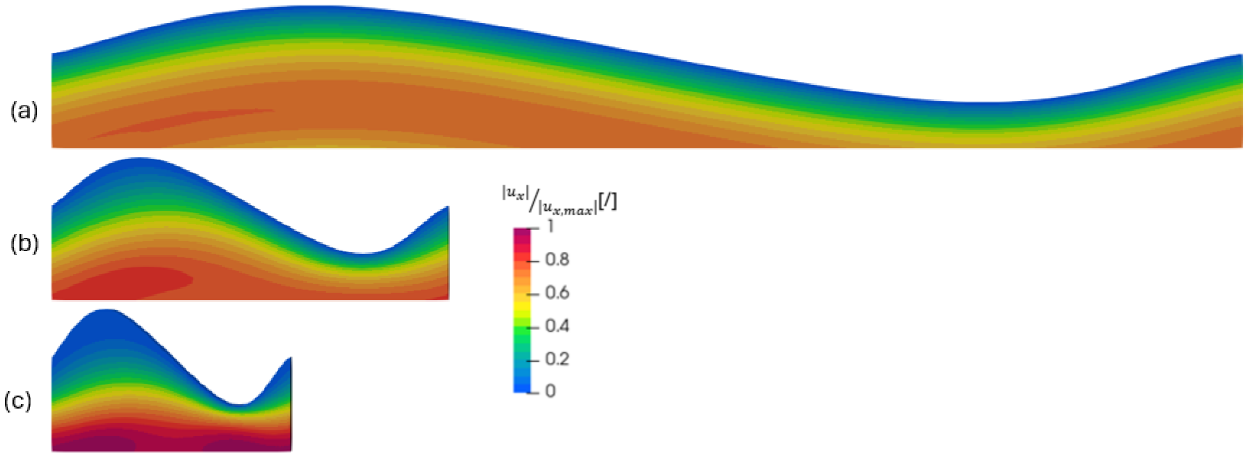

Figure 3.1: $|u_x|$ distribution at Re=10 for S=0.5 mm(a) $\alpha = 0.5$ (b) $\alpha = 1.5$ (c) $\alpha = 2.5$

Regarding vertical component of velocity (Figure 3.2): results indicate that $|u_y|$ exhibits a trend analogous to that of the streamwise component: its magnitude increases as the corrugation number (α) increases. This behavior is associated with the stronger curvature of the channel walls, which induces more pronounced flow deviation from the main direction and enhances the formation of 3 more accentuated local recirculation zones.

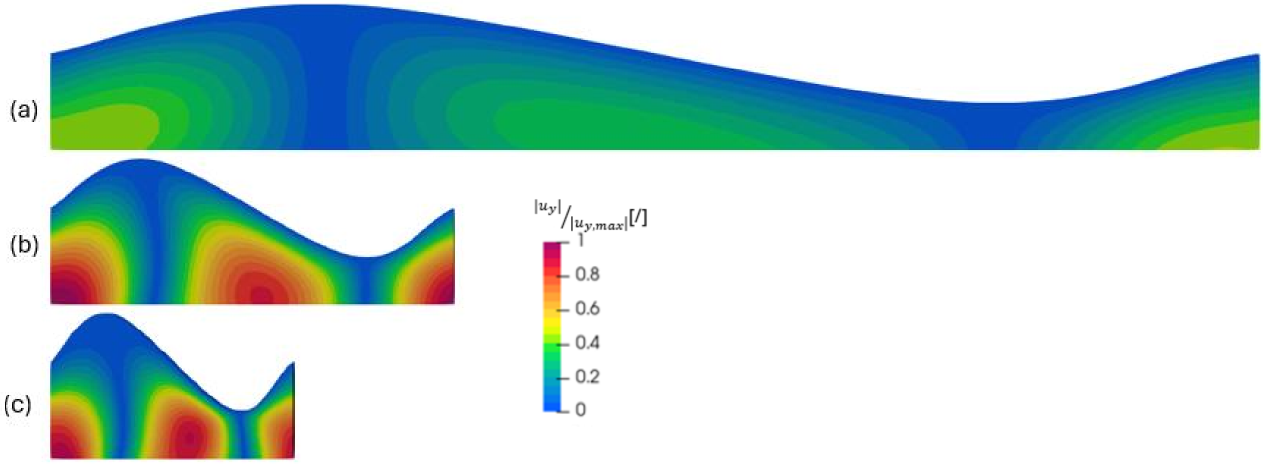

Figure 3.2: $|u_y|$ distribution at Re=10 for S=0.5 mm(a) $\alpha = 0.5$ (b) $\alpha = 1.5$ (c) $\alpha = 2.5$

The modification of the velocity field with increasing corrugation is directly reflected in the distribution of vorticity inside the channel. As the parameter α grows, the stronger wall curvature and the alternation of expansion and contraction zones generate intense shear layers near the walls and within the recirculation regions. These shear layers are responsible for the increase in local vorticity, especially in the vicinity of the troughs where the flow separates and reattaches periodically.

At low corrugation levels (Figure 3.3a), vorticity (shown in log scale for better comprehension) is mainly confined close to the walls, with a relatively smooth and symmetric distribution between the upper and lower surfaces. When α increases (Figure 3.3b, c), distinct vortical structures appear within the cavities, becoming larger and more energetic as the corrugation amplitude grows. This behavior indicates a progressive enhancement of fluid mixing and momentum exchange across the cross-section.

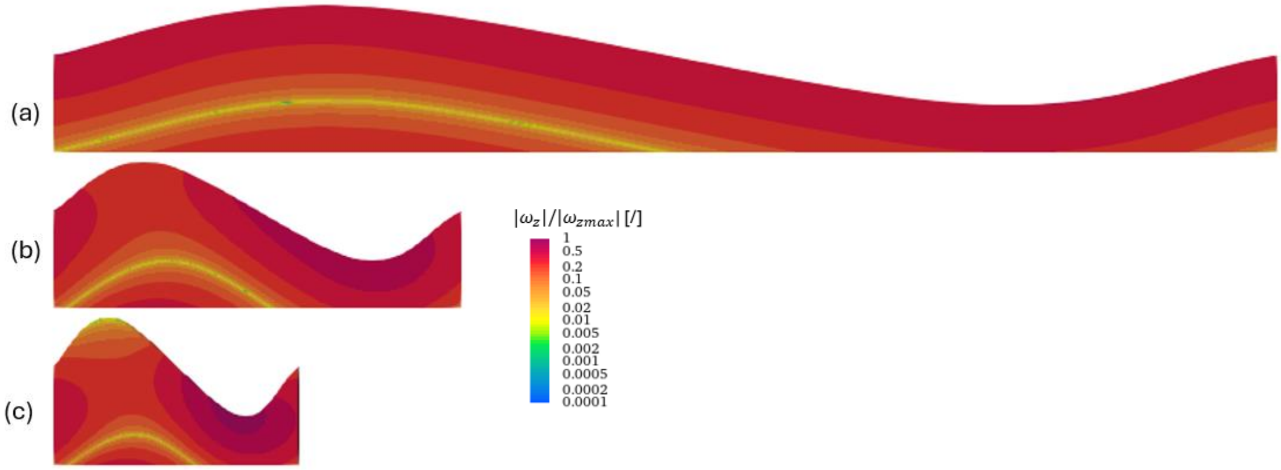

Figure 3.3: $|\omega_z|$ distribution at Re=10 for S=0.5 mm (a) $\alpha = 0.5$ (b) $\alpha = 1.5$ (c) $\alpha = 2.5$

The amplitude of the sinusoidal corrugation plays a key role in determining the intensity of the flow disturbances within the channel. As *S* increases, the wall deformation becomes more pronounced, causing larger variations in the local cross-section and stronger curvature effects along the streamwise direction.

Figure 3.4 illustrates how the increase in S influences the overall flow organization and the development of vortical structures inside the sinusoidal channels.

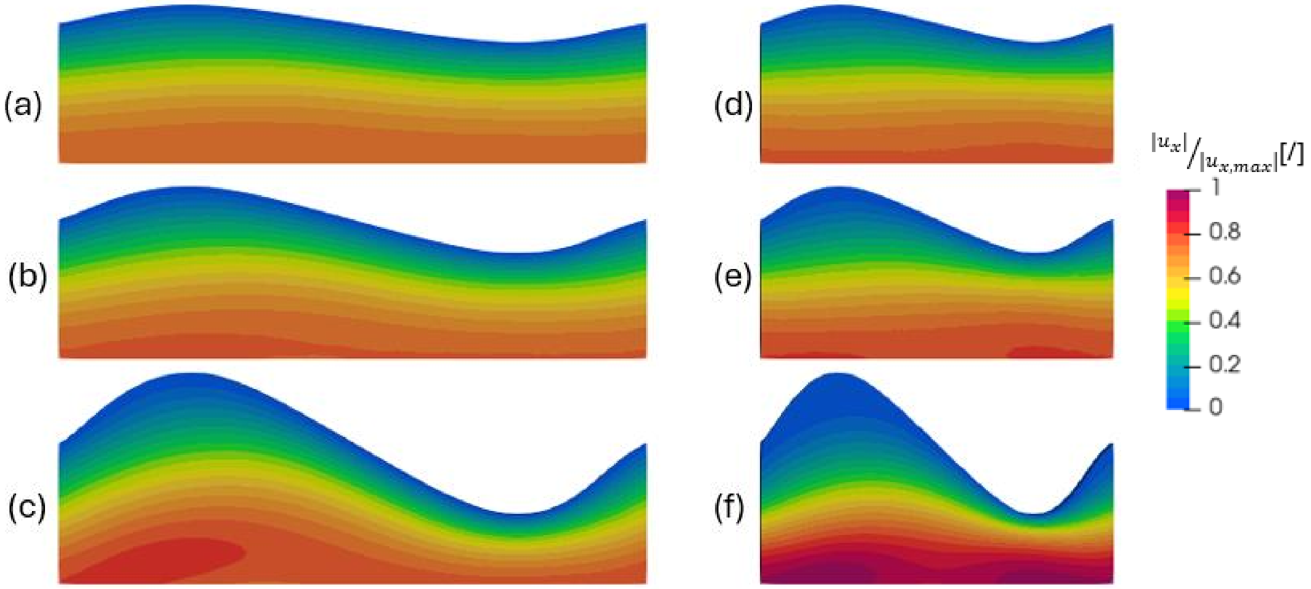

Figure 3.4: u_x distribution at Re=10 for: $\alpha = 1.5\ (a)\ S = 0.13\ mm\ (b)\ S = 0.235\ mm\ (c)\ S = 0.5\ mm;\ \alpha = 2.5, (d)\ S = 0.13\ mm, (e)\ S = 0.235\ mm\ (f)\ S = 0.5\ mm$

The comparison clearly shows that increasing the corrugation amplitude *S* strongly affects the velocity distribution inside the sinusoidal channels. For both values of the corrugation parameter α, a larger amplitude leads to a more pronounced modulation of the flow field. At low *S* (Figure 3.4a, d), the velocity contours remain relatively parallel to the wall and the flow follows the sinusoidal shape with only slight distortion. As *S* increases to intermediate and high values (Figure 3.4b–c, e–f), the constriction of the upper region and the expansion of the lower region promote local flow acceleration near the crests and the formation of low-velocity zones or weak recirculation within the troughs. The distribution of the transverse velocity component provides further insight into how the flow structure evolves as the corrugation amplitude S increases. For both corrugation numbers, low S values (Figure 3.5a, d) correspond to a nearly one-dimensional flow, with negligible lateral motion and uniform velocity contours. When S increases (Figure 3.5b, c, e, f), the deformation of the channel walls promotes the development of strong transverse velocity components, especially near the troughs where the flow decelerates and secondary recirculation appears.

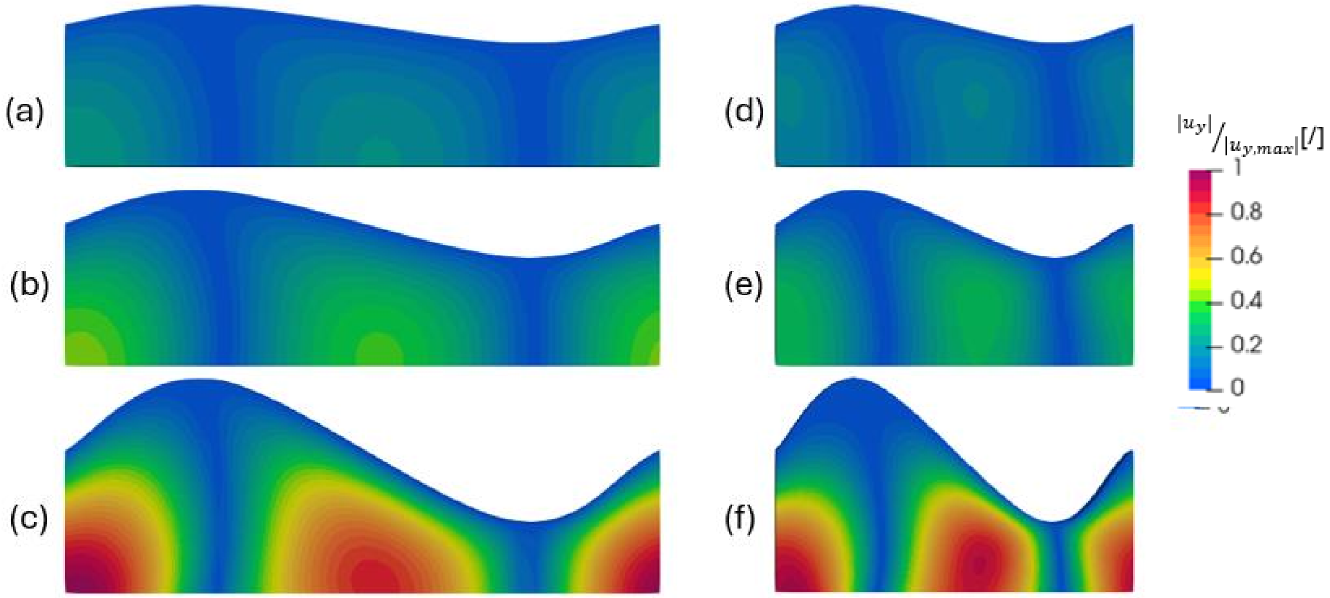

Figure 3.5: $|u_y|$ distribution at Re=10 for: $\alpha = 1.5\ (a)\ S = 0.13\ mm\ (b)\ S = 0.235\ mm\ (c)\ S = 0.5\ mm;\ \alpha = 2.5, (d)\ S = 0.13\ mm, (e)\ S = 0.235\ mm\ (f)\ S = 0.5\ mm$

In the most corrugated configurations (Figure 3.5c, f), the $|u_y|$ distribution highlights the presence of well-defined counter-rotating vortices that occupy a large portion of the cross-section. These vortical structures are more intense for α = 2.5, indicating that both the corrugation amplitude and the wall curvature contribute to the generation of secondary motions. The resulting increase in lateral velocity components enhances mixing and momentum exchange between the core flow and the near-wall regions.

The vorticity distribution (Figure 3.6) reveals how the wall corrugation significantly modifies the near-wall flow behavior. In the less corrugated channels (Figure 3.6a, d), the vorticity close to the upper wall is relatively low but remains nearly uniform along the streamwise direction. This indicates a stable shear layer, typical of a smooth-wall configuration, where the velocity gradients are weakly affected by the wall geometry.

As the corrugation amplitude increases (Figure 3.6b, c, e, f), distinct peaks of vorticity appear in correspondence with the sinusoidal crests and troughs, where the flow accelerates and decelerates, respectively. These local peaks reflect strong velocity gradients generated by flow separation and reattachment phenomena. At the same time, lower-vorticity zones can be observed in the regions corresponding to the bulging parts of the wall, where the flow tends to slow down and recirculate.

Overall, the results highlight that wall corrugation enhances the spatial variability of the vorticity field: instead of a uniform shear layer, the flow develops alternating high- and low-vorticity regions following the sinusoidal pattern of the channel, leading to more complex near-wall dynamics and stronger local mixing.

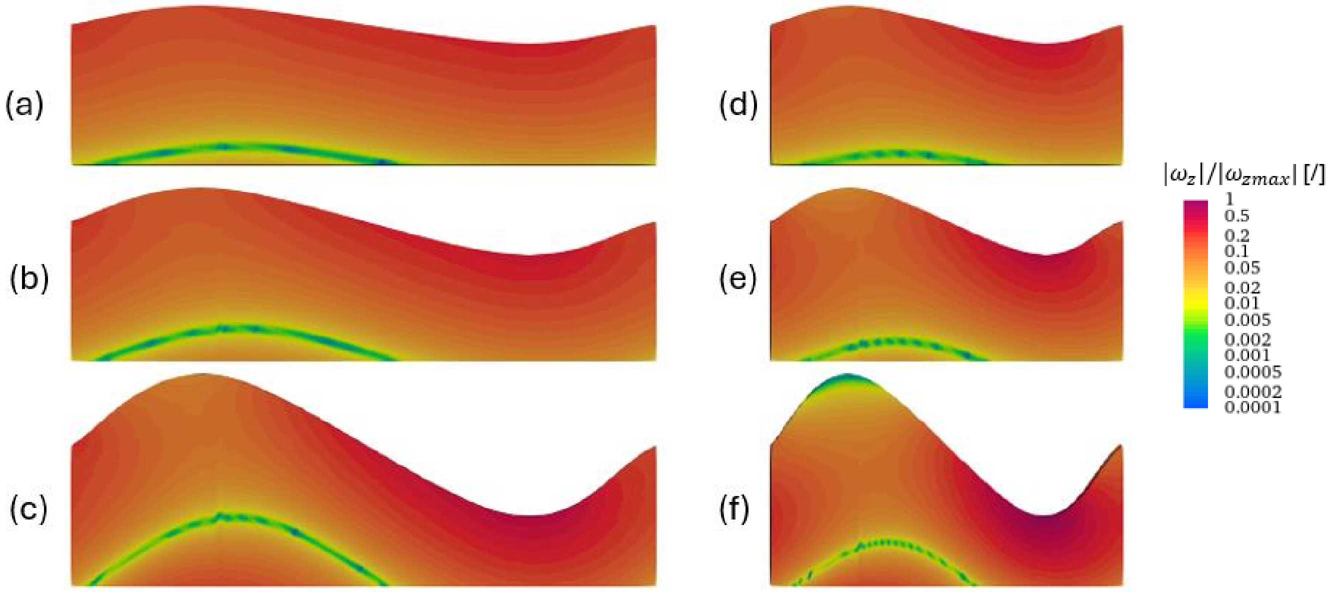

Figure 3.6: $|\omega_z|$ distribution at Re=10 for: $\alpha = 1.5\ (a)\ S = 0.13\ mm\ (b)\ S = 0.235\ mm\ (c)\ S = 0.5\ mm;\ \alpha = 2.5, (d)\ S = 0.13\ mm, (e)\ S = 0.235\ mm\ (f)\ S = 0.5\ mm$

Now, qualitative results are shown varying Reynolds number (without changing the mean velocity) while keeping the geometry and boundary conditions unchanged, to isolate the effects of inertia on the velocity and vorticity distributions. Figure 3.7 illustrates the progressive evolution of the velocity and vorticity fields highlighting the transition from a stable laminar regime to a more complex and dynamically structured flow.

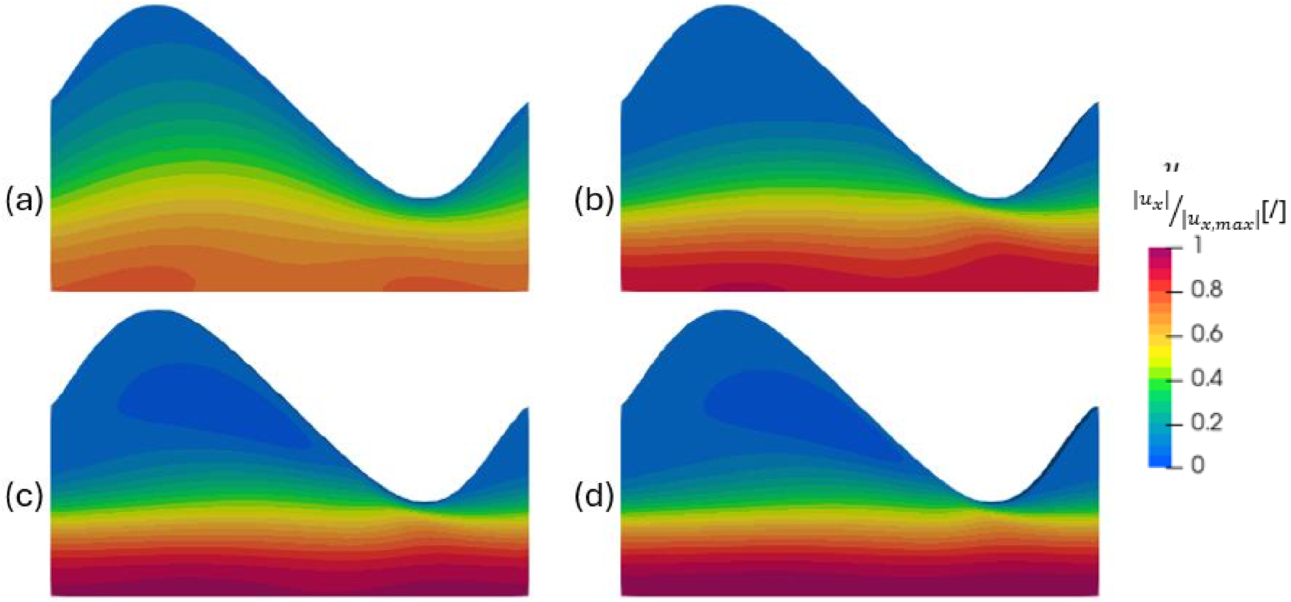

Figure 3.7: $|u_x|$ distribution for $\alpha = 2.5$, S=0.5 mm: (a) Re=10 (b) Re=100 (c) Re=300 (d) Re=500

Streamwise velocity shows how the flow structure evolves with the Reynolds number in the most corrugated configuration. At low Reynolds numbers (Figure 3.7a), the velocity distribution closely follows the sinusoidal wall shape with smooth gradients. As Re increases (Figure 3.7b, d), the velocity contours become progressively flatter and more aligned with the streamwise direction, indicating the growing influence of inertia and the reduction of viscous effects. The flow accelerates along the crests and decelerates within the troughs, while the shear layers near the walls become thinner and more localized. This behavior confirms the transition from a viscosity-dominated regime to an inertia-dominated one as the number of Reynolds increases.

Figure 3.8 shows the vertical component of velocity as Re is increased for the most corrugated configuration.

The maps of the normalized transversal velocity component show the progressive reduction of transversal motion with increasing Reynolds number. At low Reynolds numbers (Figure 3.8a), the higher viscosity allows the flow to adapt smoothly to the sinusoidal geometry, generating broad regions of transversal velocity near the wall. As Re increases (Figure 3.8b, c, d), inertial effects become dominant, and the flow tends to remain aligned with the main streamwise direction, resulting in smaller u_y values confined in narrow zones close to the wall curvature. This shows that, for constant mean velocity, higher Reynolds numbers primarily reduce viscous diffusion without amplifying the intensity of transversal motion.

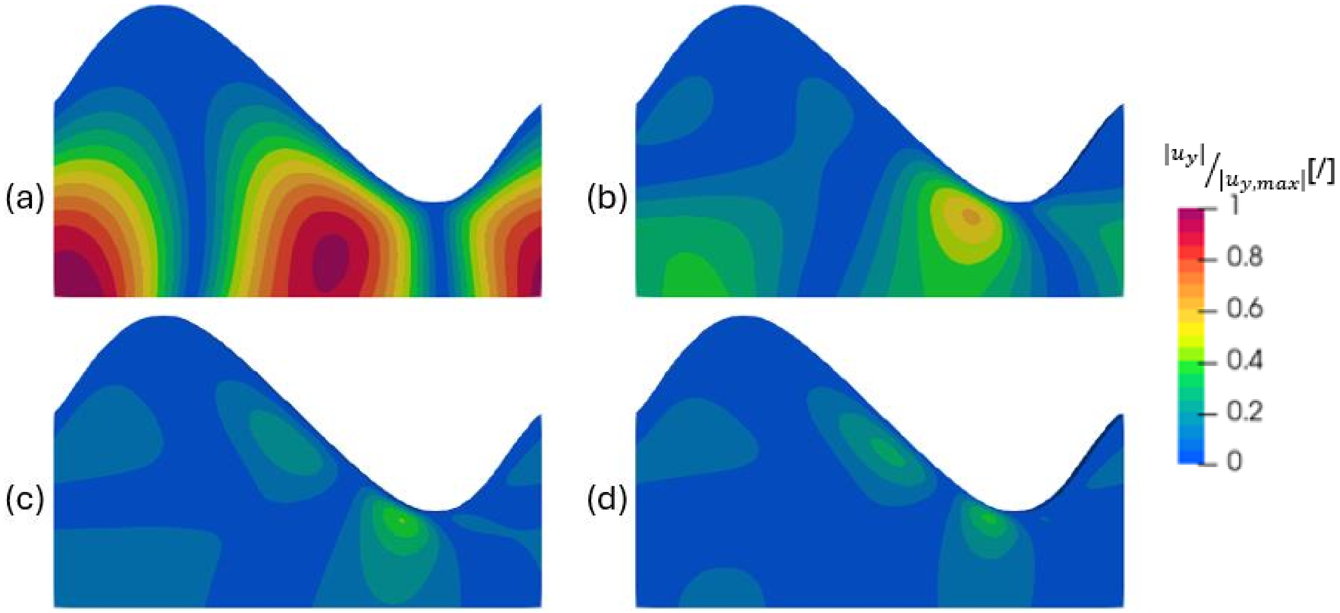

Figure 3.8: normalized $|u_y|$ distribution for $\alpha = 2.5$, S=0.5 mm: (a) Re=10 (b) Re=100 (c) Re=300 (d) Re=500

Vorticity along z reveals how the rotational features of the flow evolve with increasing Reynolds number. At low Reynolds numbers (Figure 3.9a), the vorticity is mainly confined near the wall, forming smooth layers that follow the sinusoidal contour. As the Reynolds number increases (Figure 3.9b, c, d), the vorticity distribution becomes more structured, with thinner and more intense shear layers developing along the curved walls. These localized regions of high vorticity correspond to stronger velocity gradients produced by the alternation of acceleration and deceleration zones along the geometry. At the highest Reynolds number

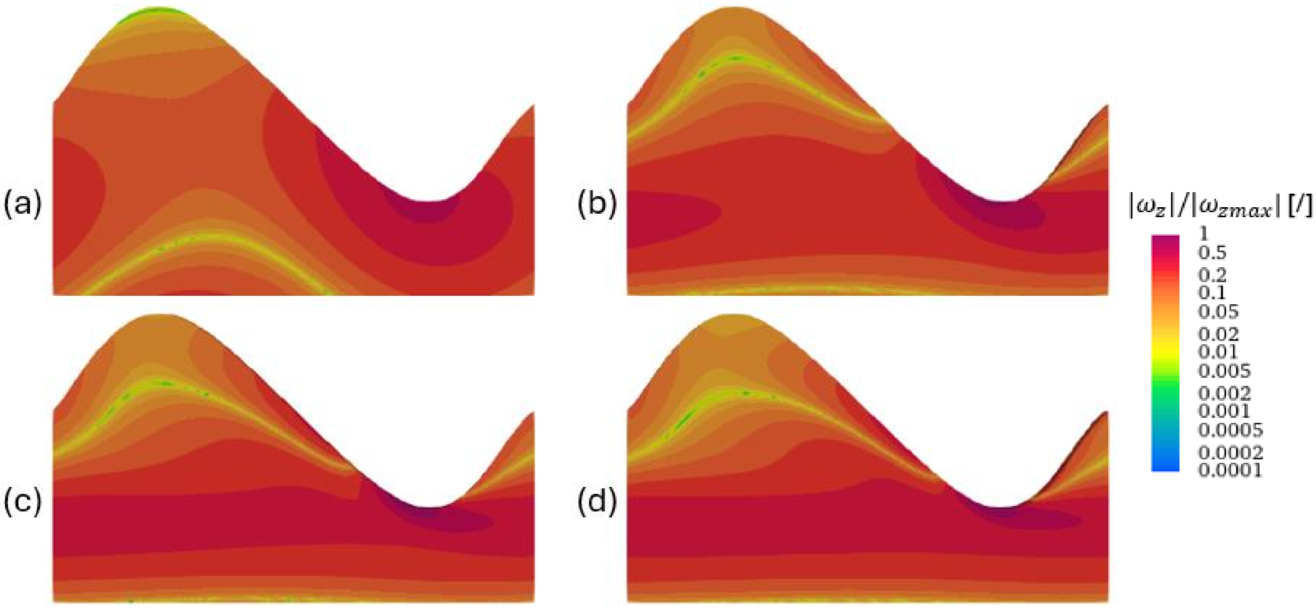

Figure3.9: normalized $|\omega_z|$ distribution for $\alpha = 2.5$, S=0.5 mm: (a) Re=10 (b) Re=100 (c) Re=300 (d) Re=500

(Figure 3.9c, d), the core flow remains mostly irrotational, while the near-wall regions exhibit concentrated bands of vorticity, confirming the progressive dominance of inertial effects and the reduction of viscous diffusion.

In the final part of the hydraulic analysis, the evolution of the flow structures is examined as both the Reynolds number, and the corrugation intensity are increased. The results show that, while at low Reynolds numbers the flow remains attached and follows the sinusoidal wall profile, higher Reynolds numbers promote the formation of recirculation zones (Figure 3.10b, c) within the troughs of the channel. These regions become more pronounced as the wall corrugation increases, enhancing fluid mixing and momentum exchange across the cross-section.

To better illustrate this behavior, streamlines at Re = 500 are compared for different geometries (Figure 3.10): it's evident that this effect will be emphasized with results in turbulent regime.

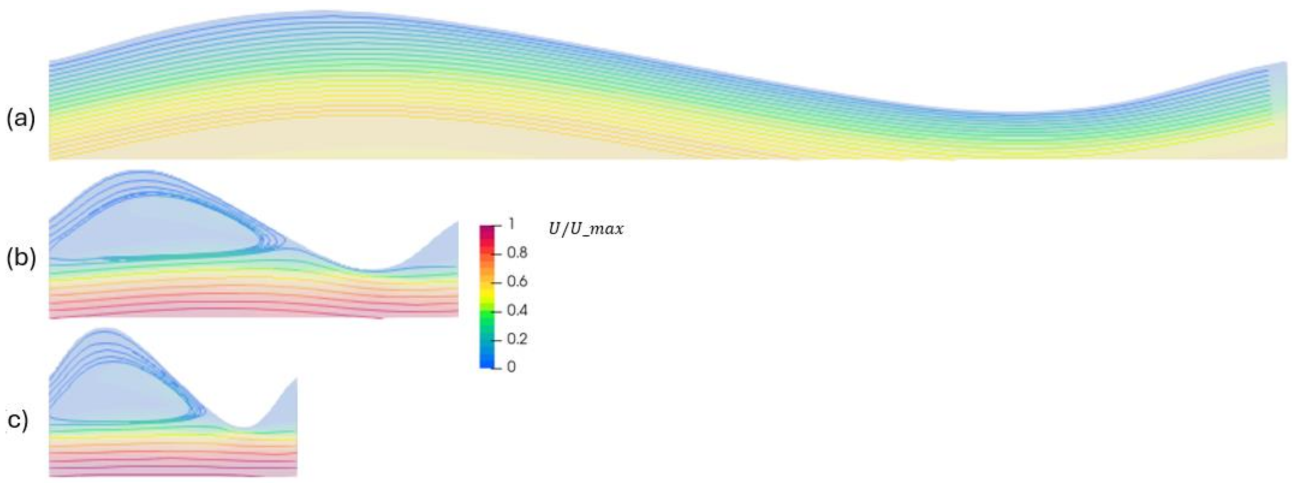

Figure 3.10: streamlines for velocity magnitude at Re=500; S=0.5 mm: (a) $\alpha = 0.5$ (b) $\alpha = 1.5$ (c) $\alpha = 2.5$

3.1.2 Thermal results

In this section, the thermal results are presented considering the two imposed thermal boundary conditions: constant wall temperature and constant heat flux. For each case, the temperature distributions within the sinusoidal channels are analyzed to highlight the influence of the geometric configuration on the heat transfer characteristics. The comparison among different geometries is performed at constant Reynolds number to illustrate how the corrugation affects the thermal field and fluid mixing. Subsequently, for the most corrugated configuration, the effect of the Reynolds number is examined to assess the evolution of thermal behavior with increasing flow inertia. These qualitative results provide an overview of the temperature patterns, while the quantitative evaluation of the heat transfer performance will be discussed in detail in Chapter 4.

3.1.2.1 Imposed temperature BC

As shown in Figure 3.11, at Re = 10 the comparison between the three configurations with S = 0.5 mm varying corrugation number α reveals that, at such low Reynolds numbers, the flow remains completely laminar without any recirculation. This regime corresponds to the so-called purely laminar shear flow region, where the influence of the channel geometry on the heat transfer is negligible. In this condition, the thermal exchange is almost entirely dominated by conduction, and the variations in corrugation do not lead to any significant enhancement of the temperature field.

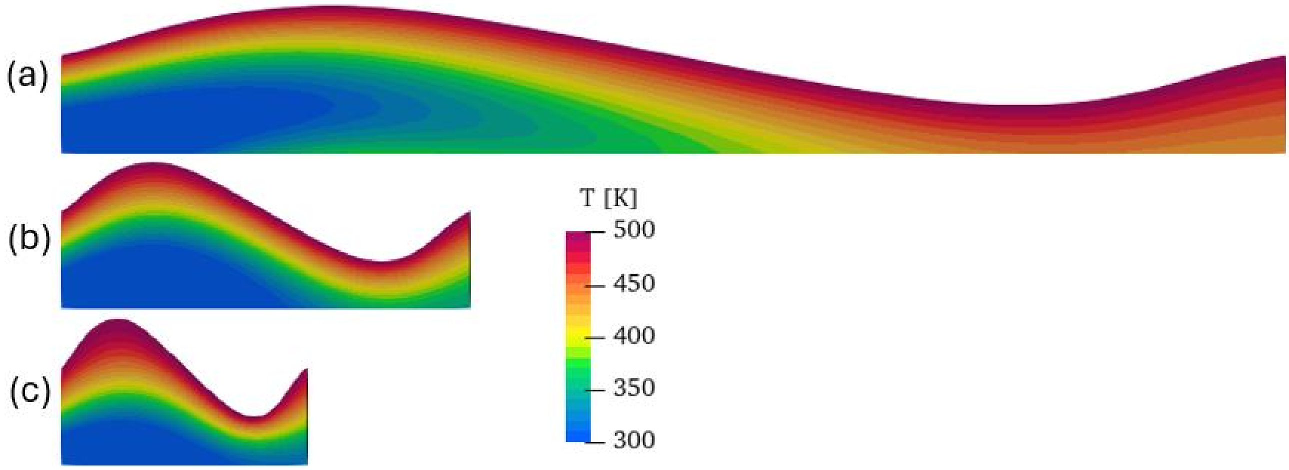

Figure 3.11: Temperature distribution for S=0.5 mm at Re=10: (a) $\alpha = 0.5$ (b) $\alpha = 1.5$ (c) $\alpha = 2.5$

At Re = 500, flow behavior changes significantly compared to the low-Reynolds regime. As shown in Figure 3.12, the higher inertia of the fluid promotes the onset of recirculation zones and stronger secondary flows within the corrugations. These effects enhance fluid mixing and, consequently, improve the convective heat transfer. Overall, comparing $\alpha = 2.5$ and $\alpha = 1.5$ (Figure 3.12b, c), it's not possible to notice great differences.

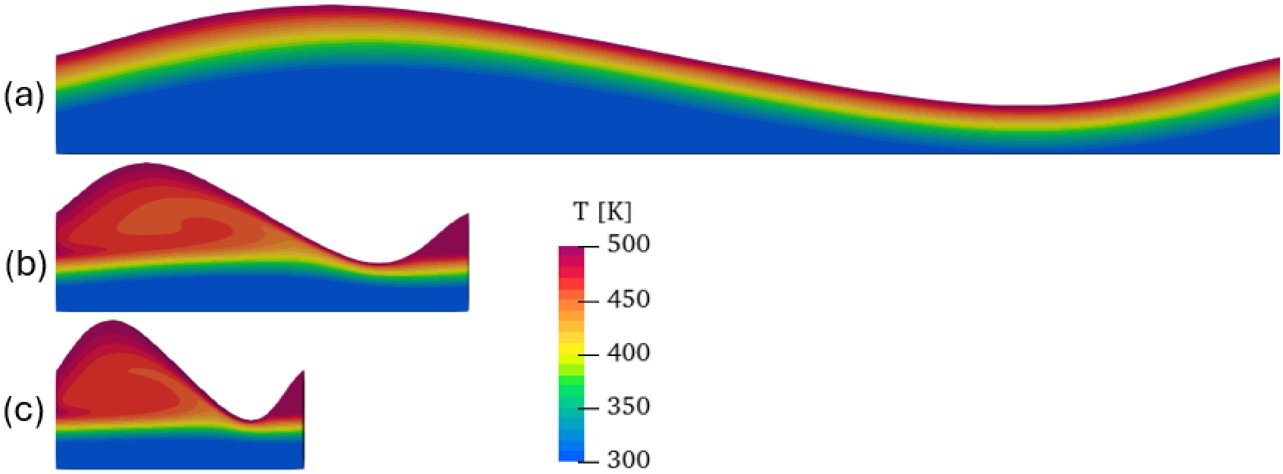

Figure 3.12: Temperature distribution at Re=500 for S=0.5 mm: (a) $\alpha = 0.5$ (b) $\alpha = 1.5$ (c) $\alpha = 2.5$

Figure 3.13 illustrates the temperature distribution for the most corrugated configuration as the Reynolds number increases. To allow a consistent comparison among different Reynolds numbers and operating conditions, the analysis is carried out using the dimensionless temperature θ, defined as

$$\theta = \frac{T(x,y) - T_{min}}{T_{wall} - T_{min}} \tag{3.1}$$

which allows normalizing the thermal results and isolating the influence of the flow regime from the absolute temperature values.

At low Reynolds numbers (Figure 3.13a), the thermal field is mainly governed by conduction, with smooth, stratified temperature gradients developing along the channel and very limited fluid mixing. In this regime, the heat transfer process is dominated by diffusion, and the

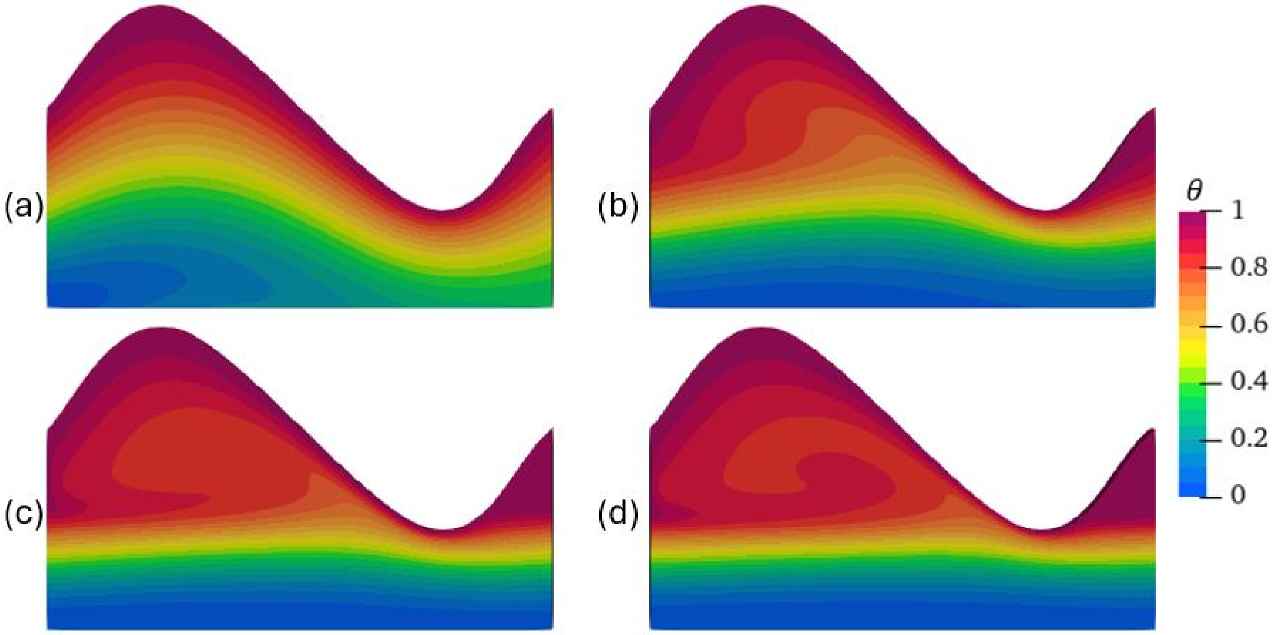

Figure 3.13: Temperature distribution for $\alpha = 2.5$, S=0.5 mm: (a) Re=10 (b) Re=100 (c) Re=300 (d) Re=500

isotherms appear almost parallel to the wall, indicating weak interaction between the core flow and the near-wall region.

As the Reynolds number rises (Figure 3.13c, d), convective transport becomes progressively more important. The increase in flow inertia promotes the onset of vortical structures and recirculation zones within the corrugated cavities, which significantly enhance fluid mixing. This enhanced mixing contributes to a more homogeneous temperature field throughout the channel cross-section, reducing the local temperature gradients and thinning the thermal boundary layer near the walls. Consequently, the overall thermal performance improves as the flow regime transitions from conduction-dominated to convection-dominated behavior.

The progressive change in the temperature distribution with Reynolds number clearly demonstrates the strong dependence of the heat transfer mechanisms on the flow dynamics induced by surface corrugation.

This normalization effectively removes the influence of absolute temperature levels and highlights the spatial variations due solely to the hydrodynamic regime and geometry. In this way, the analysis focuses on the intrinsic flow–thermal coupling, enabling a clearer interpretation of how changes in Reynolds number modify the heat transfer characteristics within the corrugated channel.

3.1.2.2 Imposed heat flux BC

In Figure 3.14, corresponding to the case with constant wall heat flux, the temperature distribution exhibits a progressive increase along the streamwise direction, as expected due to the continuous energy input at the wall. In contrast to the constant wall temperature condition, the thermal field here is characterized by a variable wall temperature that adapts to the local heat transfer rate. For the lowest Reynolds number (Figure 3.14), temperature contours remain smooth and stratified, indicating that heat transfer is still dominated by conduction.

As the Reynolds number increases (Figure 3.15) convective contribution becomes more significant, leading to enhanced mixing and a more uniform temperature field.

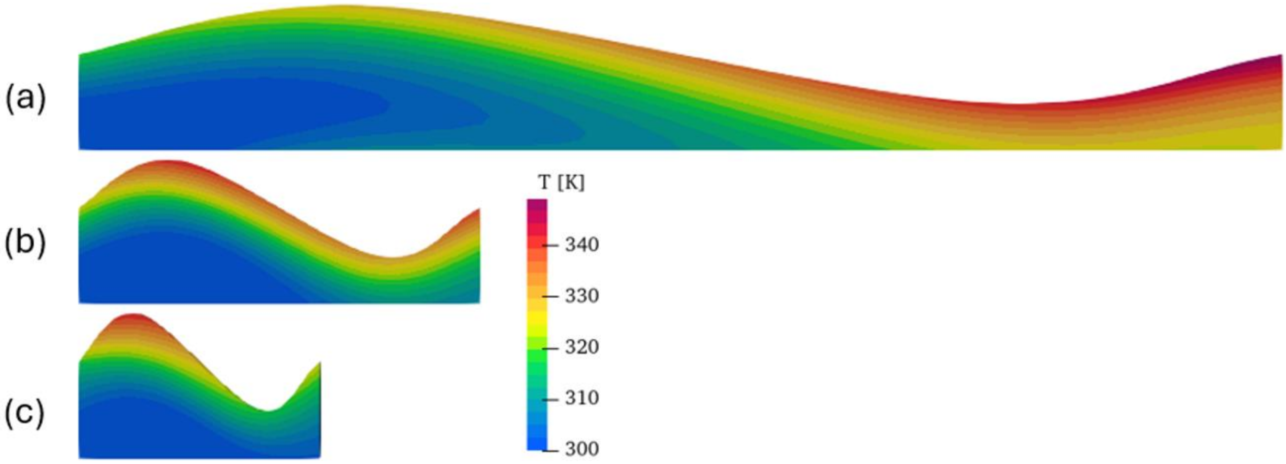

Figure 3.14: Temperature distribution at Re=10 for S=0.5 mm: (a) α=0.5 (b) α=1.5 (c) α=2.5

The comparison has been made again with the dimensionless temperature distribution evaluated in this case as:

$$\theta = \frac{T(x,y) - T_{min}}{T_{wall} - T_{min}} \tag{3.2}$$

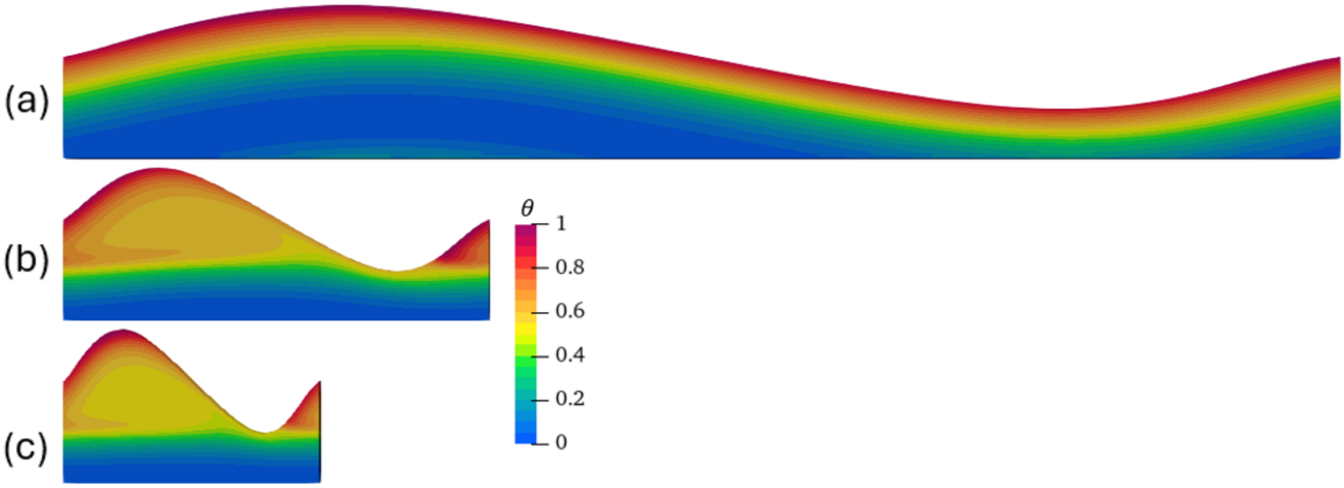

Figure 3.15: Temperature distribution at Re=500 for S=0.5 mm: (a) α=0.5 (b) α=1.5 (c) α=2.5

Compared to the low-Reynolds regime, the flow now exhibits a much stronger convective contribution, which leads to a thinner thermal boundary layer and a more uniform temperature field across the channel. The increase in Reynolds number enhances fluid mixing, particularly in the regions downstream of the corrugation peaks. However, when comparing the two most corrugated configurations (α = 1.5 and α = 2.5), the visual differences in the temperature field appear relatively small. This suggests that under the imposed heat flux condition, the amplitude of the corrugation rather than the corrugation wavenumber may play a more dominant role in

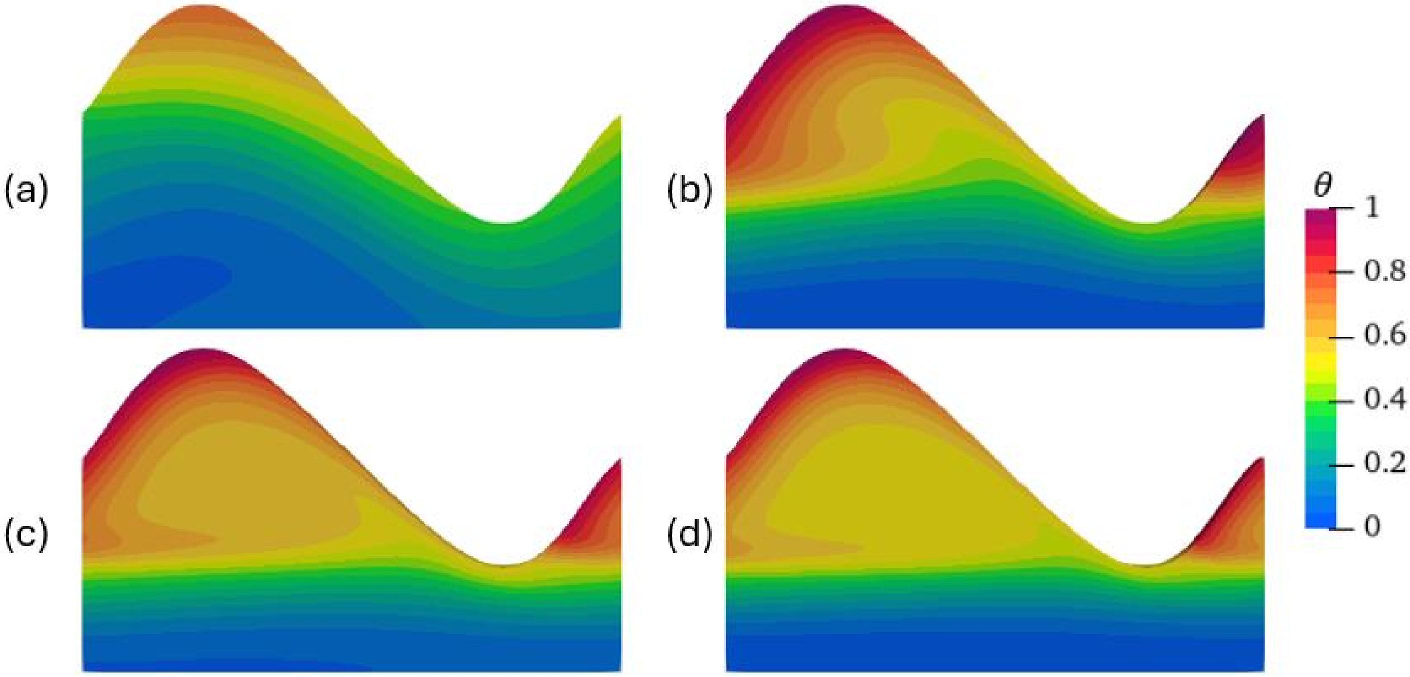

Figure 3.16: Temperature distribution for S=0.5 mm, $\alpha = 2.5$: (a) Re=10 (b) Re=100 (c) Re=300 (d) Re=500

influencing the overall thermal behavior and heat transfer performance. Similar qualitative behavior is also observed under constant wall temperature conditions

At Re = 10 (Figure 3.16a), the flow is fully laminar, and the temperature distribution is mainly governed by conduction, resulting in smooth and stratified contours. With increasing Reynolds number (Figure 3.16c, d), convective transport becomes progressively more significant, leading to a noticeable thinning of the thermal boundary layer and a more uniform temperature field within the channel. Beyond Re=300 (Figure 3.16c, d), the presence of recirculation zones enhances fluid mixing, which further promotes heat transfer and reduces temperature gradients near the wall. This overall trend highlights the transition from conduction-dominated to convection-dominated heat transfer as the flow inertia increases.

3.2 Turbulent regime

The following section presents the qualitative results obtained for the turbulent flow regime. This part of the analysis directly follows the laminar case and aims to highlight the main differences in flow behavior and thermal response when turbulence develops within the corrugated geometries.

As already introduced in chapter 2.4, to validate the turbulence model, the near-wall mesh was designed so that the first cell of the boundary layer satisfies $y^+ < 1$. Figure 3.17 shows the y^+ local distribution in the most corrugated configuration.

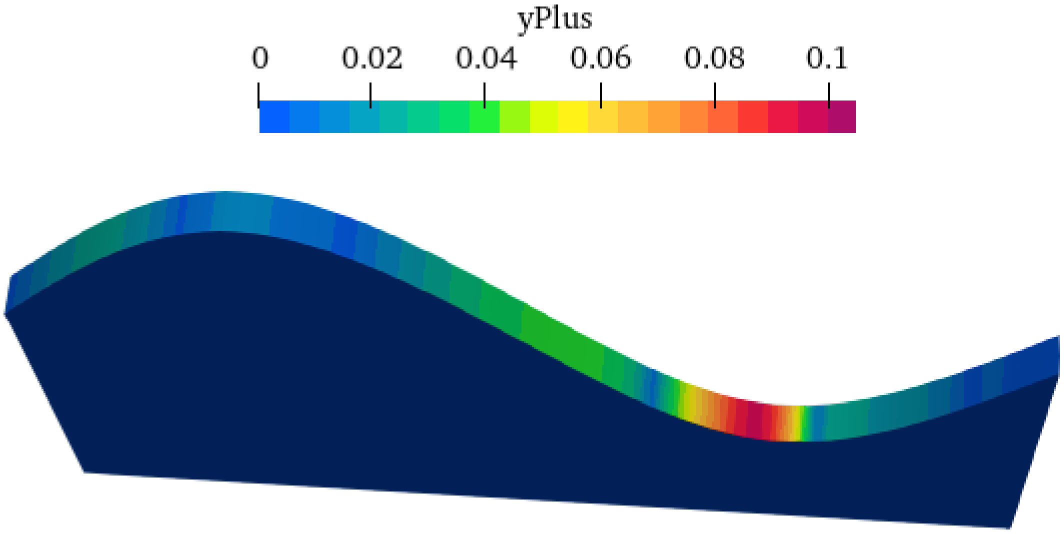

Figure 3.17: y^+ verification for Re=20000, $\alpha = 2.5, S = 0.5\ mm$

The analysis focuses on the most corrugated configurations, corresponding to α = 2.5 and α = 1.5, with corrugation amplitudes S = 0.13, 0.235, and 0.5 mm. These cases were selected because they exhibit the strongest influence of the wall undulations on the flow structures and heat transfer mechanisms, allowing a clear comparison between laminar and turbulent regimes. The selected Reynolds numbers for this analysis are 5000, 10000, 20000.

Regarding the thermal analysis, only the isothermal wall condition (imposed wall temperature) was considered. This choice was made primarily to simplify the post-processing phase and ensure a consistent comparison among configurations. Moreover, as already discussed in the previous sections, the overall trend of Nusselt number enhancement with increasing vorticity remains similar for both imposed temperature and imposed heat flux boundary conditions, making the isothermal case sufficiently representative for the purposes of this study.

3.2.1 Hydraulic results

This section analyzes the qualitative hydraulic results for all the configurations. The aim is to illustrate how the increase in wall corrugation influences the flow structure and promotes the formation of vortical motions within the channel. Initially, the visualization is performed using the surface line integral convolution (LIC) of the velocity vector field (U), which provides an intuitive representation of the local flow direction and the presence of vortical structures along the corrugated walls. This method allows highlighting the transition from predominantly aligned flow regions to more complex recirculating zones induced by the wall undulations. Through Figure 3.18 it becomes possible to clearly identify how periodic geometry enhances the mixing and disrupts the near-wall flow, revealing the mechanisms responsible for the increased vorticity and, consequently, for the improvement in heat transfer performance observed in the turbulent regime.

From the LIC visualization, it is evident that the only configuration in which no significant vortical structures are present is the least corrugated one, corresponding to $\alpha = 1.5$ and $S = 0.13$ mm. In this case, the flow remains almost completely attached to the wall, and the velocity field follows the surface profile smoothly, without the formation of recirculation zones or strong shear layers. The fluid motion is therefore mainly unidirectional, resembling the behavior typically observed in the laminar regime.

However, as soon as the wavelength is reduced, the situation changes noticeably: even for the configuration with $\alpha = 1.5$ and $S = 0.235$ mm, distinct recirculation regions begin to appear near the troughs, marking the onset of vortical motion. These structures originate as the local curvature of the wall becomes sufficient to cause flow separation, creating enclosed zones where the fluid rotates before reattaching downstream.

As the corrugation becomes more pronounced, the flow field evolves into a far more complex pattern. The number and intensity of the vortices increase, and they begin to occupy a larger fraction of the channel cross-section (Figure 3.18c, f). In the most corrugated geometry (Figure 3.18c), multiple vortices coexist within each period leading to a flow field characterized by strong mixing and high local vorticity. This proliferation of vortical structures is a clear indication of how wall modulation intensifies the fluid’s rotational dynamics, a mechanism that, as will be seen in the thermal analysis, plays a key role in enhancing heat transfer efficiency.

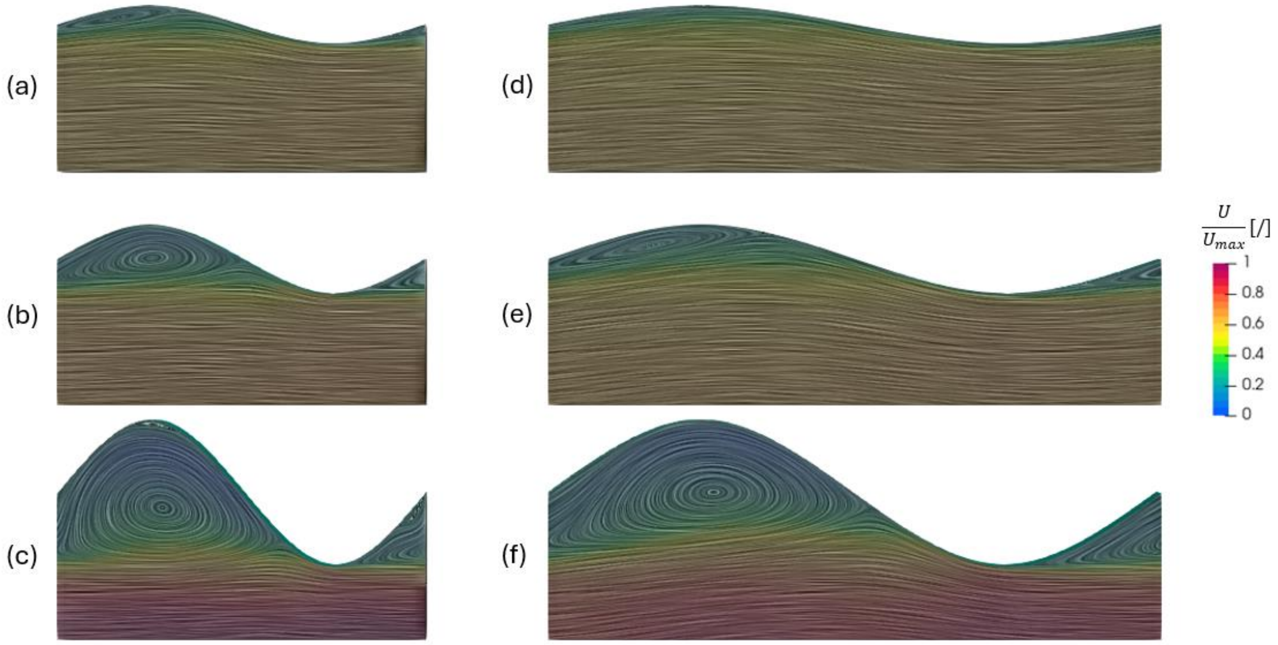

Figure 3.18: LIC of U vector for Re=5000: α=1.5: (a) S=0.13 mm, (b) S=0.235 mm, (c) S=0.5 mm. α=2.5: (d) S=0.13 mm, (e) S=0.235 mm, (f) S=0.5 mm

As the corrugation amplitude increases, a clear intensification of the velocity gradients is observed. The near-wall regions exhibit higher velocity peaks, while the low-speed zones within the troughs become more pronounced and spatially extended. This behavior indicates that the flow undergoes stronger acceleration and deceleration phases as it adjusts to the wavy surface.

In the more corrugated cases (Figure 3.19c, f), significant nonzero velocity magnitudes are visible even inside the recirculation regions. The presence of finite velocity values in these areas confirms that the flow is not stagnant but involves vortical motion with measurable tangential velocity components. These localized swirling structures enhance the local vorticity, as the velocity changes rapidly both in magnitude and direction. The progressive growth of high-velocity and recirculating regions with increasing corrugation highlights the intensification of mixing and shear effects that underline the improved heat transfer performance in the turbulent regime.

As shown in Figure 3.20a, d, for S = 0.13 mm the transverse motion is weak and confined, with very low $|u_y|$ values. As the corrugation increases, the peaks of the vertical velocity component| become stronger, especially near the walls. The enhanced wall curvature produces sharper shear layers and well-defined recirculation cells within the troughs, causing high-$|u_y|$ regions to expand and shift closer to the surface. The amplification of near-wall $|u_y|$ clearly indicates stronger vortical activity and increased cross-stream mixing.

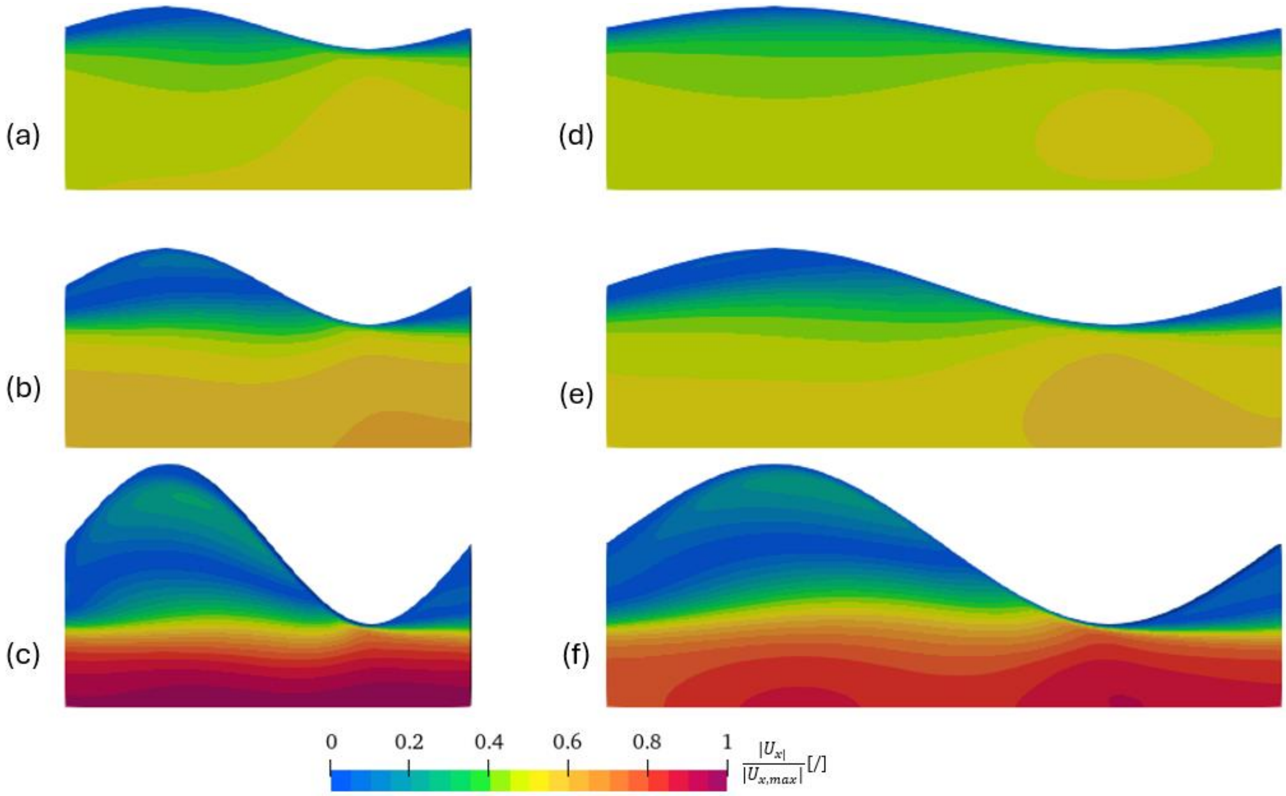

Figure 3.19: normalized velocity along x for Re=5000: α=1.5: (a) S=0.13 mm, (b) S=0.235 mm, (c) S=0.5 mm. α=2.5: (d) S=0.13 mm, (e) S=0.235 mm, (f) S=0.5 mm

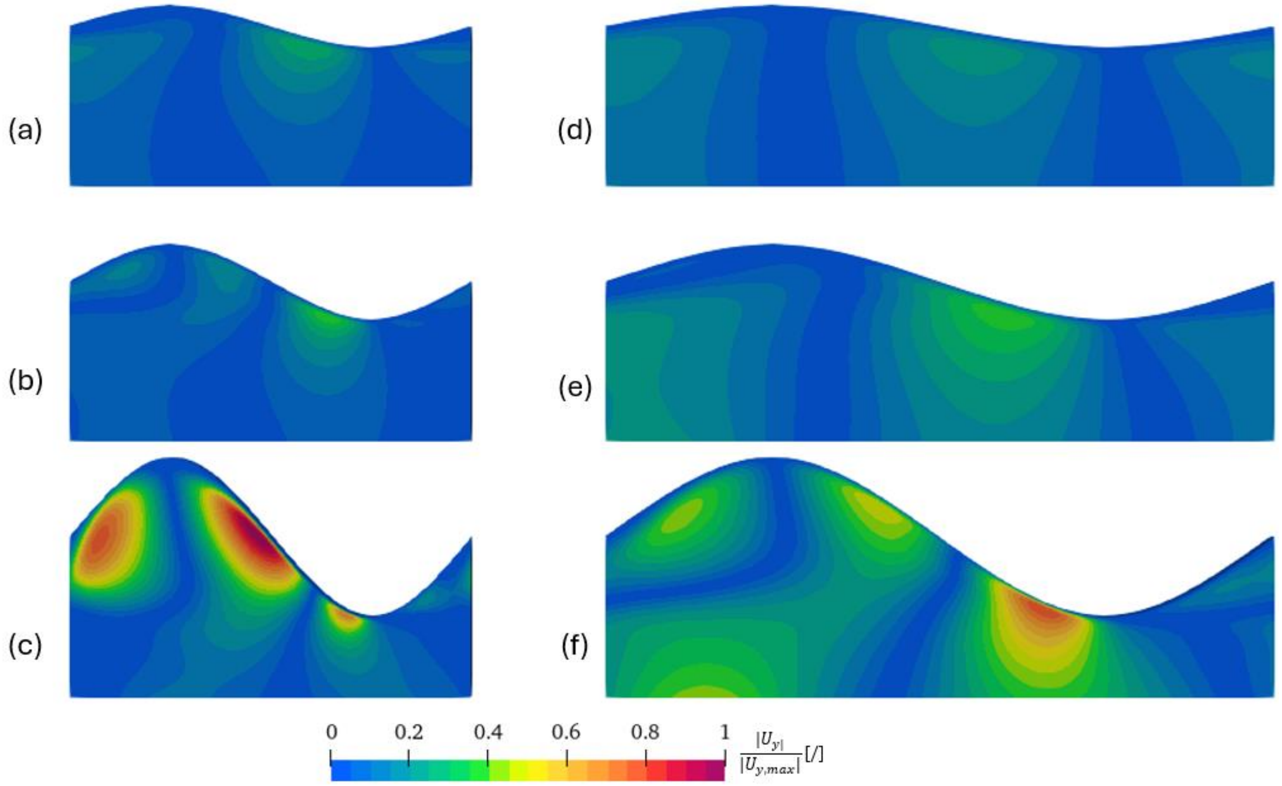

Figure 3.20: normalized velocity along y for Re=5000: α=1.5: (a) S=0.13 mm, (b) S=0.235 mm, (c) S=0.5 mm. α=2.5: (d) S=0.13 mm, (e) S=0.235 mm, (f) S=0.5 mm

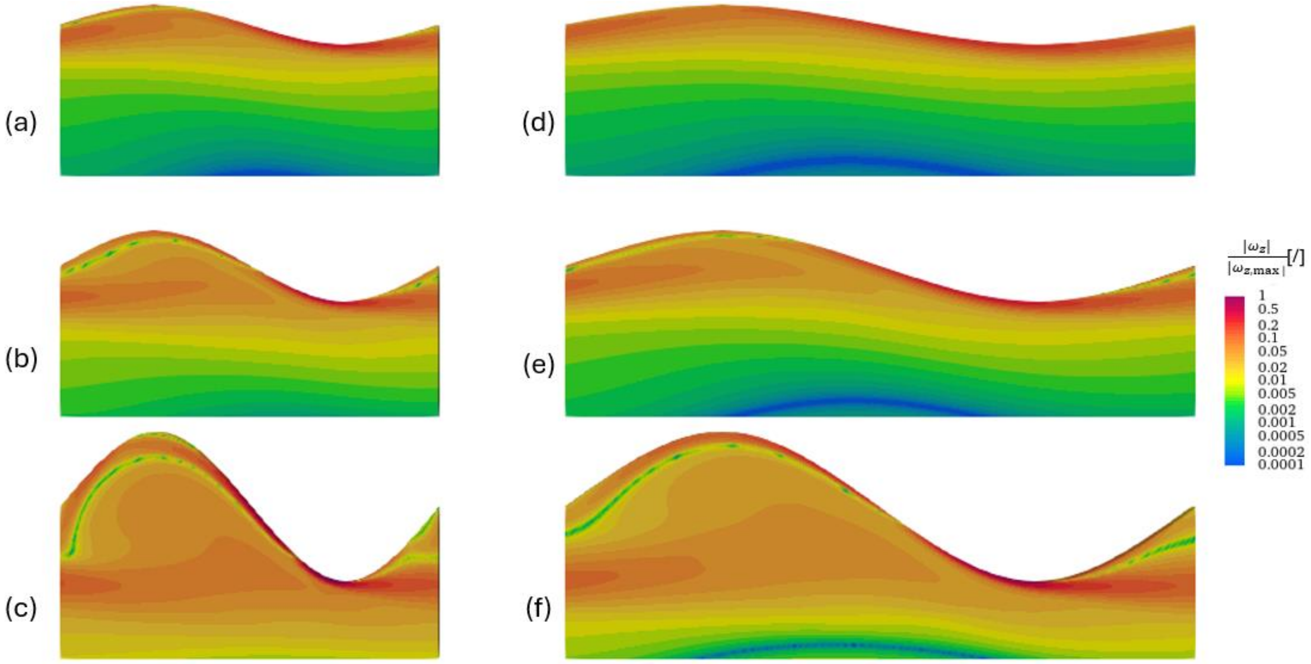

Figure 3.21: normalized vorticity along z for Re=5000: α=1.5: (a) S=0.13 mm, (b) S=0.235 mm, (c) S=0.5 mm. α=2.5: (d) S=0.13 mm, (e) S=0.235 mm, (f) S=0.5 mm

What has been shown before is now summed with the qualitative results of vorticity along z in Figure 3.21.

It is evident that as the corrugation increases, the region characterized by high vorticity (red shades) progressively expands, covering a larger portion of the flow domain. For S = 0.13 mm, the strong vorticity remains confined near the wall, where shear stress is highest, while the core of the channel remains mostly unaffected

In the most corrugated configuration (S = 0.5 mm), the vorticity distribution becomes much broader, with elevated vorticity values not only near the wall but also in the central part of the troughs. This indicates that the entire flow field is more dynamically active, with vortical structures penetrating further into the channel. Such behavior enhances the mixing of fluid particles and promotes stronger momentum and thermal exchange between the wall and the core region. As will be discussed in the next section, this intensified mixing directly contributes to the improvement of the heat transfer performance observed for highly corrugated geometries.

Following the comparison between different geometries, is important to show how the fluid changes its behavior when the onset of turbulence increases. To do so, Figure 3.22 shows how vorticity develops and increases its magnitude when passing from Reynolds equal to 5000 to 20000.

At first glance the vorticity distribution looks qualitatively similar, because the strongest values sit in thin near-wall layers and around separation, which saturate the color scale. However, the volume-averaged vorticity increases with Re, as will be shown in the quantitative discussion of the results. This trend follows what is expected: higher Re thins the viscous layer and strengthens the shear in the separation shear-layer, so $|\omega_z| \sim U/\delta$ grows and the near-wall contribution weights more in the domain average. Recirculation cells remain in the same locations but become more energetic, with larger nonzero velocities inside the cavities. Consistently, it is expected that Nusselt number will rise with Re since the thermal boundary layer is thinner and the turbulent diffusivity is higher, enhancing wall-normal mixing even if the mean $|\omega_z|$ shading appears comparable.

In short, the maps show similar topology, while integral metric reveal the monotonic growth of rotational intensity that underpins the observed heat transfer increase.

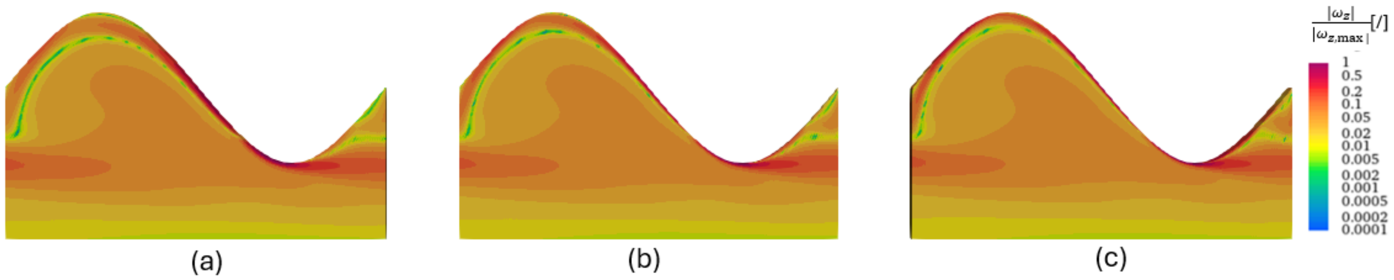

Figure 3.22: normalized vorticity distribution for α=2.5, S=0.5 mm: (a) Re=5000, (b) Re=10000, (c) Re=20000

3.2.2 Thermal results

As discussed before, results for turbulent regime are shown only for the isothermal wall temperature boundary condition. Dimensionless temperature θ is used to display the results, as in section regarding laminar results.

Figure 3.23 shows the dimensionless temperature θ for Re = 5000 under isothermal walls. The left column refers to α = 1.5, the right to α = 2.5; rows (a, c) and (d, f) correspond to S = 0.13, 0.235, and 0.5 mm.

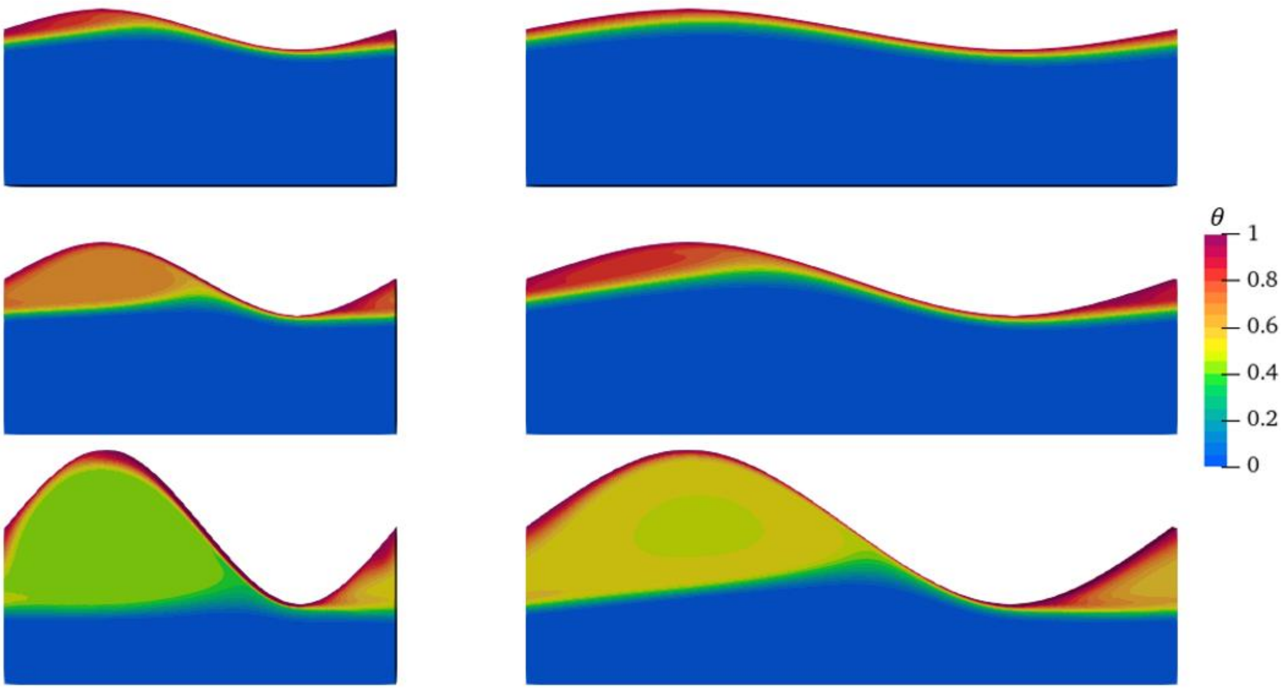

Figure 3.23: dimensionless temperature distribution for Re=5000: α=1.5: (a) S=0.13 mm, (b) S=0.235 mm, (c) S=0.5 mm. α=2.5: (d) S=0.13 mm, (e) S=0.235 mm, (f) S=0.5 mm

For α = 1.5 with S = 0.13 mm (Figure 3.23a), temperature is mostly layered: a thin hot band near the wall and a cold blue core. With S = 0.235 mm (Figure 3.23b), the isotherms bend over the troughs, and the warm layer thickens slightly. At S = 0.5 mm (Figure 3.23c), a clear warm pocket forms inside the cavity and the hot layer near reattachment becomes thinner; this is total evidence of stronger mixing.

The α = 2.5 cases show the same trend but stronger. Even at S = 0.13 mm (Figure 3.23d) the warm region is broader than for α = 1.5. At S = 0.235 mm (Figure 3.23e) a distinct warm patch appears downstream of the trough. For S = 0.5 mm (Figure 3.23f) a large warm area fills much of the section and the isotherms are strongly distorted. In short: more corrugation pushes warm fluid into the core and thins the near-wall thermal layer, which is consistent with enhanced mixing and higher heat transfer.

Similarly to what has been shown for the laminar results, the most corrugated geometry will be displayed comparing the thermal behavior when increasing the Reynolds number, to understand how the temperature distribution changes (Figure 3.24).

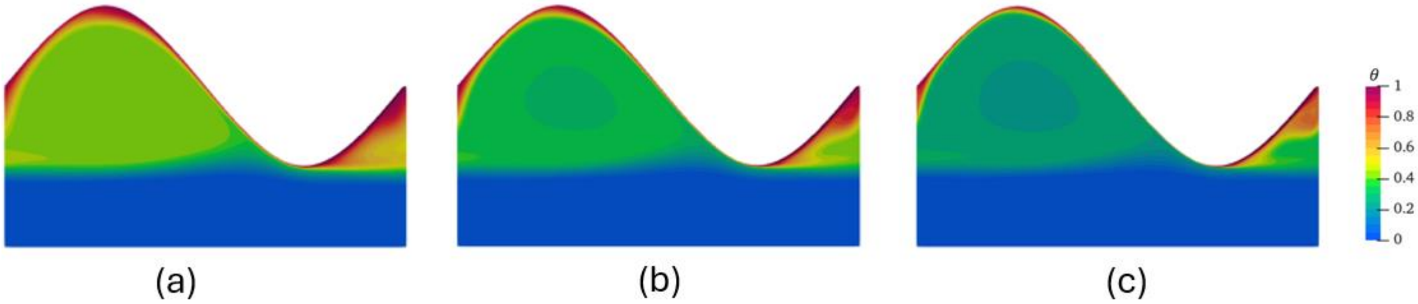

Figure 3.24: dimensionless temperature distribution for α=2.5, S=0.5 mm: (a) Re=5000, (b) Re=10000, (c) Re=20000

The trends align with the vorticity evidence discussed earlier. As Re rises, the near-wall thermal layer becomes thinner and the red band intensifies, indicating steeper wall-normal temperature gradients and therefore higher local heat flux. Isotherms bend more strongly over separation and reattachment, and the warm pocket inside the cavity becomes tighter and closer to the wall, while the channel core remains comparatively colder at the same axial location. Overall, higher Re produces sharper thermal gradients and more distorted isotherms, exactly the qualitative signature of an increasing Nusselt number noted in the quantitative results, with the accompanying cost of higher frictional losses (chapter 4).

4 Discussion

In this chapter, a quantitative discussion of the hydraulic and thermal performance of the sinusoidal channels is presented. Building on the qualitative observations introduced in the previous section, the analysis focuses on the relationship between the normalized friction factor and Nusselt number with the normalized mean vorticity within the channel. This approach aims to show how the flow structures and associated velocity gradients influence both pressure losses and heat transfer enhancement across different geometrical configurations and Reynolds numbers.

The friction factor is evaluated according to the Darcy-Weisbach correlation:

$$f = \frac{\Delta p}{L} \cdot \frac{D_h}{2\rho u_m^2} \tag{4.1}$$

where $\frac{\Delta p}{L}$ is the pressure gradient, automatically computed in OpenFOAM. To assess the effect of wall corrugation, this quantity is normalized by the friction factor of the reference parallel-plate channel, evaluated as:

$$f_0 = \frac{64}{Re}\ for\ the\ laminar\ regime\ (Re < 2300) \tag{4.2}$$

$$f_0{}^{1} = 0.3164 \cdot Re^{-0.25} for\ turbulent\ regime\ (3000 < Re < 10^5) \tag{4.3}$$

Local vorticity is defined as:

$$\omega = \nabla \times U \tag{4.4}$$

With $U = (u_x, u_y, u_z)$.

Since the simulations are performed on a two-dimensional domain, with a single cell in the z-direction, only the z-component of vorticity is relevant:

$$\omega_z = \frac{\partial u_y}{\partial x} - \frac{\partial u_x}{\partial y} \tag{4.5}$$

Vorticity along z is then averaged on all the domain using a *surface average* function object on OpenFOAM:

$$\overline{|\omega_z|} = \frac{\int_A |\omega_z| dA}{\int_A dA} \tag{4.6}$$

A is the surface over which the mean is averaged and *dA* is the infinitesimal local area.

To investigate possible correlations between vorticity and the global performance parameters (Nusselt number and friction factor), the mean vorticity was normalized using two different approaches.

In the first normalization, the mean spanwise vorticity of the studied corrugated channel, $|\overline{\omega_z}|$ was divided by the corresponding value obtained in the flat channel at the same Reynolds number:

$$\frac{|\overline{\omega_z}|}{|\overline{\omega_{z,0}}|} = \frac{|\overline{\omega_z}|(Re_x)}{|\overline{\omega_z}|(Re_x, parallel\ flat\ planes)} \tag{4.8}$$

This ratio highlights how much the vorticity field is intensified with respect to the reference case of parallel flat plates, thus allowing a direct assessment of the flow structure enhancement induced by the surface corrugation.

---

[1] Blasius correlation for friction factor in turbulent regime

The second normalization, which will later be used to correlate the Nusselt number in the laminar regime, quantifies the relative increase of vorticity with respect to the so-called "laminar cutoff," corresponding to Re = 10. In this case, the mean vorticity of each configuration is compared to its value at Re = 10, to evaluate the effective growth of vorticity as the flow becomes more energetic and mixing increases:

$$\frac{|\overline{\omega_z}|}{|\overline{\omega_{z,0}}|} = \frac{|\overline{\omega_z}|(Re_x)}{|\overline{\omega_z}|(Re = 10)} \tag{4.8}$$

This approach was adopted because the hydraulic diameter used for normalization (see Chapter 2.3) was defined to penalize the corrugated geometries. Consequently, when the Nusselt number is computed in its raw form, the smoother channels tend to appear more efficient at low Reynolds numbers, leading to a non-monotonic trend with increasing corrugation. Such behavior would make it difficult to establish a clear correlation between Nusselt number and mean vorticity. By normalizing vorticity with respect to the laminar reference case, the analysis compensates for this geometric bias and enables a more consistent, monotonic comparison between vorticity growth and heat transfer enhancement across the different geometries.

Nusselt number is calculated as:

$$Nu = \frac{hD_h}{k} \tag{4.9}$$

where h [W/(m²·K)] is the convective heat transfer coefficient and k [W/(m·K)] is the thermal conductivity of the fluid. The evaluation of h depends on the imposed thermal boundary condition:

- Imposed wall temperature: $h = \frac{q''}{\Delta T_{log}}$ with $\Delta T_{log} = \frac{T_{out} - T_{in}}{\log(\frac{T_s - T_{in}}{T_s - T_{out}})}$
- Imposed heat flux at the wall: $h = \frac{q''}{\Delta T_{sb}}$ with $\Delta T_{sb} = T_s - T_{bulk}$

Under the *T imposed* condition, the system behaves analogously to a conventional heat exchanger, and the Nusselt number can be directly obtained through the logarithmic mean temperature difference.

In contrast, for the *imposed heat flux* case, the difference between surface temperature and bulk temperature varies along the corrugated walls. Therefore, the heat transfer coefficient must be computed at several streamwise sections, and a spatially averaged value is used to evaluate the mean Nusselt number. Bulk temperature is evaluated on each section as:

$$T_{bulk} = \frac{\int_A \rho u T dA}{\int_A \rho u dA} \tag{4.10}$$

Similarly, the Nusselt number was normalized according to the flow regime to enable a consistent comparison with the vorticity-based indicators.

In the laminar regime, the normalized Nusselt number was expressed as its relative increase with respect to the value at Re = 10, following the same approach adopted for the vorticity normalization:

$$\frac{Nu}{Nu_0} = \frac{Nu(Re_x)}{Nu(Re = 10)} \tag{4.11}$$

This formulation highlights the actual growth of convective performance as the flow develops and strengthens, allowing a direct comparison between the enhancement of vorticity and the corresponding increase in heat transfer.

In the turbulent regime, instead, normalization was performed using the classical ratio Nu/Nu_0, where Nu_0 represents the Nusselt number for the limiting case of parallel flat plates:

$$\frac{Nu}{Nu_0} = \frac{Nu(Re_x)}{Nu(Re_x, parallel\, flat\, plates)} \tag{4.12}$$

The reference value Nu_0 was computed using the Gnielinski correlation, which provides an accurate estimate of the Nusselt number for fully developed turbulent flow in smooth channels:

$$Nu_0 = \frac{(f/8)(Re - 1000)Pr}{1 + 12.7(f/8)^{0.5}(Pr^{0.66} - 1)} \tag{4.13}$$

This choice is appropriate because, in turbulent conditions, the differences among the various corrugated configurations become more pronounced, and the ratio Nu/Nu_0 exhibits a clear, monotonic trend that can be effectively correlated with the evolution of mean vorticity.

4.1 Vorticity analysis

The first part focuses on the laminar regime, where vorticity mainly arises from shear and recirculation induced by channel geometry. The second part extends the discussion to turbulent conditions, examining how the onset of turbulence and increase in Reynolds amplify the vorticity distribution through the domain.

4.1.1 Laminar Regime

Globally, an increase in both the corrugation amplitude and the Reynolds number leads to a progressive rise in the mean vorticity within the domain (Figure 4.1).

This trend reflects the stronger velocity gradients and enhanced flow curvature induced by the wall geometry and the higher inertial effects associated with larger Reynolds numbers. At low corrugation levels, the flow remains relatively smooth and aligned with the main direction, resulting in limited rotational motion. As the corrugation amplitude increases, the alternating wall curvature promotes local flow acceleration and deceleration, which amplifies shear and generates stronger vortical regions near the surface.

Similarly, at higher Reynolds numbers, the inertia of the fluid accentuates these mechanisms, leading to more pronounced flow separation and larger recirculating zones. As a result, the spatially averaged vorticity over the entire domain systematically increases; the peak values are reached in the configurations with higher S.

The trend observed for mean vorticity is further confirmed by the analysis of the maximum vorticity values within the domain, as shown in Figure 4.2. For each configuration, the maximum vorticity increases progressively with the Reynolds number, following a behavior like that of the spatially averaged vorticity. This growth reflects the combined effect of the higher inertial forces and the intensified velocity gradients induced by the wall corrugation. As

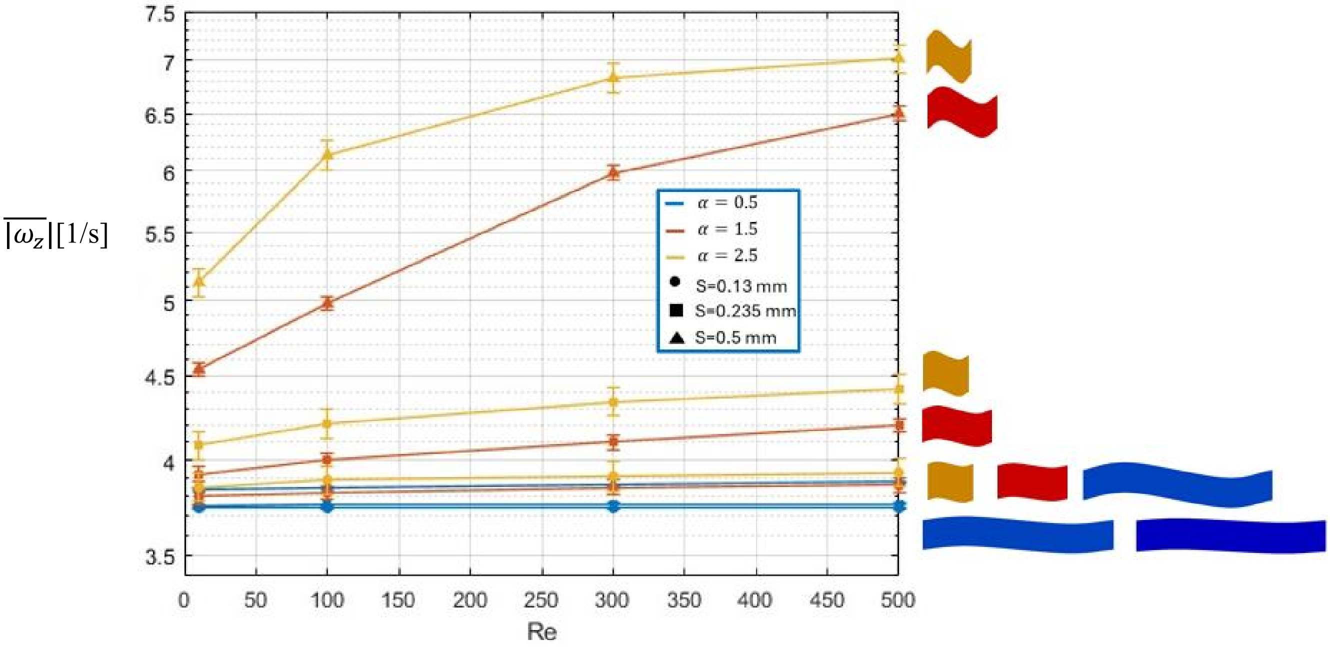

Figure 4.1: average vorticity trend increasing Reynolds for different corrugation degrees

the corrugation amplitude increases, the flow experiences stronger curvature and sharper accelerations near the peaks and troughs of the sinusoidal surfaces, which locally enhance the rotational motion. Consequently, configurations characterized by larger α and higher Reynolds numbers exhibit more intense vortex cores and stronger shear layers. However, while the mean vorticity provides a global measure of flow rotation, the maximum values reveal the presence of localized regions of intense vortical activity. As shown in Figure 4.3, the normalized mean

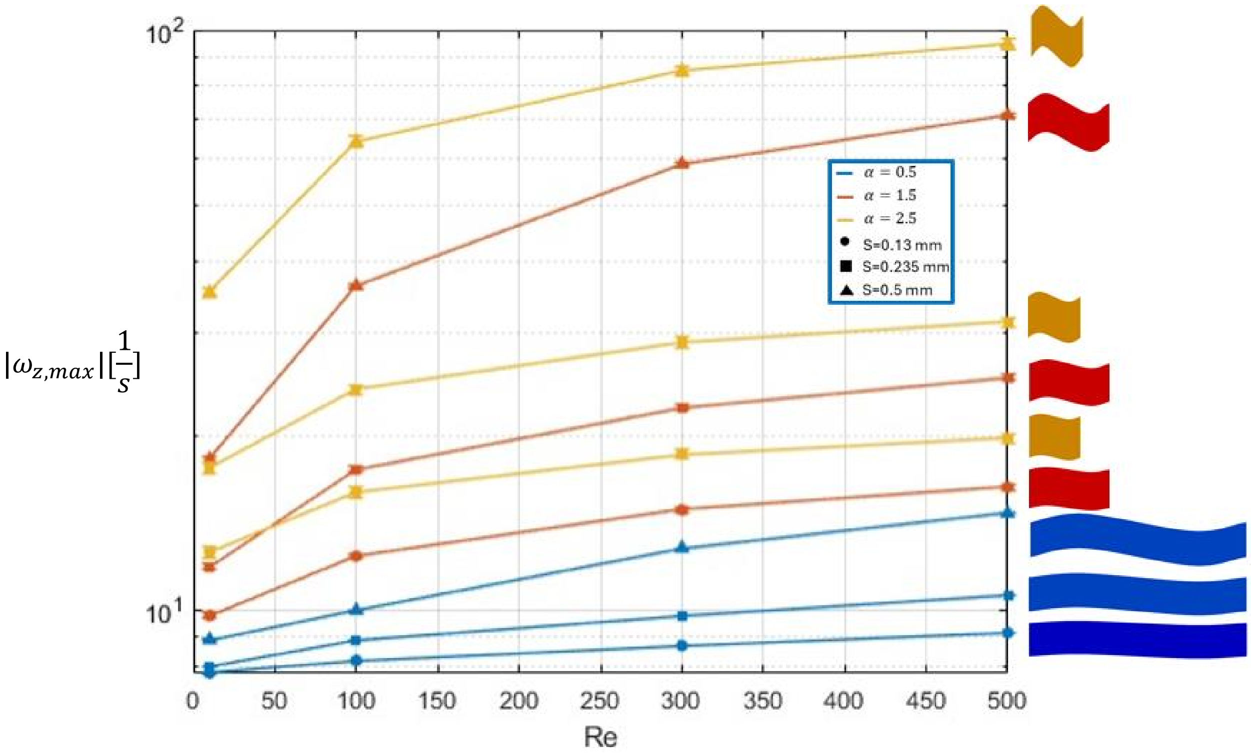

Figure 4.2: maximum vorticity for each configuration increasing Reynolds

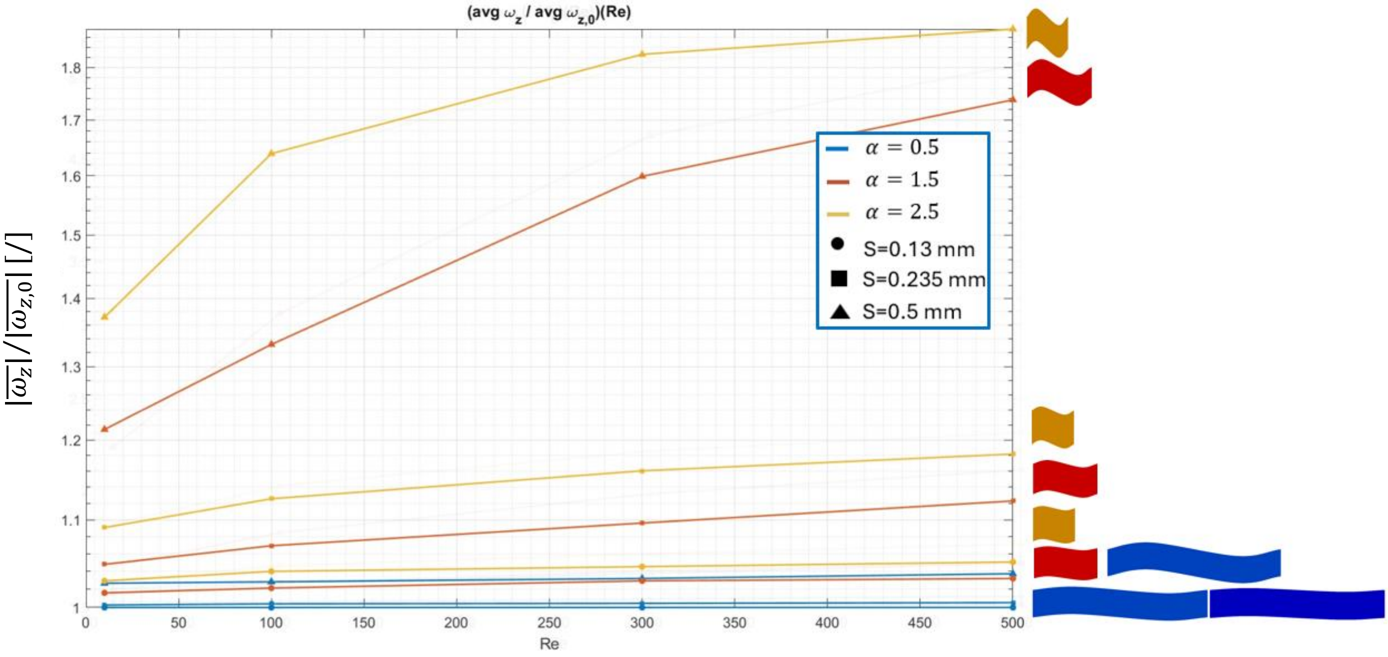

Figure 4.3: normalized average vorticity in function of Reynolds for all configurations

vorticity increases with the Reynolds number and exhibits a trend that closely follows the previous ones.

This correlation reflects the global nature of both quantities: as the corrugation enhances mixing and promotes the formation of recirculating regions, the average vorticity in the domain rises.

All different parameters show the same pattern: most corrugated geometry wins in terms of vorticity, thanks to the localized peaks that influence the average vorticity among the whole domains. Instead, less corrugated geometry tends to match the behavior of a smooth pipe.

4.1.2 Turbulent regime

Starting from the qualitative results, it is immediately evident that in turbulent flow the mean vorticity within the channel increases even more significantly than in the laminar regime. The stronger mixing and the presence of fine scale vortical structures enhance the overall rotational intensity of the flow, especially near the corrugated walls where shear layers and recirculation zones become more energetic. To better quantify this behavior, the following section shows the normalized mean vorticity in turbulent conditions, allowing a direct comparison with the laminar results and highlighting how the onset of turbulence amplifies the influence of wall corrugation on the global vorticity field.

Figure 4.4 and 4.5 shows the average vorticity and normalized average vorticity with increasing Re.

The results clearly show that the two configurations with the highest corrugation amplitude are those that most effectively promote the development of vorticity, confirming what was already observed qualitatively in Chapter 3. However, the configuration with α = 2.5 demonstrates a superior ability to enhance vorticity compared to the one with α = 1.5, even when considering a smaller corrugation amplitude (S = 0.13 mm) with a shorter wavelength.

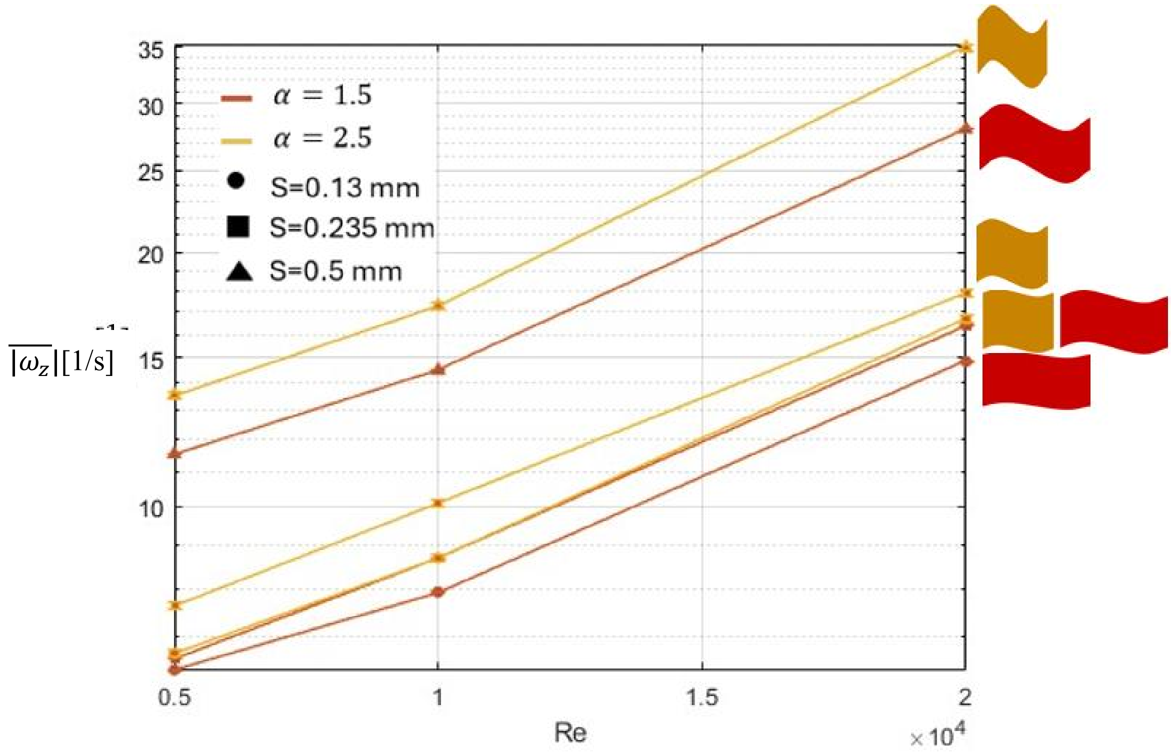

Figure 4.4: average vorticity in turbulent regime as the Reynolds increases

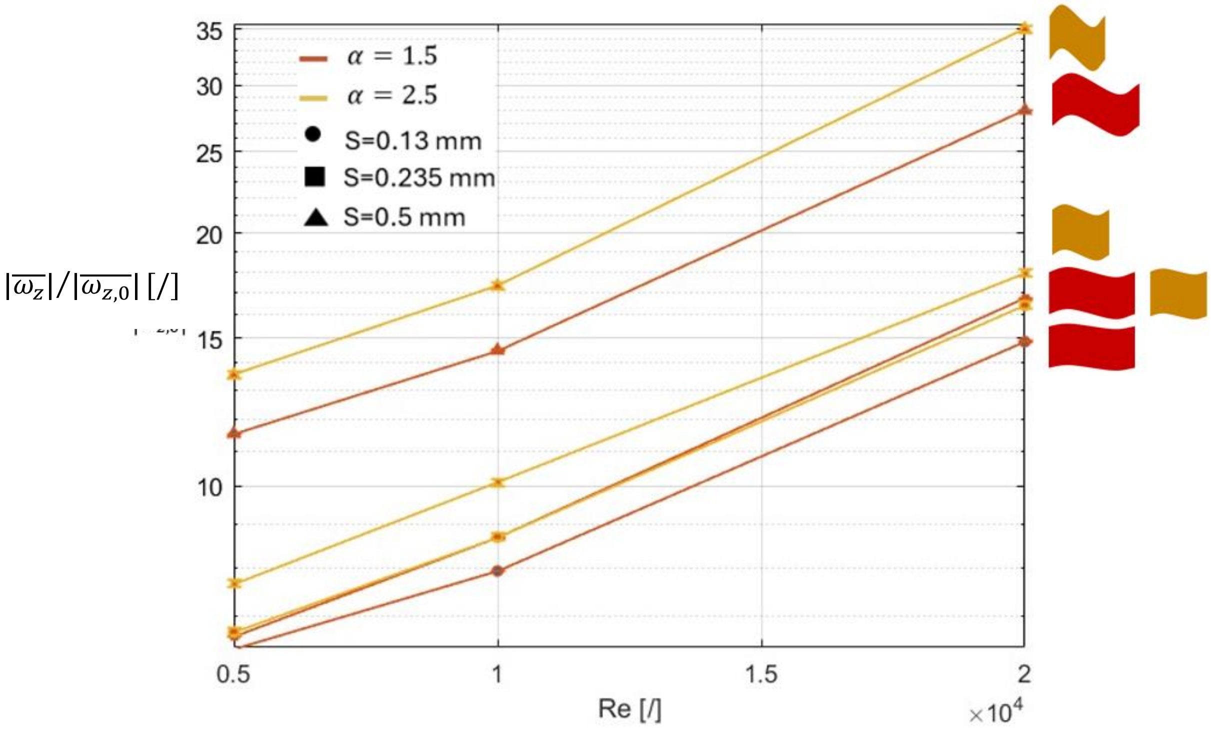

Figure 4.5: normalized average vorticity in turbulent regime as the Reynolds increases

4.2 Friction factor analysis

The analysis of the friction factor results provides insight into how the geometric characteristics of the channel and the flow conditions affect the overall pressure losses. Before discussing the normalization procedure applied to the data, it is useful to highlight that the

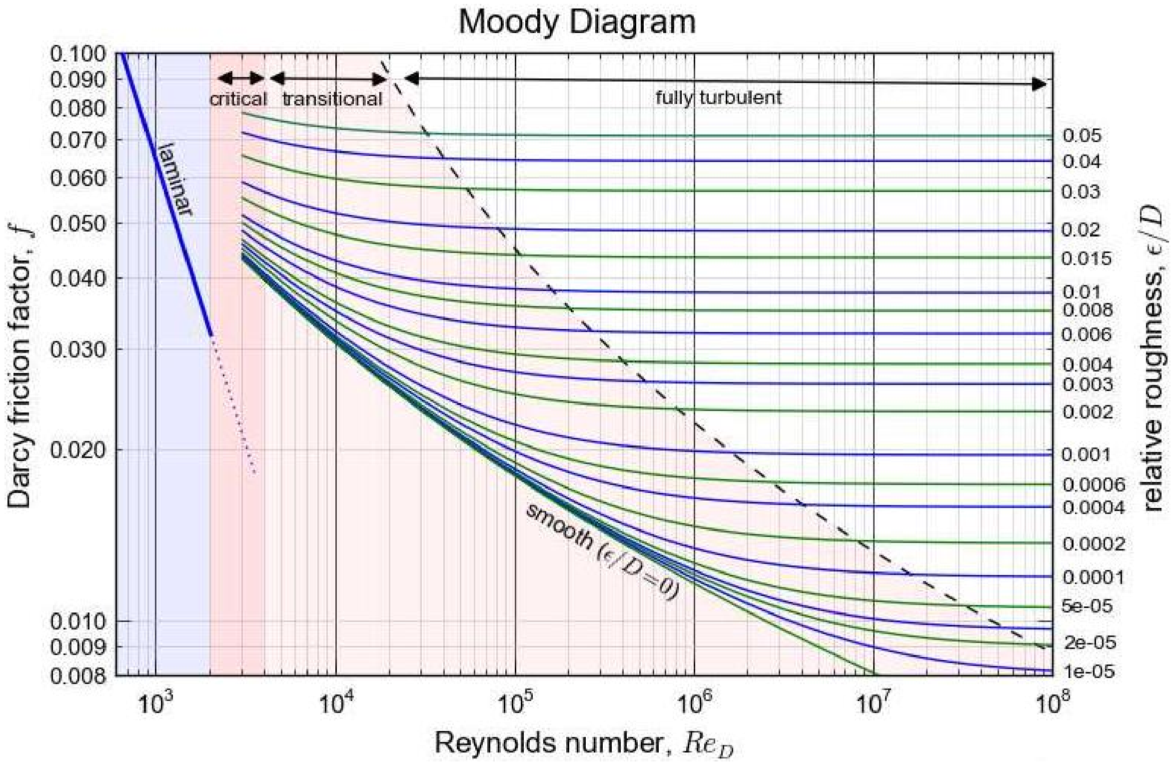

Figure 4.6: experimental moody diagram

general trend of the computed friction factor follows the behavior typically observed in the Moody diagram [16] (Figure 4.6).

In the Moody chart, the friction factor is plotted as a function of the Reynolds number, showing three distinct regions: at low Reynolds numbers, the flow is laminar and the friction factor decreases proportionally to 1/Re; as Re increases, a transition region appears where the behavior becomes less regular; finally, in the turbulent regime, the friction factor tends to level off or slightly increase, especially in the presence of surface roughness or geometrical irregularities.

The numerical results exhibit a consistent evolution with these theoretical trends, showing a gradual reduction of the friction factor as the Reynolds number increases, with deviations that can be attributed to the enhanced flow disturbances and secondary motions induced by the corrugated geometry.

Figure 4.7 shows the variation of the friction factor with the Reynolds number for the different geometric configurations analyzed. The overall behavior closely resembles the characteristic trend observed in the Moody diagram. As in the classical representation, at low Reynolds numbers the flow remains laminar, and the friction factor decreases proportionally to 1/Re. As Re increases, the curves gradually approach an asymptotic region where the slope becomes less steep.

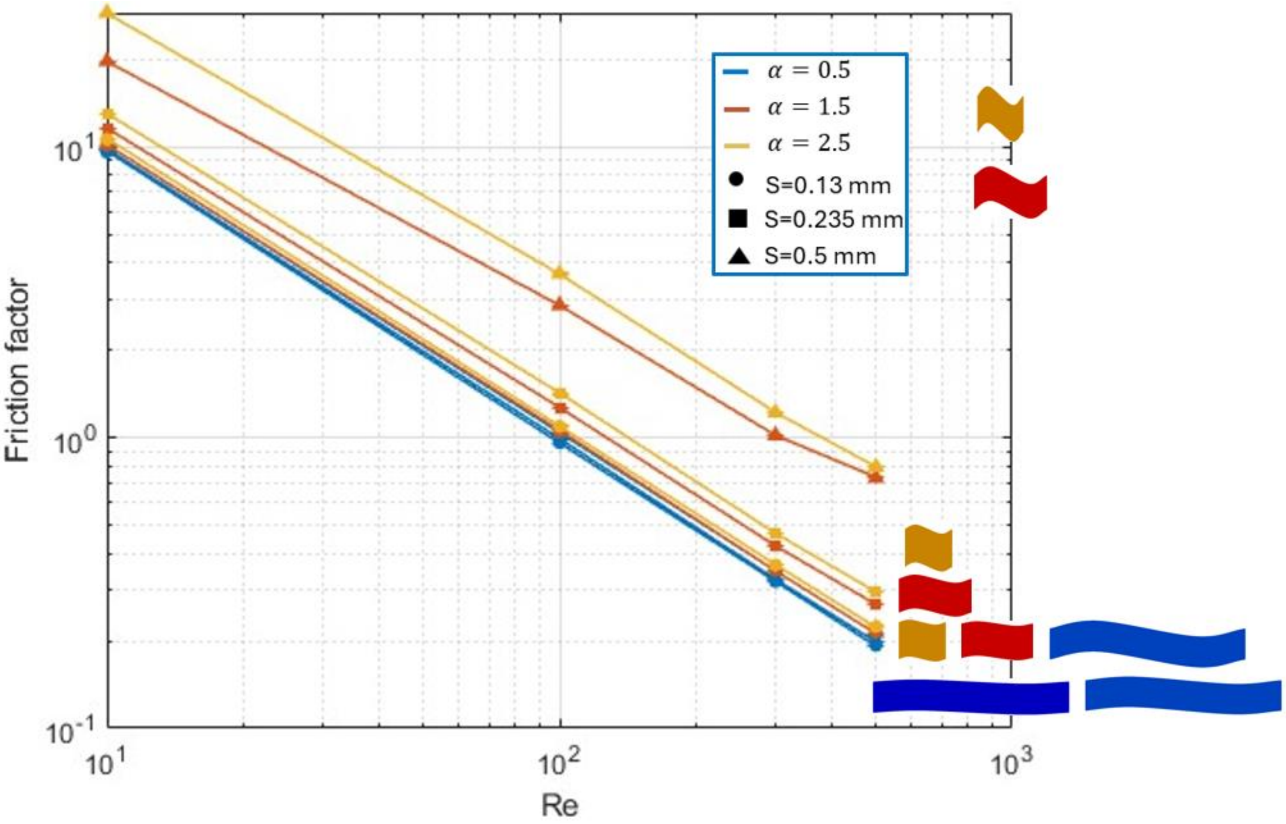

Figure 4.7 friction factor trend with increasing Reynolds number

In this context, the effect of channel corrugation plays a role analogous to surface roughness in the Moody chart: increasing the corrugation amplitude or corrugation wavenumber (α) anticipates the deviation from the laminar 1/Re trend, leading the friction factor to reach its asymptotic behavior at lower Reynolds numbers. This indicates that stronger geometric perturbations enhance flow disturbances and promote an earlier transition toward a more mixed, higher-loss regime. The configurations with larger α and smaller spacing S therefore exhibit higher friction factors and a faster approach to the asymptotic region, consistent with the behavior expected for rougher surfaces in the Moody diagram.

4.2.1 Laminar Regime

Figure 4.8 shows the trend of f/f_0 for all the simulated configurations in laminar regime:

It can be observed that friction factor tends to increase with the Reynolds number, indicating that the relative impact of wall corrugation on pressure losses becomes more significant as the flow inertia grows. In other words, while the absolute friction factor decreases with Reynolds number for all geometries, its reduction is less pronounced in the corrugated channels than in the smooth reference one. This behavior suggests that the flow disturbances and recirculation zones induced by the surface undulations intensify with increasing Reynolds number, enhancing momentum exchange and leading to higher normalized losses. The amplitude and wavelength of the corrugation further modulate this effect, with larger amplitudes and shorter wavelengths producing stronger deviations from reference behavior.

Finally, the quantitative relationship between the normalized friction factor and the normalized mean vorticity was investigated through a global fitting procedure. For each configuration and Reynolds number, the values of $(f/f_0 - 1)$ and $(\overline{|\omega_z|}/\overline{|\omega_{z,0}|} - 1)$ were extracted and combined into a single dataset. Error bars were included to account for the uncertainty associated with the pressure-drop evaluation. The resulting points were then fitted in log–log space using a power-law model with an additional offset term, expressed in the general form:

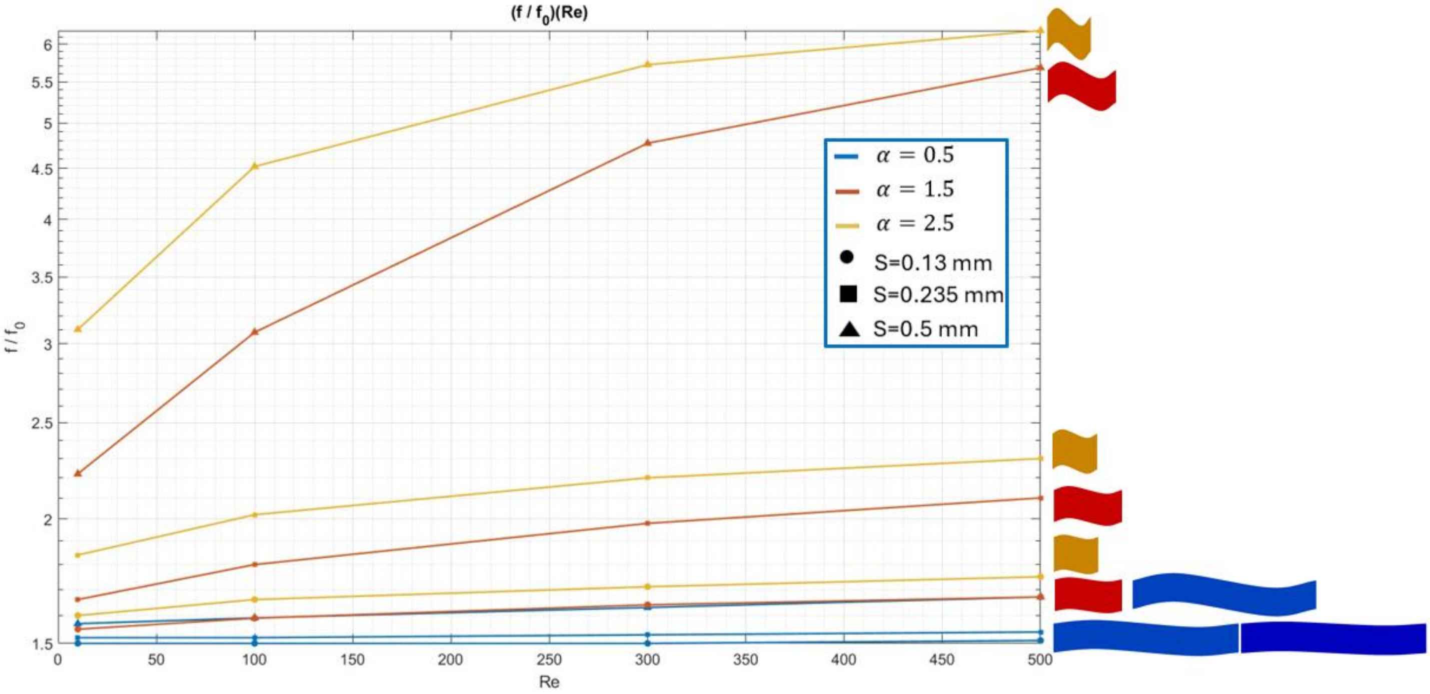

Figure 4.8: normalized friction factor in function of Reynolds for all configurations

$$\left(\frac{f}{f_0} - 1\right) = A \cdot \left(\frac{\overline{|\omega_z|}}{|\omega_{z,0}|} - 1\right)^{B} + C \tag{4.13}$$

where A, B, and C are fitting coefficients determined through nonlinear regression. The fit provides an excellent correlation ($R^2 \approx 0.98$), confirming that the normalized friction factor scales almost linearly with the normalized mean vorticity across all configurations and Reynolds numbers. This result supports the interpretation that the global vorticity field effectively captures the degree of flow disturbance and momentum exchange induced by the wall corrugation, which directly translates into increased frictional losses. The presence of a small offset term C accounts for residual effects not directly linked to vorticity, such as local flow asymmetries or secondary circulation near the walls. The obtained relation is the following:

$$\frac{f}{f_0} = 5.45 \cdot \left(\frac{\bar{\omega}z}{\bar{\omega}z0} - 1\right)^{1.17} + 1.53 \tag{4.14}$$

As shown in Figure 4.9, the fitted curve provides an excellent representation of the overall trend between the friction factor and the mean vorticity. The smooth power-law dependence captures the progressive growth of frictional losses with increasing vorticity, confirming the strong coupling between the global flow rotation and the hydraulic performance of the corrugated channels: it is possible to notice that the normalized friction factor is directly proportional to the normalized vorticity with an exponential power of 1.17. The close agreement between the data points and the fitted curve across all geometrical configurations and Reynolds numbers

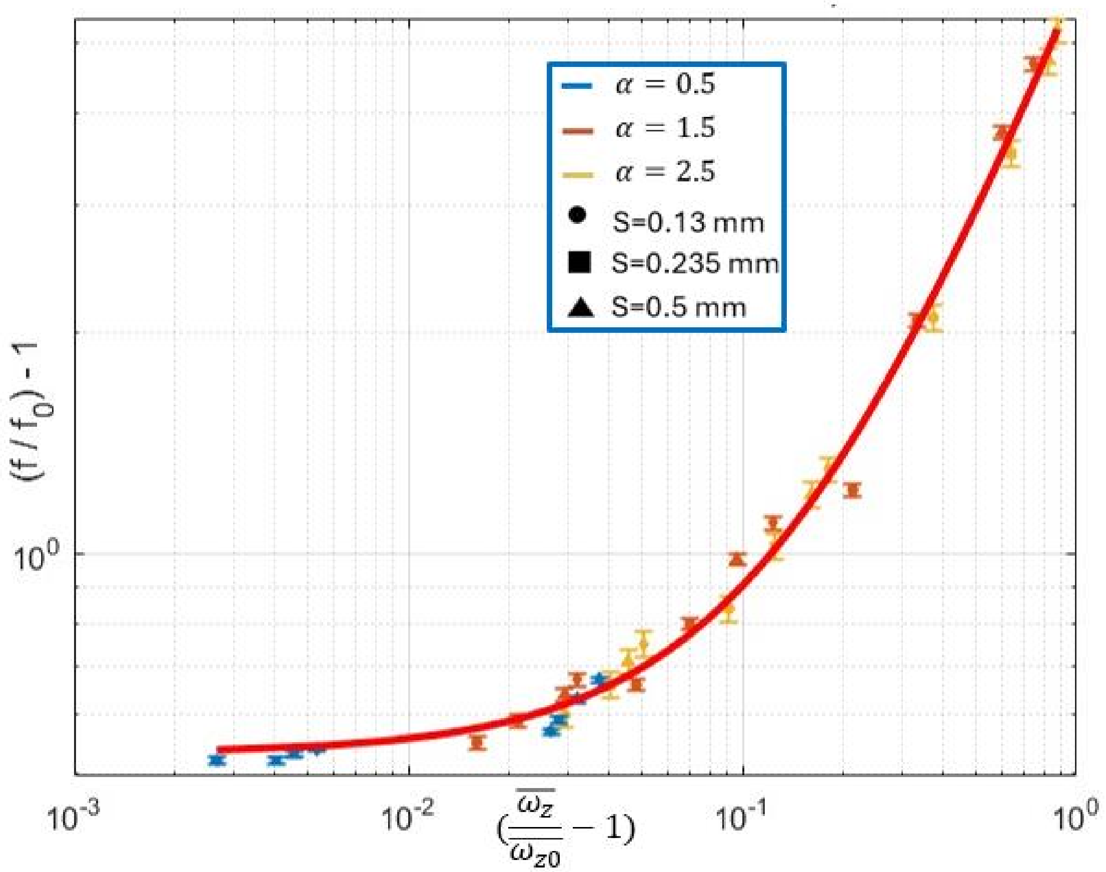

Figure 4.9: fitting curve correlation between normalized friction factor and normalized average vorticity

further supports the idea that the mean vorticity can be considered a reliable global indicator of the additional dissipation mechanisms introduced by wall corrugation.

This may be a rule of thumb for the preliminary design of corrugated and complex geometries, like TPMS.

4.2.2 Turbulent regime

In turbulent regime, the mechanisms contributing to pressure losses become significantly more complex due to the enhanced mixing, flow separation, and the formation of multiple recirculation zones within the corrugated channels. To better understand how these effects influence the overall flow resistance, this section first presents the raw friction factor data as a function of the Reynolds number for all the six configurations.

Finally, the normalized friction factor trends will be compared with the normalized vorticity results discussed in the previous paragraph, to assess the correlation between flow structure intensity and pressure losses. Figure 4.10 shows the raw friction factor trend with increasing Reynolds while Figure 4.11 shows the normalized friction factor.

As expected, the most corrugated configurations exhibit higher overall friction factors due to the stronger flow disturbances and recirculation zones induced by the geometry. Moreover, these configurations reach an asymptotic value of the friction factor earlier, meaning that beyond a certain Reynolds number, further increases in Re no longer lead to a significant reduction of friction losses. This behavior is consistent with what is shown in the Moody diagram discussed in the previous paragraph, where rough surfaces tend to approach an asymptotic limit.

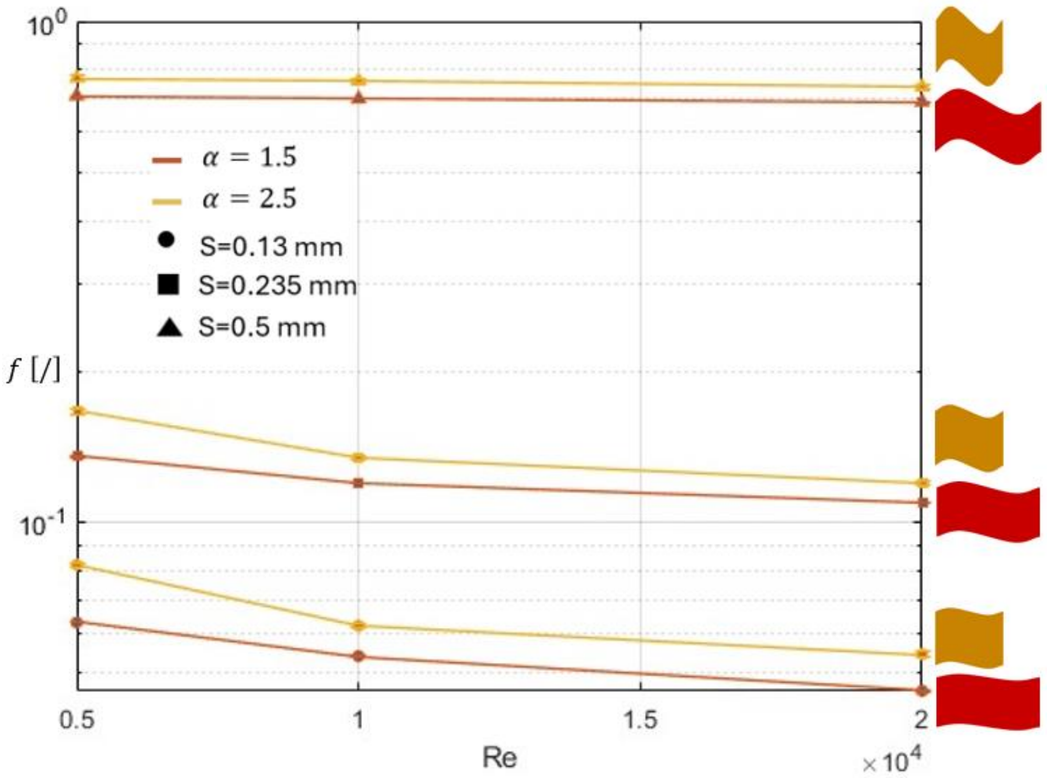

Figure 4.10: friction factor trend with increasing Reynolds in turbulence regime

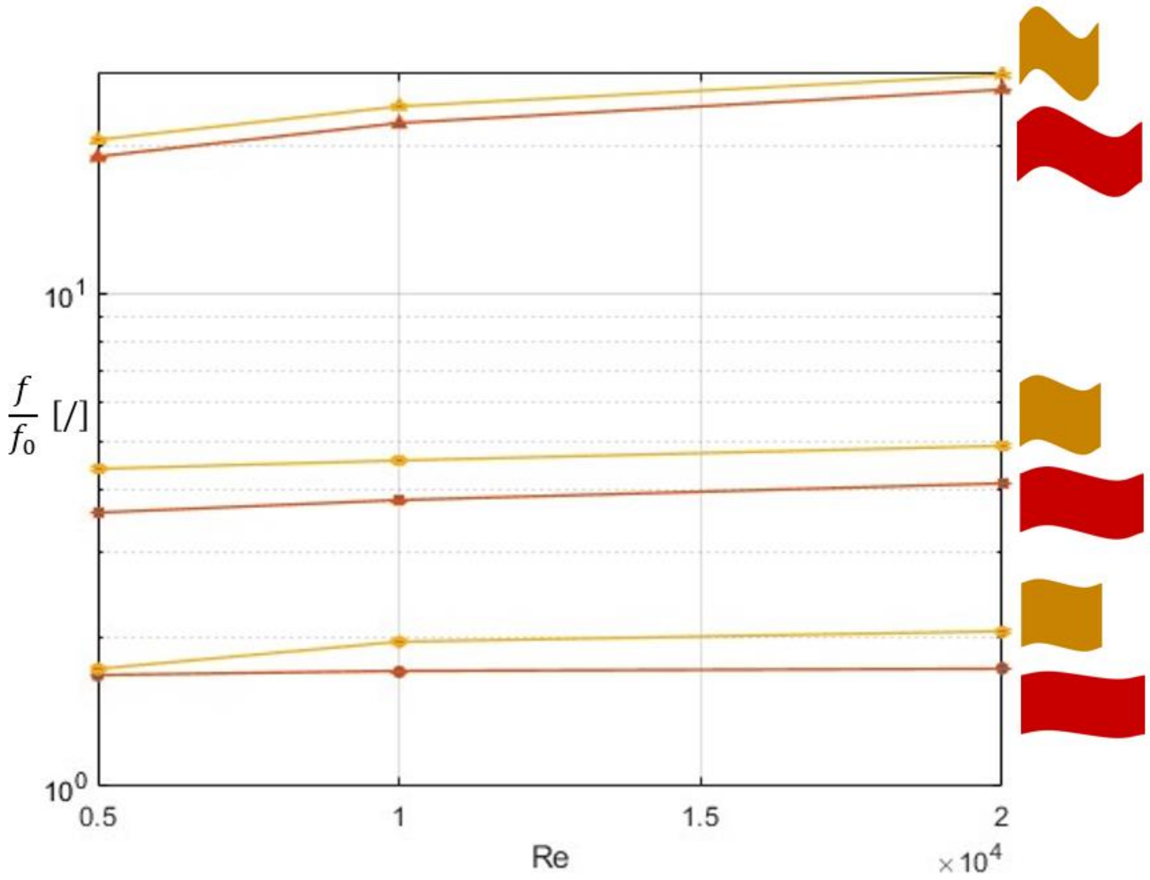

Figure 4.11: friction factor trend with increasing Reynolds in turbulence regime

Consequently, when the results are normalized, the ratio between the corrugated and parallel flat planes friction factors continues to increase with Reynolds number. This occurs because the friction factor of the corrugated cases remains nearly constant, while that of the smooth channel keeps decreasing, leading to a progressively higher normalized value. Figure 4.12 shows the fitting curve for normalized friction factor and vorticity.

As for laminar regime, to find a rule of thumb also in turbulent regime, the same global fitting procedure was displaced: unfortunately, the obtained correlation seems fails to describe the global trend of friction factor with respect to vorticity (Figure 4.12).

This result confirms the earlier observation that establishing a clear correlation between the friction factor and vorticity becomes more challenging in the turbulent regime, due to the increased complexity and variability of the flow structures.

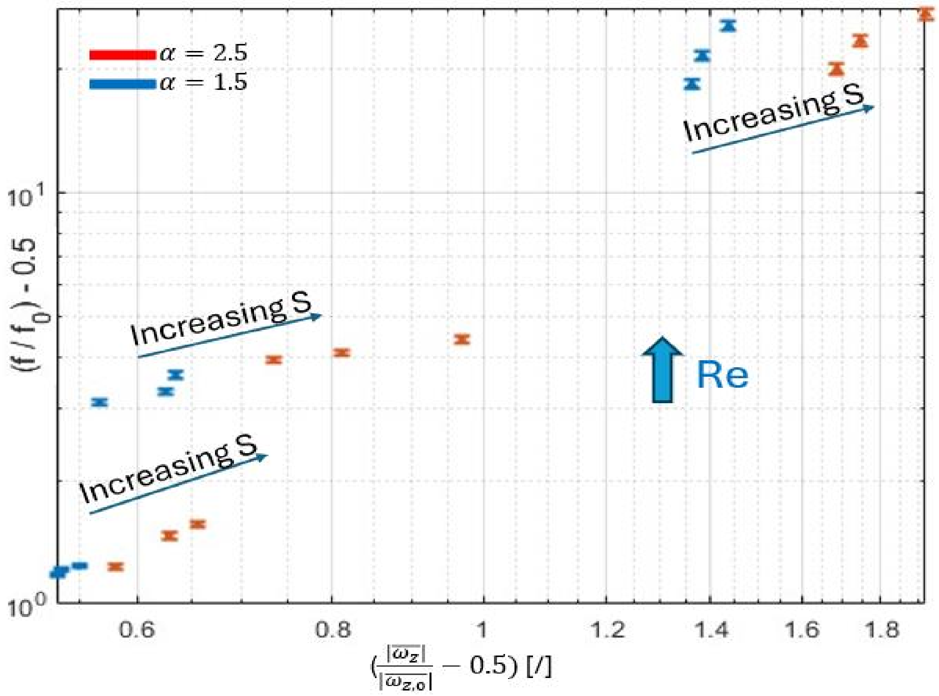

Figure 4.12: data set for normalized friction factor and vorticity for both $\alpha = 2.5, 1.5$ at Re=5000, 1000, 2000

4.3 Normalized Nusselt analysis

4.3.1 Laminar regime

From theory, it is known that for the case of parallel flat plates in 2D the Nusselt number is Nu = 7.54 [2] when a constant temperature boundary condition is imposed. In the case of constant heat flux, the corresponding value Nu is expected to be higher (Nu=8.235 for parallel flat plates), and this trend is confirmed by the present results. Since in this analysis the Nusselt numbers are normalized with respect to the laminar reference case (Re = 10), the absolute difference between the two values becomes less relevant. Therefore, to investigate the correlation with the mean vorticity, it is sufficient to present only one of the two normalized quantities, as both exhibit the same relative trend with respect to the reference condition.

Figure 4.13 shows the evolution of the normalized Nusselt number as a function of the Reynolds number, following the same approach adopted in the previous paragraph for the friction factor and the mean vorticity.

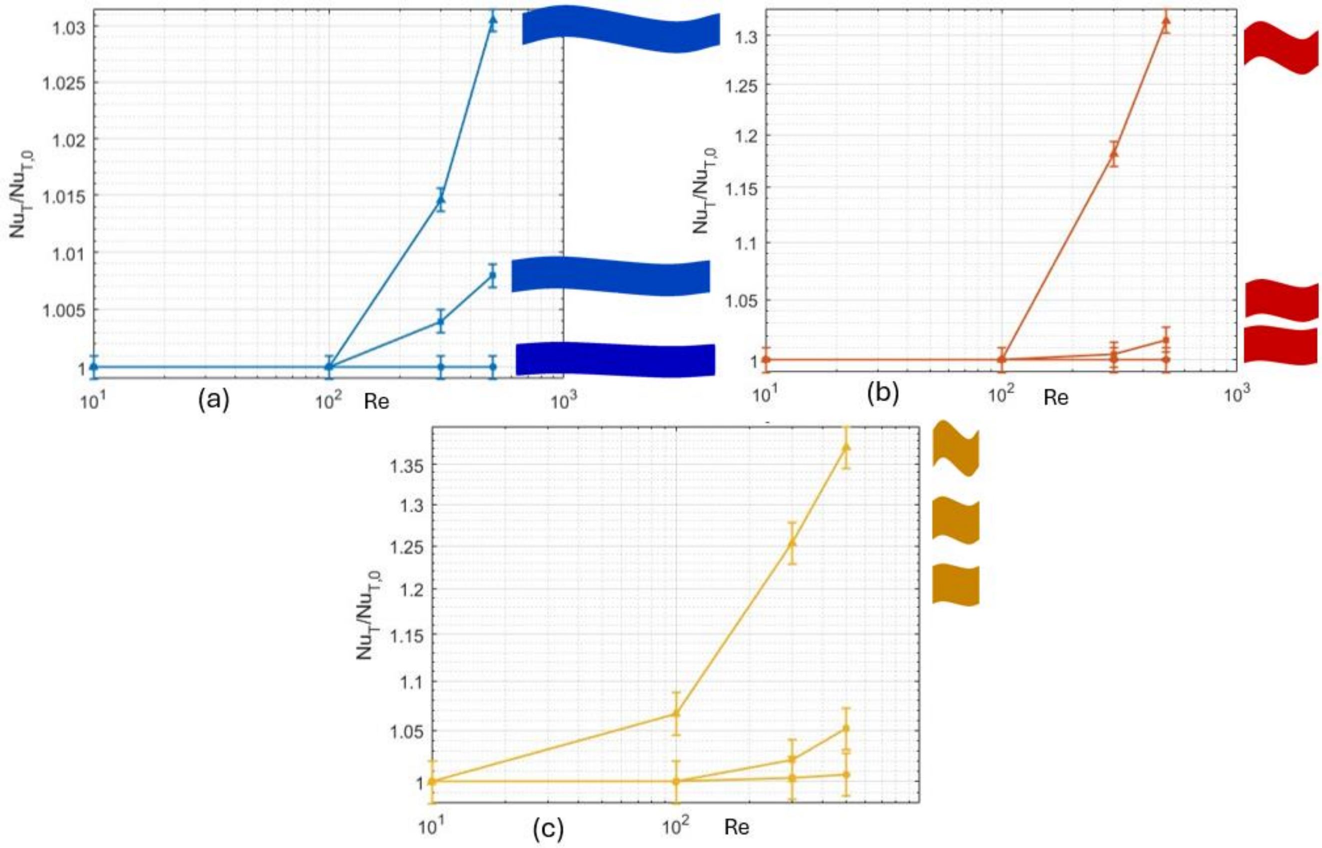

Figure 4.13: Nusselt number increase as a function of the Reynolds number for $\alpha = 0.5\ (a), 1.5\ (b), 2.5\ (c)$

For the lowest corrugation (α = 0.5, panel a), the heat transfer remains almost unchanged as Re increases, showing a very limited enhancement even at higher flow intensities. This indicates that for mildly perturbed geometries, the flow structure remains predominantly laminar, and convective effects do not significantly intensify.

In contrast, for larger corrugation amplitudes (α = 1.5 and α = 2.5, panels b and c), the Nusselt number exhibits a more pronounced growth with Reynolds number. This trend reflects the increasing contribution of vortical motion and fluid mixing induced by the wavy geometry, which becomes progressively stronger as α increases.

It is also worth noting that the only configuration showing a clear increase in the Nusselt number already at Re = 100 is the most corrugated one (α = 2.5, S = 0.5). This behavior can be explained by examining the corresponding streamline plots (Fig. 4.14), where the onset of recirculation zones and vortical structures is already visible at this relatively low Reynolds number. These early-formed vortices enhance the local fluid mixing and promote heat transfer, leading to an earlier deviation from the purely laminar trend observed in smoother geometries:

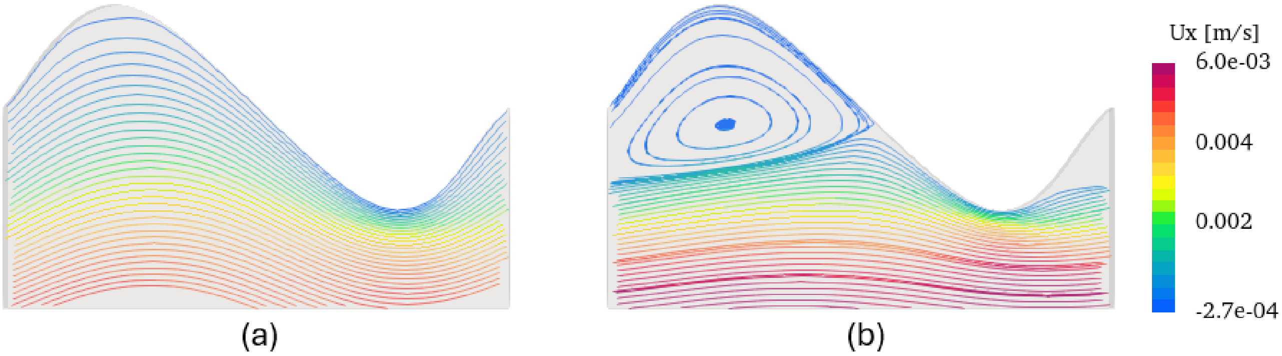

Figure 4.14: onset of recirculation zones when increasing Reynolds from (a) Re=10, to (b) Re=100

Following the same approach of chapter 4.2, a quantitative correlation was also established between the normalized Nusselt number and the normalized mean vorticity through a global fitting procedure. For each geometric configuration and Reynolds number, the values of $(Nu_T/Nu_{T,0})$ and $(\bar{\omega}_z/\bar{\omega}_{z,0})$ were extracted and combined into a single dataset, allowing the identification of a general trend across all tested cases. Error bars were included to account for the uncertainty associated with the thermal evaluation.

The resulting data points were fitted in log–log space using a power-law model with an additional offset term, expressed in the general form:

$$\left(\frac{Nu_T}{Nu_{T,0}} - 0.5\right) = A \cdot \left(\frac{\overline{|\omega_z|}}{|\omega_{z,0}|} - 0.5\right)^B + C \qquad (4.17)$$

where A, B, and C are fitting coefficients obtained through nonlinear regression. The correlation provides a very good agreement ($R^2 \approx 0.985$), indicating that the normalized Nusselt number follows a power-law dependence on the normalized mean vorticity. This result quantitatively confirms that the enhancement in heat transfer is directly related to the intensification of vortical motion within the channel.

The fitted relation can be expressed as:

$$\frac{Nu_T}{Nu_{T,0}} = 0.49 \cdot \left(\frac{\overline{\omega_z}}{\omega_{z,0}} - 0.5\right)^{3.6} + 0.95 \qquad (4.18)$$

As shown in Figure 4.15, the fitted curve accurately reproduces the overall trend between the normalized quantities.

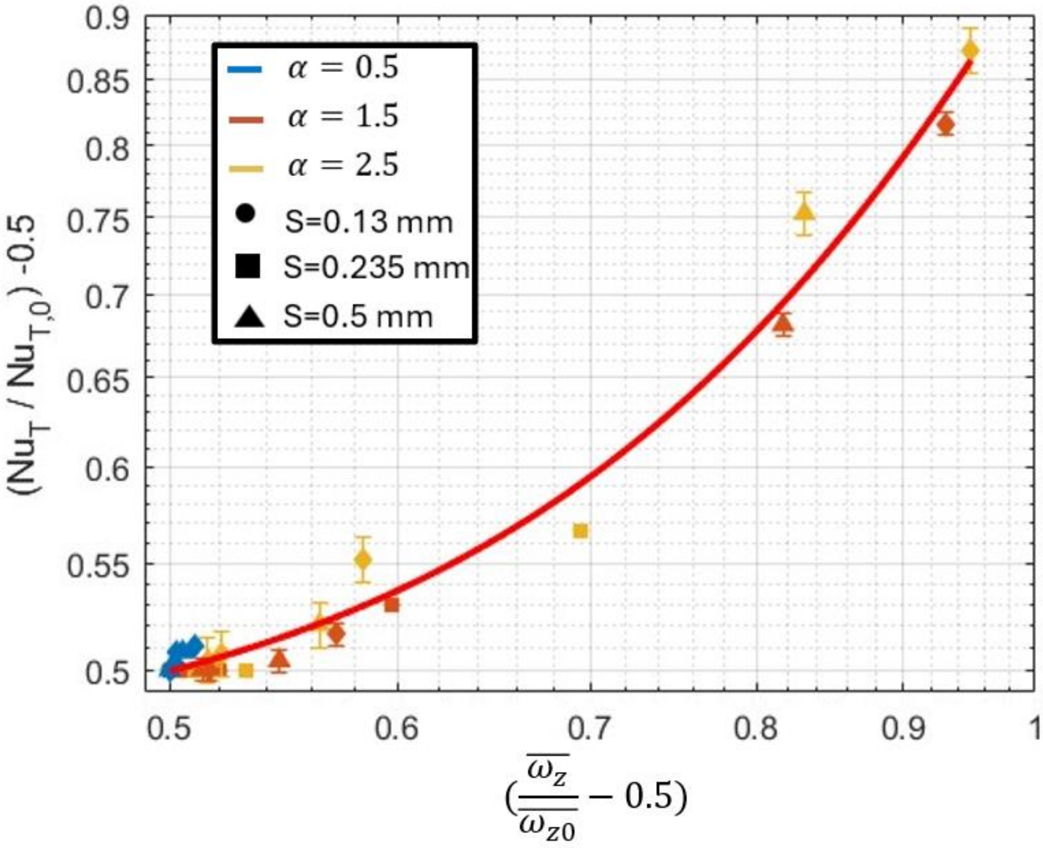

Figure 4.15: curve fitting for normalized Nu_T as function of normalized vorticity

The monotonic power-law reflects the progressive increase in convective heat transfer with the growth of the mean vorticity, with a power of 3.6, which is associated with stronger secondary flows and enhanced fluid mixing. The small offset term C accounts for residual effects not directly captured by the mean vorticity, such as local flow asymmetries or near-wall thermal gradients. The close agreement between the numerical data and the fitted curve across all Reynolds numbers and geometrical configurations further supports the interpretation that the mean vorticity acts as a reliable global indicator of the heat transfer enhancement mechanisms induced by the wall corrugation.

The same approach was adopted for the imposed heat flux boundary condition: the following equation was then obtained with $R^2 \approx 0.98$:

$$\frac{Nu_{q''}}{Nu_{q'',0}} = 0.74 \cdot (\frac{\overline{\omega_z}}{\omega_{z,0}} - 0.5)^{4.37} + 0.96 \tag{4.19}$$

Figure 4.16 shows the curve fitting the data.

The curve obtained for the constant heat flux case (Nu_q'') exhibits a slightly steeper slope, with a power of 4.16 suggesting a somewhat stronger sensitivity of the heat transfer enhancement to the increase in vorticity. Nevertheless, the general behavior of the two datasets remains consistent.

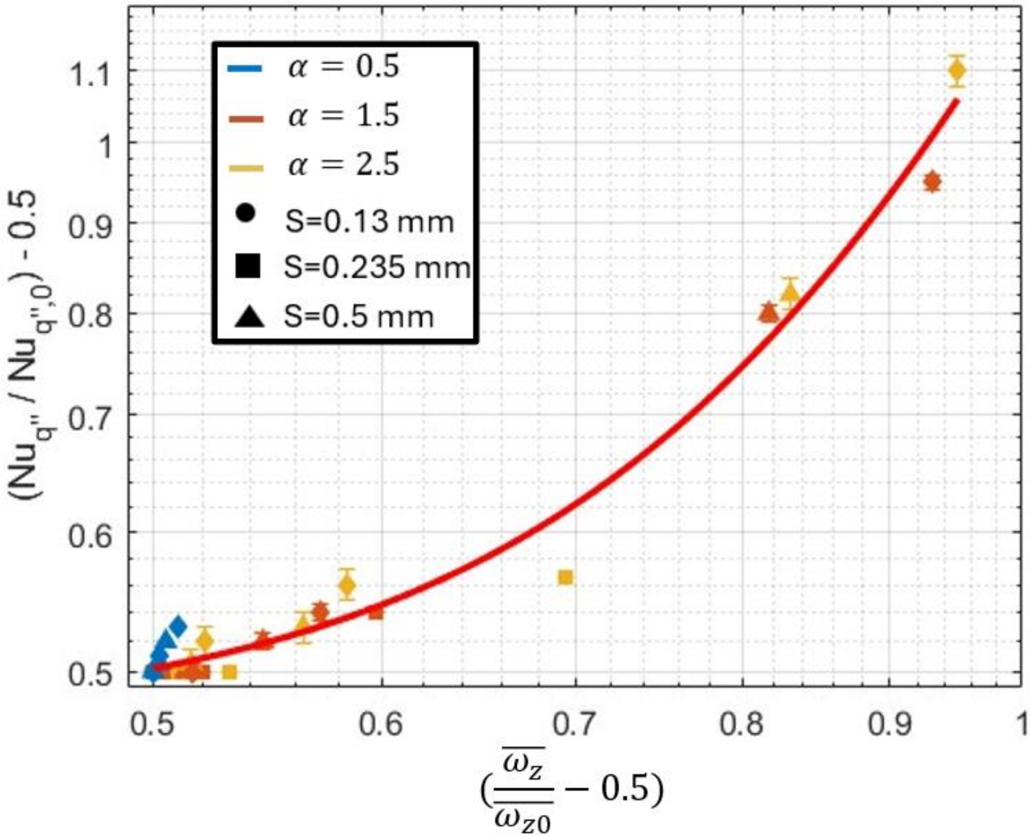

Figure 4.16: curve fitting for normalized $Nu_{q''}$ as function of normalized vorticity

Once a certain threshold of vorticity is exceeded, corresponding to Reynolds numbers of approximately 10 and 100, and extending up to 300 and 500 for less corrugated geometries, the Nusselt number begins to rise rapidly, following an almost exponential trend with respect to vorticity. This behavior clearly indicates that the intensification of vortical structures in the flow strongly promotes convective heat transfer, independently of the imposed thermal boundary condition. Although slightly higher values of the normalized Nusselt number are achieved under constant heat flux, both correlations confirm that the increase in heat transfer is directly linked to the strengthening of the flow recirculation and mixing phenomena induced by wall corrugation.

Finally, the reliability of these correlations is supported by the high values of the determination coefficient R^2, equal to 0.985 for the constant wall temperature case and 0.98 for the constant heat flux case. These results demonstrate that the fitted curves provide an excellent representation of the numerical data, confirming the robustness and coherence of the proposed relationship between vorticity intensity and heat transfer enhancement in laminar regimes. These two correlations may be used for a preliminary design of heat pipes or heat transfer enhancement method, because they lead to the possibility of tuning the vorticity in such a way that we can increase the heat exchange, therefore the Nusselt number, keeping under control the pressure drop, represented by the friction factor.

4.3.2 Turbulent regime

Figure 4.17 shows the raw results for the Nusselt number, while Figure 4.18 in normalized form:

The observed trends closely follow those previously identified for the mean vorticity. In particular, the two configurations with the largest corrugation amplitude exhibit the highest Nusselt numbers, as the stronger recirculation zones and more intense fluid mixing promote higher convective heat transfer. Immediately after these, the configurations with the shorter wavelength ($\alpha = 2.5$) also display a significant enhancement, confirming that a reduced period effectively strengthens the mixing even with a lower amplitude. Finally, the two configurations with α = 1.5 show the lowest Nusselt values, consistent with their weaker vortical structures and more limited flow interaction.

Finally, using the same approach as in previous paragraphs, a fitting curve procedure is applied. The used equation is the following:

$$(\frac{Nu_T}{Nu_{T,0}} - 1) = A \cdot (\frac{\overline{\omega_z}}{\omega_{z,0}} - 1)^B + C \tag{4.20}$$

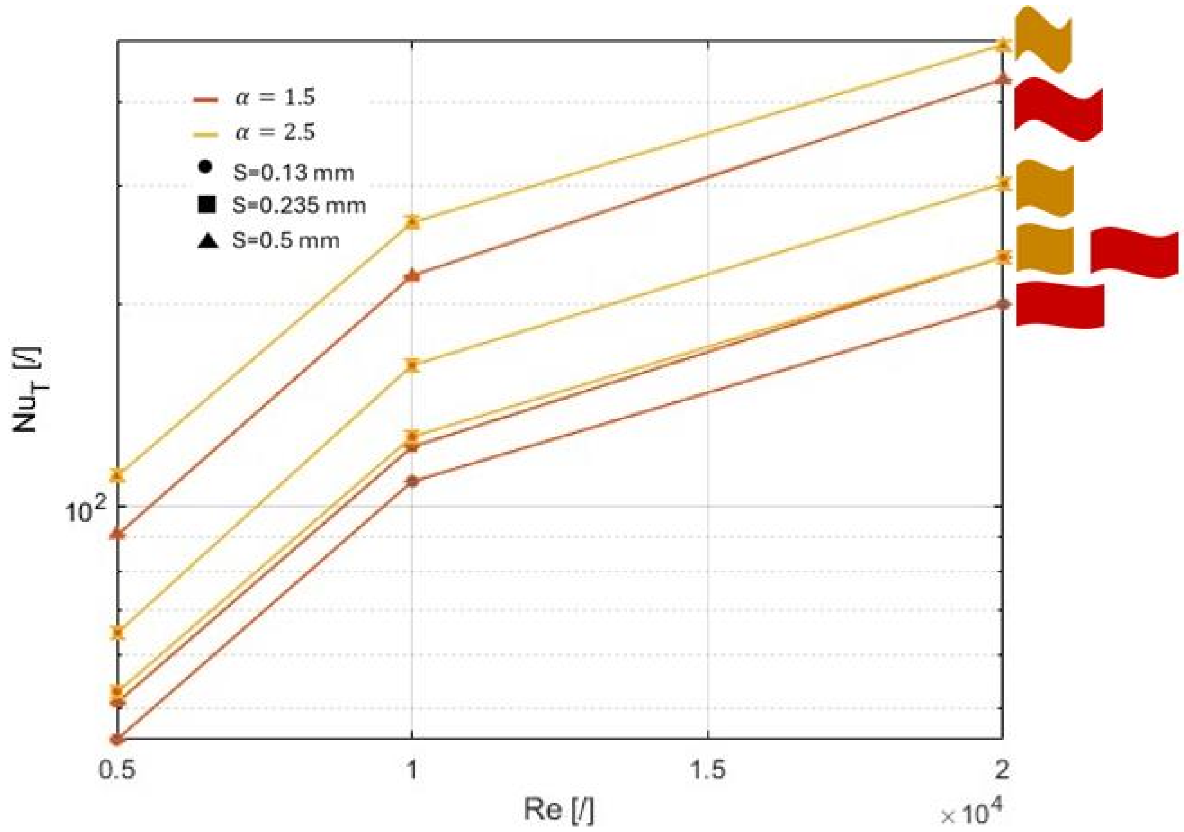

Figure 4.17: Nusselt number evolution in turbulence with increasing Reynolds

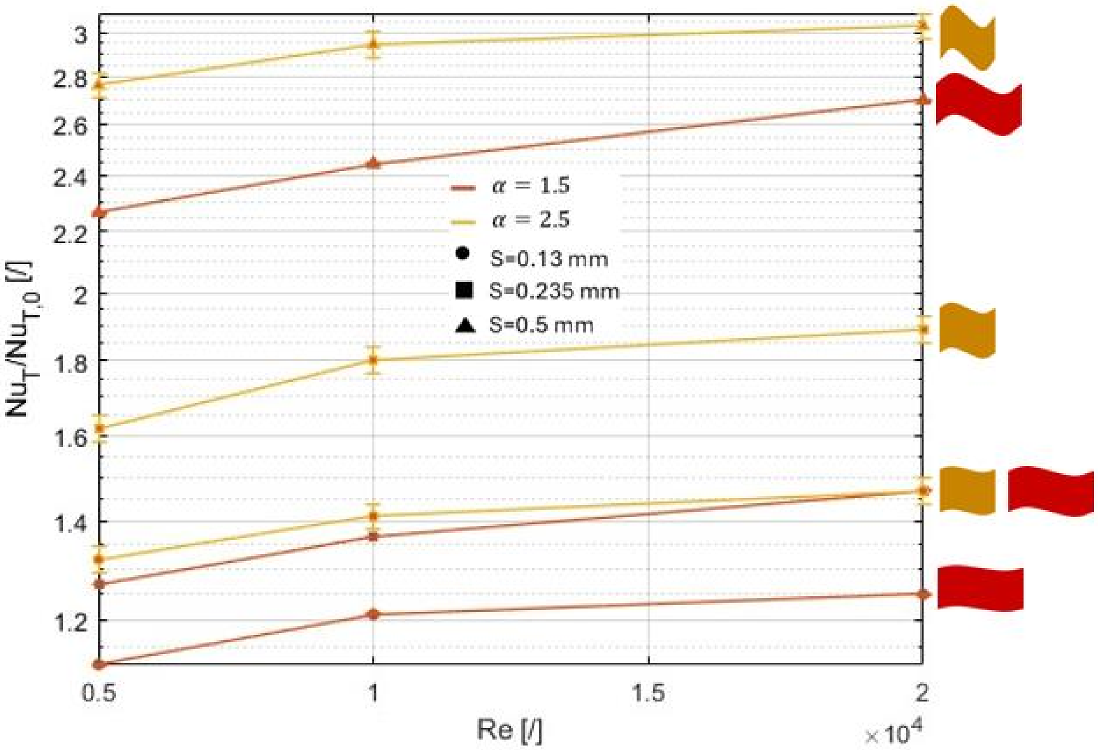

Figure 4.18: Normalized Nusselt number evolution in turbulence with increasing Reynolds

The curve (Figure 4.19) fitting equation is then found with a fitting parameter of $R^2 \approx 0.988$:

$$\frac{Nu_T}{Nu_{T,0}} = 1.51 \cdot (\frac{\overline{\omega_z}}{\omega_{z,0}} - 1)^{0.74} + 0.58 \tag{4.21}$$

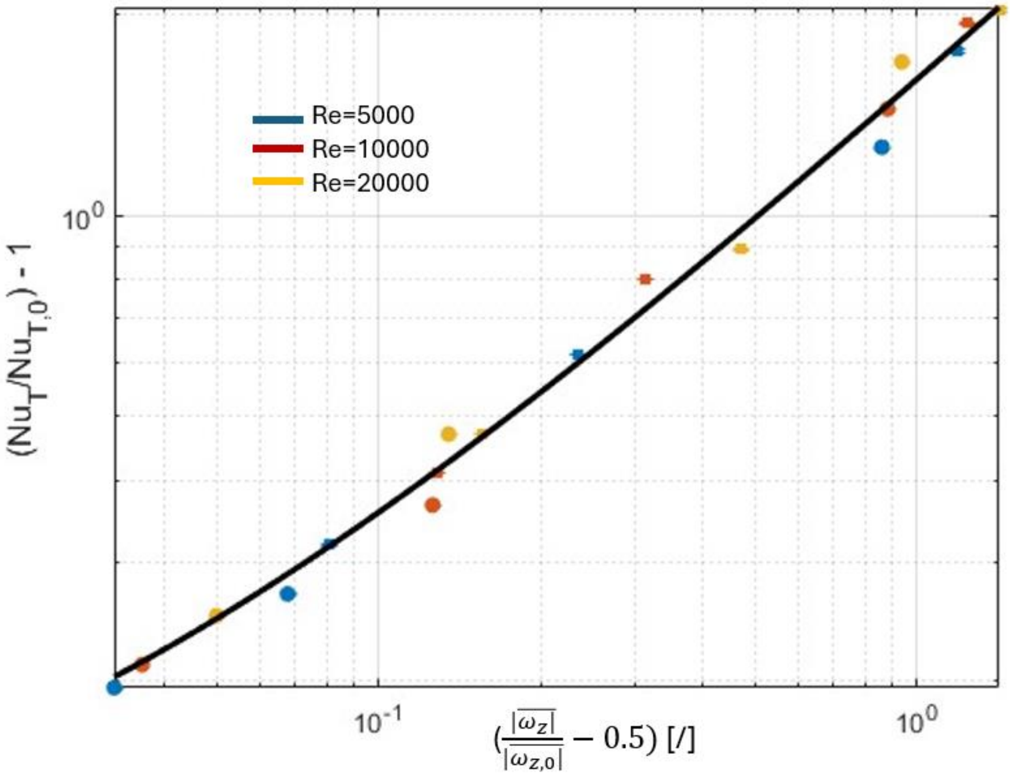

Figure 4.19: curve fitting for normalized Nu_T as function of normalized vorticity

Overall, the obtained results highlight the key role of vorticity in governing heat transfer enhancement under turbulent conditions. The strong correlation between the normalized Nusselt number and the normalized mean vorticity indicates that the development of coherent vortical structures directly translates into improved convective efficiency. This confirms the physical consistency of the proposed relationship and reinforces the validity of using vorticity-based indicators to predict the thermal behavior of corrugated channels.

5 Conclusions

The present work explored the correlation between flow vorticity and the thermo-hydraulic performance of sinusoidal corrugated channels through detailed numerical simulations. The two-dimensional computations, performed using OpenFOAM, enabled a quantitative assessment of how geometric parameters and Reynolds number influence the development of vortical structures, and how these structures, in turn, govern both the heat transfer coefficient and the friction factor.

The results demonstrated that increasing the corrugation amplitude promotes the formation of recirculation zones and significantly enhances the overall vorticity within the channel. This intensification of vortical motion strengthens the mixing between the core flow and near-wall regions, leading to a marked increase in the Nusselt number. At the same time, the stronger vorticity also generates higher velocity gradients and wall shear stresses, resulting in a corresponding rise in the friction factor. Configurations with shorter wavelengths ($\alpha = 2.5$) exhibited intermediate behavior, confirming that both the amplitude and the spatial frequency of the corrugation play a decisive role in determining the flow organization and the associated thermal and hydraulic performance.

A key outcome of this study was the establishment of quantitative correlations linking the mean vorticity to both the Nusselt number and the friction factor. The numerical data were successfully fitted using power-law relationships, yielding high coefficients of determination ($R^2 \approx 0.98$–0.99). These correlations reveal that both heat transfer and pressure losses scale nonlinearly with the mean vorticity. Beyond a critical vorticity threshold, corresponding to the onset of strong recirculation and enhanced mixing, the Nusselt number rises sharply, indicating that the vorticity field acts as the primary driver of convective heat transfer enhancement in corrugated geometries.

The relationships obtained in this work provide a physically consistent and predictive link between the flow topology and the global performance of the channel. They represent a first step toward a generalized framework capable of connecting local flow dynamics to macroscopic heat transfer behavior. In the future, these vorticity-based correlations could serve as practical design guidelines or *rules of thumb* for the preliminary optimization of complex geometries, allowing engineers to estimate the trade-off between heat transfer enhancement and frictional penalty from simple flow metrics.

5.1 Further works

Although the present study provided valuable insights into the relationship between vorticity and the thermo-hydraulic performance of sinusoidal channels, several directions remain open for future investigation. A natural continuation of this research would involve extending the analysis to three-dimensional corrugated geometries. In contrast to the two-dimensional configuration adopted in this work, three-dimensional channels would allow the capture of spanwise flow variations, secondary vortical motions, and complex turbulent structures that can significantly affect both heat transfer and pressure losses. Investigating these effects would lead to a more realistic and comprehensive understanding of the flow physics that govern practical heat exchanger systems.

Another important step would be to expand the database by including a wider set of geometric configurations and Reynolds numbers. A broader range of cases would enable a more accurate fitting of the empirical trends identified in this study, improving the robustness and generality of the proposed correlations. A larger dataset could better describe the transition region where the scaling behavior of the Nusselt number and the friction factor with vorticity changes, providing more precise predictive models.

Overall, extending this methodology toward three-dimensional domains and to a wider range of geometrical configurations would represent a valuable step forward in developing a general and predictive framework for the design and optimization of advanced corrugated channels and heat transfer surfaces.

References

[1] H. J. Lee, S. J. Lee, "Effect of Secondary Vortex Flow Near Contact Point on Thermal Performance in the Plate Heat Exchanger with Differenet Corrugation Profiles", energies, 2020.

[2] X. Gao, W. Li, J. Wang, "Heat transfer and flow characteristics in a channel with one corrugated wall", Science China Tecnhological Sciences, 2014.

[3] N.Kaewchoothong, K. Maliwan, K. Takeishi, C. Nuntadusit , "Effect of inclined ribs on heat transfer coefficient in stationary square", Theoretical & Applied Mechanics Letters, 2017.

[4] L. Savoldi, A. Cammi, L. Marocco, E. Gajetti, "Investigating the Reynols analogy for Triply Periodic Minimal Surfaces in low-Reynolds regime", ICHMT digital library, 2025.

[5] G. Karlsson, L. Wang, C. Fureby, "Laminar to turbulent transition using large eddy simulation in cross-corrugated heat exchanger channels", SSRN, 2023.

[6] P. Naphon, "Heat tranfer characteristics and pressure drop in channel with V corrugated upper and lower plates", Energy conversion and management, 2007.

[7]S. Nashee, "Numerical study for fluid flow and heat transfer characteristics in a corrugating channel", International Journal of heat transfer and Technology, 2023.

[8] https://www.diabatix.com/blog/innovating-thermal-deign-with-tpms-structures [Online] November 18, 2024.

[9] K. Amara, M. Saghir, R. Abdelijabar, "Review od Triply Periodic Minimal Surface (TPMS) Structures for Cooling Heat Sinks", energies, 2025.

[10] H. J. Lee, S. H. Lee, "Effect of secondary vortex flow near contact point on heat transfer in plate heat exchanger with various corrugated geomteries", energies, 2020.

[11] S.W. Gepner, J. M. Floryan. "Flow dynamics in sinusoidal channels at moderate Reynolds numbers", J. Fluid Mech, 2023.

[12] A. Sidi, "Pratical Extrapolation Methods, I - The Richardson Extrapolation Process and Its Generalizations", 2010.

[13] www.simscale.com. [Online]

[14] en.wikipedia.org/wiki/Law_of_the_wall [Online]

[15] Frank P. Incropera et al., "Fundamentals of Heat and Mass Transfer".

[16] Owlcation.com/stem/how-to-read-a-moody-chart [Online]

[17] OpenFOAM v.2412. [Online] December 2024.